6-6-2014

# First Time Measurements of Polarization Observables for the Charged Cascade Hyperon in Photoproduction

Jason S. Bono
jason.s.bono@gmail.com

FLORIDA INTERNATIONAL UNIVERSITY

Miami, Florida

# FIRST TIME MEASUREMENTS OF POLARIZATION OBSERVABLES FOR THE CHARGED CASCADE HYPERON IN PHOTOPRODUCTION

A dissertation submitted in partial fulfillment of the

requirements for the degree of

DOCTOR OF PHILOSOPHY

in

PHYSICS

by

Jason Bono

2014

To: Interim Dean Michael R. Heithaus
College of Arts and Sciences

This dissertation, written by Jason Bono, and entitled First Time Measurements of Polarization Observables for the Charged Cascade Hyperon in Photoproduction, having been approved in respect to style and intellectual content, is referred to you for judgment.

We have read this dissertation and recommend that it be approved.

Brian A. Raue

Misak M. Sargsian

Cem Karayalcin

Lei Guo, Major Professor

Date of Defense: June 6, 2014

The dissertation of Jason Bono is approved.

Interim Dean Michael R. Heithaus
College of Arts and Sciences

Dean Lakshmi N. Reddi
University Graduate School

Florida International University, 2014

## DEDICATION

This dissertation is dedicated to my entire family, but most significantly to my mother Sharon. Without her faith and devotion, my early educational struggles might never have been overcome.

ACKNOWLEDGMENTS

My time spent in fundamental research has been pleasurable and deeply gratifying, although the trajectory of events preceding this completed work has been somewhat circuitous. I suppose it's all part of the fun, though. Unpredictability in research, numerous successes, failures, dead ends, new ideas, and excitement have been recurrent themes against a background of some of the less energizing aspects of life in graduate school. Amidst the mixture of light and dark, in the journey which this work represents, I am grateful for every inch in its broad path. Melodrama aside, this accomplishment is contingent upon the hard work and devotion of many people to whom I wish to express my sincere gratitude.

First, my deepest gratitude goes to Lei Guo for his excellent guidance over the past three years. With a contagious passion for physics, keen intuition and an openness to new ideas, he has been a great source of inspiration. His attentiveness and clarity across scales from the big picture to the most subtle aspects of analysis have provided a rich and open dialog which has been instrumental in my development. Although, Lei's uncanny memory for the details of such discussions has worked to my detriment on an occasion or two. I additionally thank Lei for the answers he did not provide and for his encouragement to think for myself. His genuine interest in the wellbeing of his students has provided me solace during important moments. In the midst of more difficult times, knowing that someone possessed a selfless imperative to help, was often help enough.

I am extremely gracious for the additional and voluntary guidance which Brian Raue bestowed. Many key aspects of the analysis directly descended from his expert advise as a physicist and statistician. His consistent participation through week after week, of long, and sometimes overly expressive research meetings was paramount to our results. I have learned so much and consider Brian as my adoptive advisor. Together

Brian and Lei have been, in a strict sense, brilliant, but I am especially grateful for the tremendous amount trust that the two invested in me. Perhaps most importantly, our research has been a lot of fun. I implore both of them to continue training graduate students together.

I would like to thank the world class scientists at Jefferson Lab who maintained smooth operation of the CLAS detector during data collection. Extra thanks goes to the hardworking members of the g12 collaboration; especially to those who slaved in data reconstruction and calibrations as graduate students and post-docs, Johann Goetz, Diane Schott, Mukesh Saini, Craig Bookwalter, Mike Kunkel and Mike Palone.

I thank Kanzo Nakayama, Misak Sargsian and Oren Maxwell as theoreticians with whom consulting brought fruitful insight. Special thanks goes to Kanzo for this continued correspondence and collaboration. I kindly thank Joerg Reinhold for patiently teaching me principals of nuclear physics experimentation. I also thank my undergraduate professor James Cresser for encouraging me to further pursue physics. I still mull over our discussions on quantum decoherence.

Colleagues, horses, from the FIU nuclear physics lab, thank you. Eric Pooser, Hari Khanal, Dipak Rimal, Rafael Badui, William Phelps, Adam Freese and Marianna Gabrielyan, you guys were all amazing to work with. Besides being the most creative and smartest group of people I know, you are also among the most light-hearted and hilarious, that's what u r doing. I hope you have benefited from my presence as much as I have from yours. Special thanks goes to former post-doc Puneet Khetarpal for sharing his expertise in programing.

Thanks to my siblings Andrew Bono and Kathleen Schecher with whom I delight in sharing fun challenges and amusing times. From our distinct breed of humor containing themes and debates such as the spelling of a certain dog's name, to our constant search for adventure via land, snow, sea and the otherwise more absurd, the

elements of our friendship are unique and I value them dearly. You both, presumably without realizing, have kept me on track time and time again.

To my father Jay Bono, thank you for our friendship and for cultivating my curiosity about the world. I consider myself fortunate having grown up with access to great ideas and for them having been communicated so engagingly and often. I carry several details of our early conversations, although the most memorable aspects pertain to the open-endedness of inquiry and its implied imaginative freedom. I am delighted that our conversations, which have always been refreshingly fluid, have paradoxically grown in both sophistication and immaturity.

To my mother and stepfather Sharon and Chuck Carlino, thank you for everything you have given us, including putting up with the aforementioned adventures. I owe more to my mother than I may express in this scope. She has held us all together with her perseverance and seeming omniscient judgment. For her efforts and struggles that I know, and for those which I remain ignorant, I wish her happiness and awareness of how great a mother she has been. To Chuck, thanks for taking in our family as your own, you have been a blessing.

Thanks to my friends who moved half a world away to be in Miami. For those who expressed that their relocation was friendship driven, I feel special gratitude and humility.

Finally to Jen McAnney, thank you for being my friend in the relatively frantic time of writing and for patiently proofreading my work. I'm energized by your spirit and humbled by your kindness. I hope your attributes are contagious because I would like to be more like you.

ABSTRACT OF THE DISSERTATION

FIRST TIME MEASUREMENTS OF POLARIZATION OBSERVABLES FOR THE CHARGED CASCADE HYPERON IN PHOTOPRODUCTION

by

Jason Bono

Florida International University, 2014

Miami, Florida

Professor Lei Guo, Major Professor

The parity violating weak decay of hyperons offers a valuable means of measuring their polarization, providing insight into the production of strange quarks and the matter they compose. Jefferson Lab's CLAS collaboration has utilized this property of hyperons, publishing the most precise polarization measurements for the $\Lambda$ and $\Sigma$ in both photoproduction and electroproduction to date. In contrast, cascades, which contain two strange quarks, can only be produced through indirect processes and as a result, exhibit low cross sections thus remaining experimentally elusive.

At present, there are two aspects in cascade physics where progress has been minimal: characterizing their production mechanism, which lacks theoretical and experimental developments, and observation of the numerous excited cascade resonances that are required to exist by flavor $SU(3)_F$ symmetry. However, CLAS data were collected in 2008 with a luminosity of 68 pb$^{-1}$ using a circularly polarized photon beam with energies up to 5.45 GeV, incident on a liquid hydrogen target. This dataset is, at present, the world's largest for meson photoproduction in its energy range and provides a unique opportunity to study cascade physics with polarization measurements.

The current analysis explores hyperon production through the $\gamma p \to K^+K^+\Xi^-$ reaction by providing the first ever determination of spin observables $P$, $C_x$ and $C_z$ for the cascade. Three of our primary goals are to test the only cascade photoproduc-

tion model in existence, examine the underlying processes that give rise to hyperon polarization, and to stimulate future theoretical developments while providing constraints for their parameters. Our research is part of a broader program to understand the production of strange quarks and hadrons with strangeness. The remainder of this document discusses the motivation behind such research, the method of data collection, details of their analysis, and the significance of our results.

TABLE OF CONTENTS

LIST OF TABLES

LIST OF FIGURES

# Chapter 1

## Introduction and Motivation

Experimental nuclear and particle physics provide a glimpse of what is countenanced by nature. The mantra "All that is permissible is required" hints at the utility of carefully crafted observation. Specific measurements under controlled conditions as dictated by theory have provided rich information into the workings of our universe, revealing remarkable order and beauty, as well as peculiarity. Through modern physics, a strange inner world to which we are blind in daily experience, has begun to become illuminated. Although, there is still much work to be done.

The present chapter provides an overview of the prevailing theoretical framework and a few of its shortcomings, including those that encompass our research. The motivation behind our research is discussed in detail.

## 1.1 Overview of the Standard Model of Particle Physics

The tradition of atomism dates back to ancient India and Greece, however for brevity, we will fast forward through our long history of natural philosophy to the dawn of modern particle physics: the age of quantum theory. In the early 1940s, only a handful of what were thought of as elementary particles had been identified. Among them were the electron, positron, muon, photon, neutron and proton [1]. While the former three particles are still believed to be void of internal structure, the latter two have been found to be composites of smaller elements. Our current picture of particle physics is the result of a renaissance-like explosion of experimental, and theoretical work in the later half of the twentieth century. Such developments came predominately from cosmic-ray and collider experiments, revealing new particles that did not fit the traditional atomic scheme of matter in which neutrons and protons

were fundamental. Several new classes of subatomic particles including a vast array of mesons and baryons were identified. Attempts to explain the complexity of the observed phenomena and growing list of "elementary" particles blossomed into what is now known as the *standard model*: an extraordinarily broad and successful theory. In the current picture, all matter is composed of a few particles categorized as quarks and leptons, interacting through the exchange of field quanta known as gauge bosons. All of the aforementioned elementary particles are shown in Table 1.1 along with the recently observed Higgs boson, the quanta of the Higgs field, responsible for the breaking of certain symmetries (*i.e.*, electroweak), which endows the leptons and quarks, along with the $Z$ and $W$, bosons with mass.

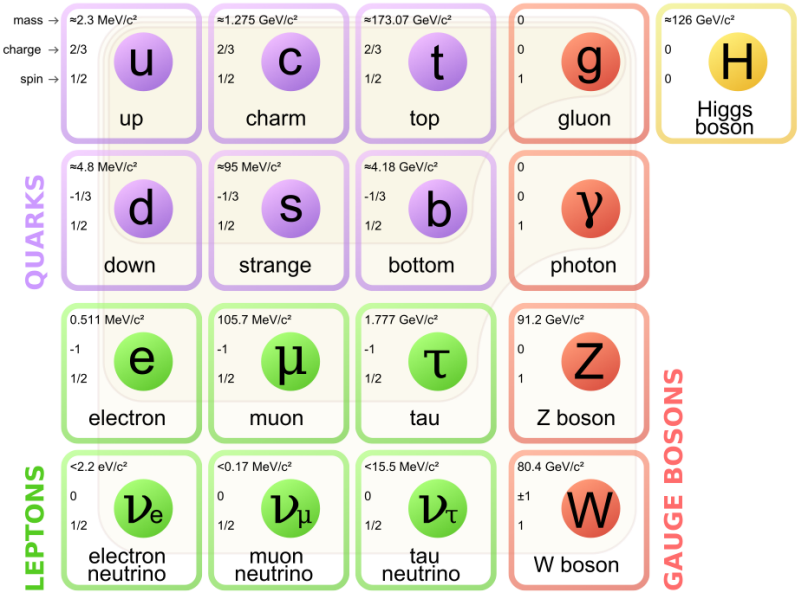


Table 1.1: A table of the elementary particles. The mass, charge, spin and symbol for each elementary particle is shown. For the quarks and leptons, first, second and third generations are organized in the first, second and third columns respectively. Image Source [2]

The exchange of gauge bosons is thought to underpin all dynamical interactions in the universe [3]. Each fundamental interaction, mediated by different gauge bosons, is classified into the strong, weak, electromagnetic or gravitational interactions. The

gauge boson underlying the latter interaction, referred to as the *graviton*, is yet to be observed experimentally; gravity is not included in the standard model but because of its weakness, is negligible in the subatomic regime. The color, or strong interaction is mediated by the exchange of *gluons*. *Photons* are exchanged in electromagnetic interactions, while the weak interaction is mediated by the exchange of $W$ and $Z$ bosons. As it turns out, the weak and electromagnetic interactions are actually differing aspects of the same phenomenon with the unsurprising name of the *electroweak* interaction. The phenomenological difference between the electromagnetic and weak forces at energies below 100 GeV is a result of the non-zero mass of the $W^{\pm}$ and $Z^0$ bosons, which owe their finite mass to the Higgs mechanism [3].

Leptons, given their name because of their small masses [4], interact electromagnetically and weakly but not via the strong force. Intricate collective behavior of interacting leptons diversifies the characteristics of atomic matter and gives rise to all phenomena in chemistry and biology, from the distinguishing features of the elements, to the microscopic processes upon which all life is dependent. Additionally, leptons are observed to participate in nuclear $\beta$-decay among other weak interactions, a process that has a large effect on the composition of the universe but is only observable through developments in nuclear experimentation.

Quarks, the building blocks of hadronic matter (hadrons refer to all baryons and mesons), interacting primarily through the strong interaction, exhibit a strange behavior physicists called *confinement*. Confinement describes the phenomenon that quarks are never found alone. Although there is no known analytic proof that quantum chromodynamics (QCD), the theory of the strong interaction, should exhibit confinement, it is generally understood through least-action principals and consideration of the vacuum's quantum nature. The energy of interaction between quarks

does not diminish with distance ($r$) as shown in the form of the potential,

$$V_c = -\frac{4}{3}\frac{\alpha_s}{r} + \kappa r. \tag{1.1}$$

As bound quarks become spatially separated, a point is reached when it is more energetically favorable for a quark-antiquark pair to spontaneously appear from the vacuum, than for $V_c$ to keep increasing according to Equation 1.1. The creation of pairs reduces the potential energy associated with the binding of the two original quarks, more than the energy required to produce the masses of the new quarks. Effectively, an attempt to separate a hadron (a bound state of two or more quarks) into its constituent quarks by "pulling" it apart results in the production of a "jet" of hadrons in a process called *hadronization*.

Besides confinement, quark dynamics have many other peculiarities. To explain how otherwise identical particles could coexist, bound in the ground state (*i.e*, the $\Delta^{++}$, a baryon consisting of three $u$ quarks) without violating the Pauli exclusion principle, quarks were postulated to be endowed with an extra degree of freedom called "color"[5]. The possible colors an individual quark can posses are red, green or blue, named after the additive primary colors to draw an analogy to color theory in the visual arts. The anti-quarks can take on complementary color denoted as cyan (antired), magenta (antigreen) and yellow (antiblue) analogous with the subtractive primary colors. As a consequence of confinement, all free particles have a neutral color charge.

The concept that all hadronic matter is composed of quarks was introduced in part to explain the flavor symmetry present in the enumeration of hadron states. In the quark model, baryons contain three quarks and mesons contain a quark-antiquark pair. To be color neutral, baryons have one quark of each color, red, green and blue.

In a meson, it's quark may take on any color with it's antiquark taking on the corresponding anti-color. The analogy of color charge with actual color only holds to the extent to which colors add, forming color neutral states (black or white). The lightest mesons, one example among many being the pion ($\pi$), contain various quantum mechanical combinations of first generation ($u$ and $d$) quarks. Other categories of mesonic matter contain higher generations quarks such as the kaons ($K$), which possess a strange quark, and the heavy mesons comprising charm and bottom quarks. The lightest baryons contain only first generation quarks. Protons and neutrons, being the lightest and most common baryons, posses quark configurations of $uud$ and $ddu$ respectively. The least massive baryon with a single strange quark is known as the lambda ($\Lambda$), $uds$, whereas the lightest baryonic states of multiple strangeness are the neutral and charged cascades ($\Xi$) with quark configurations of $uss$ and $dss$, respectively.

The masses of the hadrons are only partially a result of the masses of the quarks they comprise. For example, the proton mass is around 938 MeV while adding up the masses of it's constituent quarks gives a mass around 10 MeV, not much more that 1% of the total. Most hadronic mass actually comes from gluonic binding energy and the undulating sea of *virtual* quark-antiquark pairs that appear and disappear on time scales according to the Heisenberg Uncertainty Principal, $\Delta E \Delta t \geq \frac{\hbar}{2}$. Virtual quarks within the hadron are also commonly referred to as *current* or *sea* quarks. Indeed, the simple quark picture is too large a simplification to characterize many aspects of hadronic physics. The *proton spin puzzle* refers physicists' discovery that the nucleon's spin-half is not solely the result of parallel-parallel-antiparallel configuration of it's constituent spin-half quarks. Uncovering the origin of proton spin is connected with our research on the doubly-strange charged cascade ($\Xi^-$) in the present document and an elaboration on the connection is provided in Section 1.3.

The study of baryons containing multiple strange quarks, which is the subject of our analysis, has played an important role in the development of the quark model. Gell-Mann's *Eightfold Way* [6], intentionally alluding to Buddhism's Noble Eightfold Path, organizes the mesons and baryons into ordered multiplets. Fig. 1.1 shows the Baryon Octet, additionally displaying the now know quark makeup of each particle. The organizational principles of the Eightfold Way applied to spin-3/2 baryons (shown in Fig. 1.2) required the existence of the Omega minus ($\Omega^-$), which had not yet been observed. It was predicted that the missing particle would have a strangeness of -3 and electric charge of -1, which was later verified experimentally, winning Gell-Mann the Nobel Prize in physics. We now know the quark composition the omega to be *sss*.

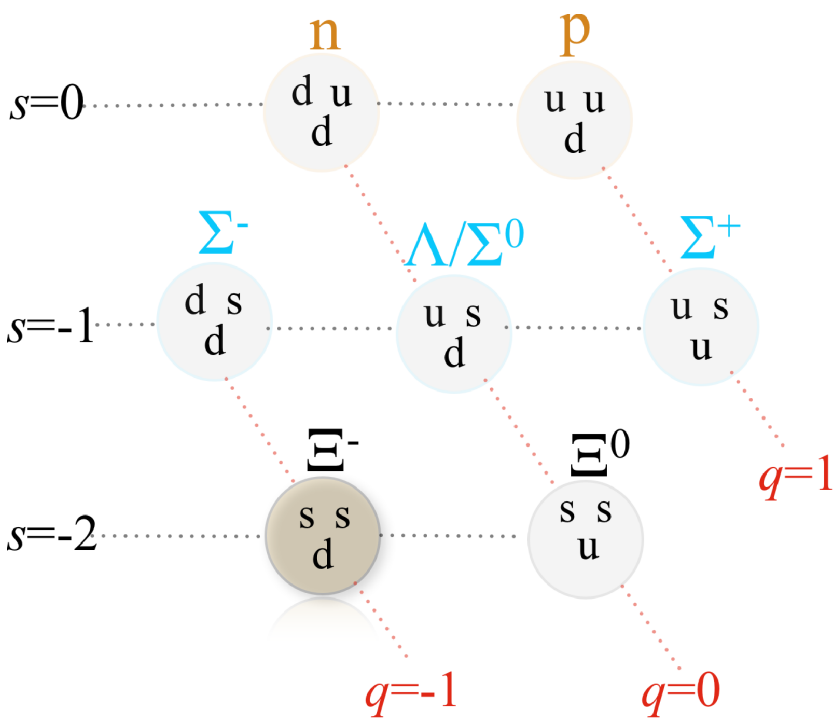


Figure 1.1: The Baryon Octet as organized in the Eightfold Way according to charge and strangeness. The octet contains spin-1/2 nucleons, sigmas, the lambda, and cascades. The quark composition is additionally shown. The particle being studied in our analysis, the charged cascade, is highlighted.

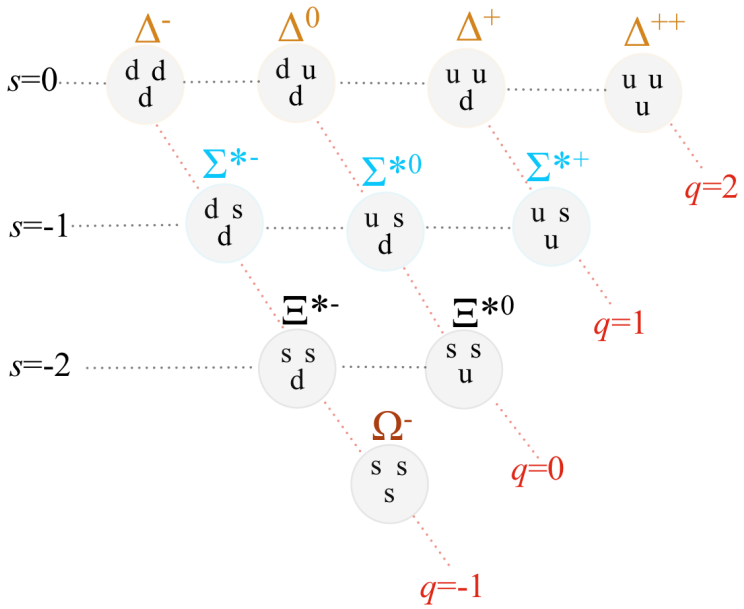


Figure 1.2: The Baryon Decuplet as organized in the Eightfold Way according to charge and strangeness. The decuplet contains spin-3/2 deltas, excited sigmas, excited cascades, and the omega. Quark compositions are additionally shown.

In connection with the Eightfold Way and also ultimately explained by the quark model, the degree of freedom "strangeness" was introduced by Gell-Mann to explain why kaons and hyperons exhibited a suppressed decay. These unusual particles were created copiously in energetic collisions but decayed slowly, which seemed to defy the reversibility of particle interactions. Particles with strangeness typically decay on time scales around $\approx 10^{-10}$s as opposed to the time scale associated with strong and electromagnetic decay of $\approx 10^{-23}$s. The peculiar signature of such particles was broadly explained by the postulate that strangeness is a quantity that is conserved by the underlying processes of hyperon production, but not in the processes behind their decay. We now know that strong and electromagnetic interactions, those responsible for the production of strange hadrons, obey the conservation of strangeness while weak interactions violate the law. Ground state particles that contain a strange quark are kinematically forbidden to decay through processes in which strangeness is conserved, and must instead decay weakly.

All observed hadronic matter has consisted of two or three bound quarks, however further hypothetical mesons and baryons are permitted by the quark model. Pentaquarks, hadrons with an extra quark-antiquark pair (totaling 5 quarks), have been the subjects of rigorous experimental efforts. Although numerous pentaquark observations were reported in the early 2000s [7, 8, 9], all claims have since been discounted upon further statistical analysis [3] and inability to reproduce the results. Still today, new observations of pentaquark states is a subject of controversy but none have been accepted by the nuclear physics community. Ruling out previous pentaquark candidates does not by any means rule out their possible existence. Similarly, mesons with multiple quark-antiquark pairs may exist such as the tetraquark, which has been recently observed [10].

In addition to the hadrons such as the pentaquark and tetraquark, which fall nicely into the quark model classification scheme, several further "exotic" mesons that lie outside the quark model could hypothetically exist. Candidates of exotic mesons include glueballs, which are excited interacting gluons devoid of quarks; a state only possible because of the self-coupling nature of the strong interaction. Other possible states outside of the quark model are the exotic mesons. Exotic or hybrid mesons are a bound quark-antiquark pair in which the binding gluons are in an excited state, augmenting the total meson mass and altering its spin and parity quantum numbers. A significant amount of experimental effort has been devoted to the search for exotic mesons at the Thomas Jefferson National Accelerator Facility (Jefferson Lab, or Jlab). Jefferson Lab's GLUEX collaboration has the principal aim of producing exotic mesons by exciting a proton target with a photon-beam.

The Standard Model's demonstrable success and broad range of application, along with rigorous endeavors probing its theoretical self-consistency, places it among the most successful and sweeping theories in the history of ideas. The Standard Model

does however, fall short of being complete. Among the more prominent problems with the model, many lie with the fact that it not well incorporated with the general relativistic formulation of gravity, which itself is a well-established theory. As previously mentioned, the standard model does not, at present, extend its quantum field characterization to gravitational interaction via gauge boson exchange successfully. Furthermore, there is reason to believe other forms of matter outside of the standard model exist. Observations of the universe on it's largest scale show an accelerating expansion indicating the manifestation of *dark energy*, which may call for the existence of additional scalar fields. Furthermore, gravitational lensing experiments, galactic rotational curves and velocity dispersions among other observational evidence calls for the existence of extra, non-baryonic matter in the universe that interacts gravitationally, dubbed *dark matter*. Many candidates for dark matter, such as the axion or dark photon, lie outside of the standard model. Another prominent issue within the Standard Model is that it does not correctly account for the non-zero mass of neutrinos or their oscillations.

In addition to a few fundamental problems with the Standard Model, many more of its unanswered questions reside within the phenomenological aspects of QCD. Deciphering the substructure of hadrons remains one of the great unsolved problems in physics. Experimental nuclear physics may address theoretical issues including proton decay, the proton charge radius, the phases of strongly interacting matter, hadronization, and the role of gluon self-interactions in nucleons.

## 1.2 Our Research

In this work we provide the first ever determination of three independent spin observables for the charged cascade ($\Xi^-$) in photoproduction. From the $\gamma p \to K^+K^+\Xi^-$ reaction (shown in Fig. 1.3), we measure the recoiling cascade's induced polarization,

$P$, along with the degree of polarization transfered from the photon, $C_x$ and $C_z$.[1]

Put succinctly, polarization is the projection of a particle's spin (depicted in Fig. 1.4), averaged over a sample, with respect to a quantization axis. Extracting the three polarization observables, $P, C_x$ and $C_z$ constitute measurements of cascade spin projection onto three orthogonal quantization axes. A detailed discussion of the relevant observables the coordinate system is left to Chapter 3.

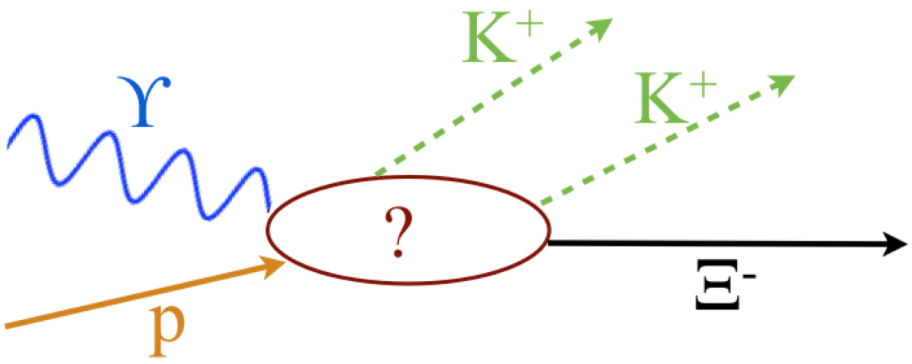


Figure 1.3: The $\gamma p \rightarrow K^+K^+\Xi^-$ reaction through an arbitrary mechanism. At present, the production mechanism which we seek to understand in our work, is unknown.

## 1.3 The Motivation Behind Our Research

The motivation for our research is multifold. One of the most immediate consequences of measuring cascade polarization will be a better understanding of the underlying mechanism behind cascade production, and hence the production of strangeness in general. We intend that the broader influence of our results will help illuminate questions such as:

- What processes underlie the photoproduction of hyperons, particularly the cascade?
- What are the processes responsible for hyperon polarization?

[1]We take on the notational convention commonly used for single meson production. For double meson production, $P$, $C_x$ and $C_z$ are often written as $P_y$, $B_{zx}$ and $B_{zz}$ respectively.

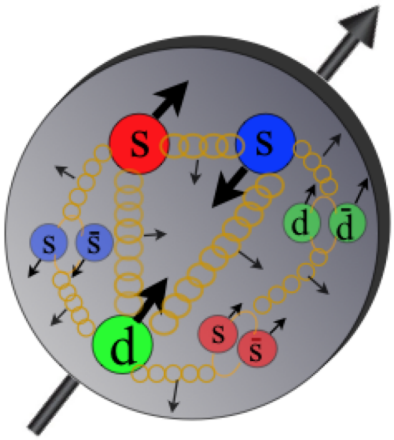


Figure 1.4: Cartoon depiction of the cascade's half-spin arising from its internal constituents and their dynamics. In general, the overall spin comes from quantum mechanical addition rules, summing contributions from valence quarks (*ssd* for the cascade), virtual quark-pairs (sea quarks) and gluons; all three types of constituents contain intrinsic spin, and orbital angular momentum. The relative contributions from each source of spin are unknown, which is in part what the present work examines.

- Which excited baryons contribute most significantly to cascade photoproduction?
- Is photoproduction a feasible means to study cascade spin?

Elaboration on the motivation behind our research is provided in the following subsections.

### 1.3.1 Motivation: Current Status of Cascade Physics

Cascade states ($\Xi$), which contain two strange quarks, are experimentally under explored as compared with the non-strange baryons ($N$ and $\Delta$) and the $S = -1$ hyperons ($\Lambda$ and $\Sigma$). In particular, the production mechanism for ground state $\Xi$ baryons remain unknown, also progress is lacking in the observation of the excited $\Xi^*$ states that are predicted to exist by flavor $SU(3)_F$ symmetry. Flavor symmetry requires a corresponding cascade resonance for each $N^*$ and $\Delta^*$ resonance, the PDG [3] reports

there are around 26 $N$ and $\Delta$'s with a status of 3-star and above. Only six such cascade resonances have been reported with an additional five constituting the resonances with 2- or 1-star status. The abysmal state of global cascade data is largely because of small production cross sections, cascades, having two strange quarks, can only be produced via indirect processes. The little experimental progress that has been made has been insufficient to significantly stimulate theoretical developments, and aside from Ref. [11], most theoretical efforts have been devoted to pentaquark production [12].

At present, there is only one existing publication [13] in which differential cross sections for $\Xi$ photoproduction were measured. The recent results for the $\gamma p \rightarrow K^+K^+\Xi^-$ reaction showed a high probability of the cascade recoiling in the direction of the proton momentum (in the center-of-mass frame); this is usually an indication of $t$-channel production. It was suggested by K. Nakayama [11] that the leading contribution of $\Xi$ photoproduction comes through meson exchange and intermediate $S = -1$ hyperon resonances, as depicted (for $t$-channel) in Fig. 1.5. It is natural to assume singly strange intermediate hyperons for the reaction, because otherwise, the it would involve a $t$-channel exchange of S=2 exotic mesons. The model of Ref. [11] was the only production model available for comparison, which, matched the experimental cross-section results fairly well. The results of Ref. [13] did not include any polarization measurements, though it was pointed out that contributions from various hyperons states can be differentiated using the $\Xi^-$ spin observables [14]. We seek to provide the first of much needed $\Xi^-$ polarization observables, which will help determine the mechanisms behind photoproduction of strangeness and the hadronic processes that give rise to hyperon polarization.

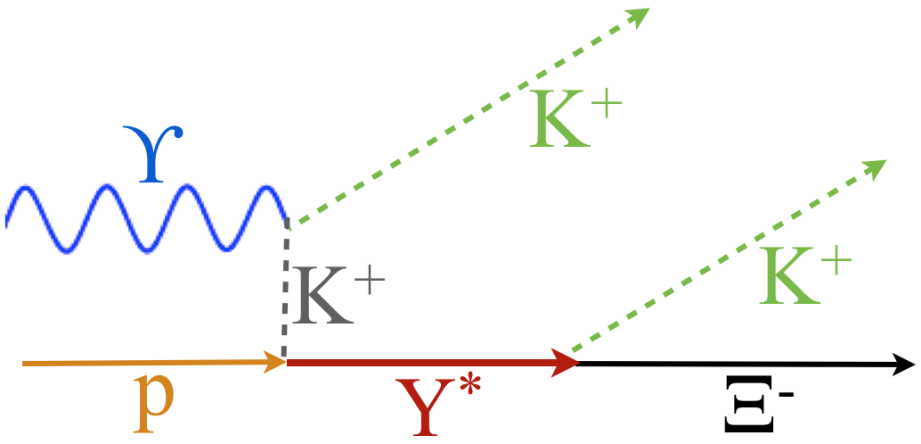


Figure 1.5: An illustration of cascade photoproduction in the $t$-channel, arising through the decay of an intermediate hyperon.

### 1.3.2 Motivation: Testing Predictions from Theory

Just as the $\Lambda$ has been useful in exploring the $S = 0$ baryon resonance structure [15], so too can the cascade be used as a sensitive probe for hyperon resonance contributions. The model mentioned in Section 1.3.1 and detailed in Ref. [11] makes specific predictions for the polarization observables. Such predictions turn out to have a high sensitivity to the relative contributions from intermediate hyperon resonances. Only the resonances with sufficient existing information to determine the hadronic and electromagnetic coupling constants, shown in Table 1.2, were included. The model is based on a relativistic meson-exchange of hadronic interactions where the production amplitudes are calculated from the relevant effective Lagrangian in the tree-level approximation. Although the model does not involve loop integration, it is more robust than a typical tree-level calculation in that it accounts for the final state interaction effects through the generalized contact terms which keep gauge invariance of the photoproduction amplitudes. Contributing diagrams to production that are considered in the model are shown in Fig. 1.6.

| Λ states | | | | | Σ states | | | | |
|---|---|---|---|---|---|---|---|---|---|
| State | $J^P$ | Γ (MeV) | Rating | $\lvert g_{N\Lambda K}\rvert$ | State | $J^P$ | Γ (MeV) | Rating | $\lvert g_{N\Sigma K}\rvert$ |
| Λ(1116) | $1/2^+$ | | **** | | Σ(1193) | $1/2^+$ | | **** | |
| Λ(1405) | $1/2^-$ | ≈ 50 | **** | | Σ(1385) | $3/2^+$ | ≈ 37 | **** | |
| Λ(1520) | $3/2^-$ | ≈ 16 | **** | | | | | | |
| Λ(1600) | $1/2^+$ | ≈ 150 | *** | 4.2 | Σ(1660) | $1/2^+$ | ≈ 100 | *** | 2.5 |
| Λ(1670) | $1/2^-$ | ≈ 35 | **** | 0.3 | Σ(1670) | $3/2^-$ | ≈ 60 | **** | 2.8 |
| Λ(1690) | $3/2^-$ | ≈ 60 | **** | 4.0 | Σ(1750) | $1/2^-$ | ≈ 90 | *** | 0.5 |
| Λ(1800) | $1/2^-$ | ≈ 300 | *** | 1.0 | Σ(1775) | $5/2^-$ | ≈ 120 | **** | |
| Λ(1810) | $1/2^+$ | ≈ 150 | *** | 2.8 | Σ(1915) | $5/2^+$ | ≈ 120 | **** | |
| Λ(1820) | $5/2^+$ | ≈ 80 | **** | | Σ(1940) | $3/2^-$ | ≈ 220 | *** | $< 2.8$ |
| Λ(1830) | $5/2^-$ | ≈ 95 | **** | | Σ(2030) | $7/2^+$ | ≈ 180 | **** | |
| Λ(1890) | $3/2^+$ | ≈ 100 | **** | 0.8 | Σ(2250) | $?^?$ | ≈ 100 | *** | |
| Λ(2100) | $7/2^-$ | ≈ 200 | **** | | | | | | |
| Λ(2110) | $5/2^+$ | ≈ 200 | *** | | | | | | |
| Λ(2350) | $9/2^+$ | ≈ 150 | *** | | | | | | |

Table 1.2: Three-star and above Lambda and Sigma hyper resonances listed by the PDG [3]. Source [11]

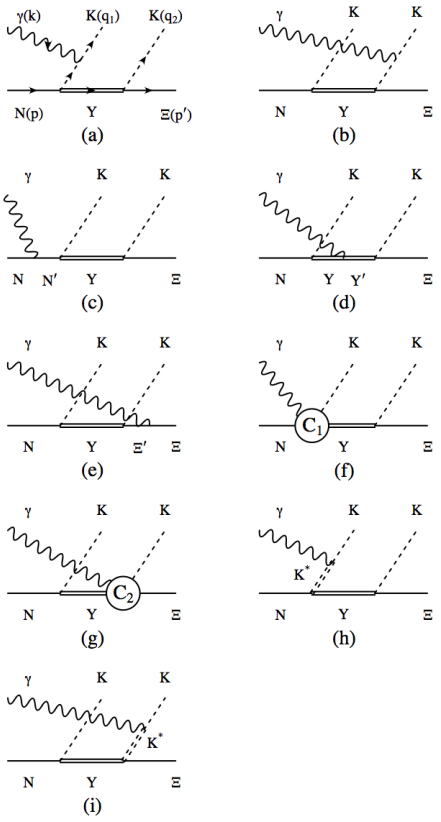


Figure 1.6: Diagrams contributing to cascade production in the model of [11].

More recently, the model of Ref. [11] has been appended in Ref. [14] to include the $\Sigma(2030)$, a four-star hyperon resonance with spin-7/2. The motivation for inclusion of higher spin resonances came from a discrepancy with experimental data reported by Ref. [13]. In this work, a comparison of experimental and theoretical results for $\Xi^-$ polarization observables will be made to constrain the production model. There are three variants on the cascade photoproduction model available for comparison, a summary of the variants is given below:

1. Pure pseudoscalar coupling with intermediate hyperons up to the $\Lambda(1890)$.
2. Pure pseudovector coupling with intermediate hyperons up to the $\Lambda(1890)$.
3. Pure pseudovector coupling with intermediate hyperons up to the $\Sigma(2030)$.

Polarization predictions for all three variants were compared with our results.

### 1.3.3 Motivation: Recent Analogous Lambda Results

Surprising experimental results have been reported by Bradford and Schumacher in Ref. [15] regarding the measured $\Lambda$ polarization in the reaction $\gamma p \to K^+\Lambda$. The spin observables they measured, $C_x$ and $C_z$, determined the polarization *transfered* from the photon-beam, to the recoiling $\Lambda$ in the $x$ and $z$ directions, respectively. Together, $C_x$ and $C_z$ measure the full polarization transfer, and, when taken along with the *induced* polarization ($P$), they constitute a basis for complete characterization of the $\Lambda$ spin orientation. For an elaboration on observables $C_x$, $C_z$ and $P$, see Chapter 3. It was reported that a remarkably large probability of spin transfer was found for all kaon angles and all beam energies for the experimental energy range $1.7 < W < 2.3$ GeV[2]. The integrated results showed, when combined with previous measurements of

[2] $W$ denotes the center-of-momentum (frame of reference with zero total momentum) energy in the initial state, which is the amount of energy available to produce the final state particles.

induced polarization $P$, that,

$$\bar{P}_\Lambda \equiv \sqrt{C_x^2 + P^2 + C_z^2} = 1.01 \pm +0.01, \tag{1.2}$$

which is consistent with unity to within high precision. Such findings show that for production with a fully polarized photon-beam, whichever processes may be contributing to production, the $\Lambda$ would be produced with 100% polarization. Notably, not a single preexisting model of the production process was in agreement with such results. As many as six highly developed theoretical models were compared with the data, all of them failed to describe the observations [16].

In Ref. [16], Schumacher explains his results with an ad-hoc hypothesis invoking *vector meson dominance*, which postulates the photon has a hadronic component, and *diquark* considerations, which, roughly speaking, models baryons as being composed of a quark bound with a spin-zero double quark. In his explanation, the incoming photon spontaneously produces a $\phi$ ($s\bar{s}$ quark pair), as shown in Fig. 1.7. The produced $s\bar{s}$ pair separates and interacts with the proton, undergoing hadronization into a $K^+$ and $\Lambda$. In this picture, the polarization of the $s$ quark is preserved after it is precessed by a spin-orbit interaction. The $ud$ quark pair within the $\Lambda$ is the main diquark component, being the only possible spin and isospin zero quark pair. Such a scenario leaves the polarization of $\Lambda$ dominated, presumably, from the polarization of the $s$ quark. One of the issues with Schumacher's hypothesis however, is that it contradicts the well known contribution of $N^*$ resonances to the production of $\Lambda$. Anisovich pointed out in Ref. [17] that by invoking contributions from the $N(1900)$ resonance, a quantitative description of $\Lambda$ data could be obtained through the conventional isobar picture.

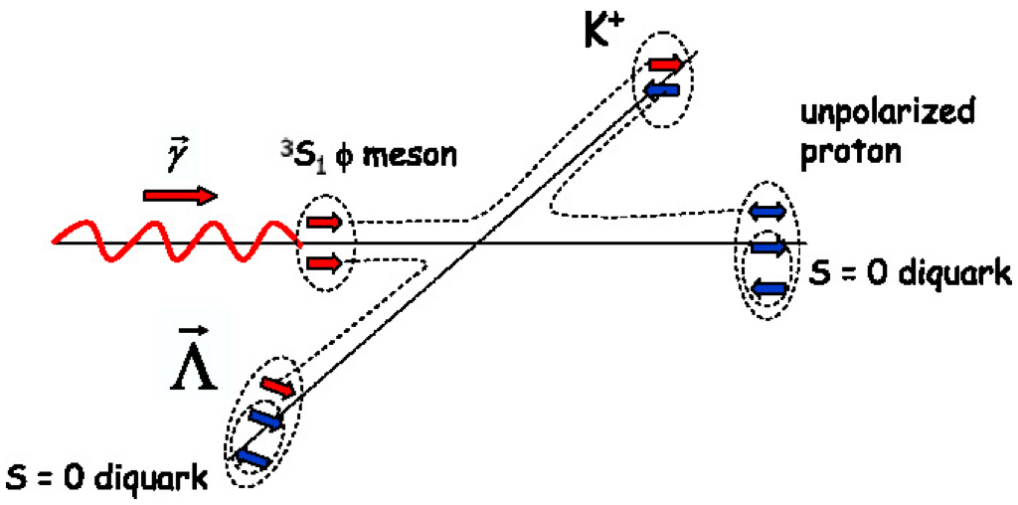


Figure 1.7: An illustration of Schumacher's hypothesis. Image source [16]

Although there is still some uncertainty regarding the production mechanism for the $\Lambda$, great progress has been made as a result of the aforementioned spin observable measurements. Collectively, cross section and polarization measurements [18, 15] were necessary to identify the various mechanisms for $\Lambda$ production, including the identification of numerous intermediate excited nucleon ($N^*$) resonances. We seek to make analogous measurements for the $\Xi^-$ to explore production and the contributing $S = -1$ hyperon spectrum. We expect results for the cascade to differ greatly from that of the $\Lambda$ due to fundamentally differing production mechanisms and diquark configurations.

### 1.3.4 Motivation: Vector Meson Dominance

[h] The total constituent quark wave function for the $\Xi^-$ is [19],

$$\psi_{\Xi^-} = \frac{1}{\sqrt{18}}[2(s\uparrow d\downarrow s\uparrow) + 2(s\uparrow s\uparrow d\downarrow) + 2(d\downarrow s\uparrow s\uparrow) - (d\uparrow s\downarrow s\uparrow) - (s\uparrow d\uparrow s\downarrow)$$
$$- (s\downarrow d\uparrow s\uparrow) - (s\uparrow s\downarrow d\uparrow) - (d\uparrow s\uparrow s\downarrow) - (s\downarrow s\uparrow d\uparrow)], \tag{1.3}$$

while the wave function for the $\Lambda$ is,

$$\psi_\Lambda = \frac{1}{\sqrt{12}}[(u\uparrow d\downarrow s\uparrow) - (u\downarrow d\uparrow s\uparrow) - (d\uparrow u\downarrow s\uparrow) + (d\downarrow u\uparrow s\uparrow) + (s\uparrow u\uparrow d\downarrow) \\ - (s\uparrow u\downarrow d\uparrow) - (s\uparrow d\uparrow u\downarrow) + (s\uparrow d\downarrow u\uparrow) - (d\downarrow s\uparrow u\uparrow) + (d\uparrow s\uparrow u\downarrow) \\ - (u\downarrow s\uparrow d\uparrow) + (u\uparrow s\uparrow d\downarrow)]. \tag{1.4}$$

We see from Equation 1.4 that the constituent quark model predicts that the majority of the lambda's spin comes from the $s$-quark, since the $u$- and $d$-quarks are anti-aligned with one another. We point out that in the aforementioned vector meson dominance picture of lambda photoproduction, the diquark considerations need not be invoked to explain its large total polarization, since either way, the $s$-quark is the main contributer to the lambda's spin.

The wave function for the cascade however, shown in 1.3, yields a more intricate spin structure. With vector meson dominance, one of the two $s$-quarks within the cascade has its origin from the photon, so one might expect the cascade to have similar polarization features as the lambda, but with a diluted overall magnitude, as can be inferred by comparing Figs. 1.8 and 1.9. The results of our polarization measurements will be compared with qualitative expectations from the vector meson dominance polarization mechanism and compared with previous results of the lambda.

As a side note, if diquark effects are manifest, a measurement of $\Xi^-$ polarization may serve as a sensitive probe of it's $d$-quark spin contribution. The cascade's only possible isospin-zero quark pair is the $ss$, where the spin-zero configuration dominates over the spin-one configuration [20]. In this picture, the majority of cascade polarization comes from the $d$-quark, which is likely inherited from the initial state proton target (see Fig. 1.9). In this case, experiments with target polarization would be interesting.

For the present work, where the proton is unpolarized, we might expect a small total cascade polarization, with little kinematic dependence, associated with strong diquark correlations.

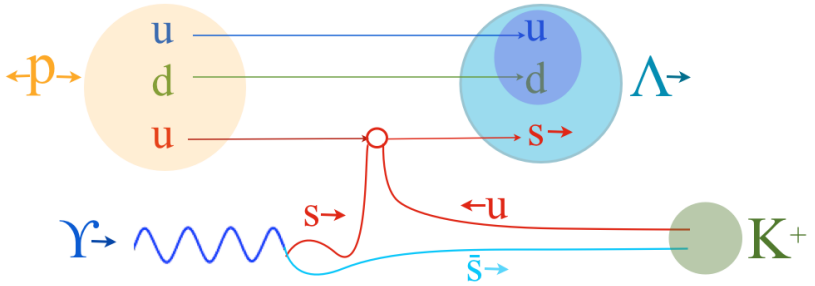


Figure 1.8: Cartoon depiction of lambda photoproduction through vector meson dominance. In this picture, the polarization of the lambda comes from the strange quark, which is produced through quantum fluctuations of the photon. Most of the photon polarization transfers to the lambda in this picture.

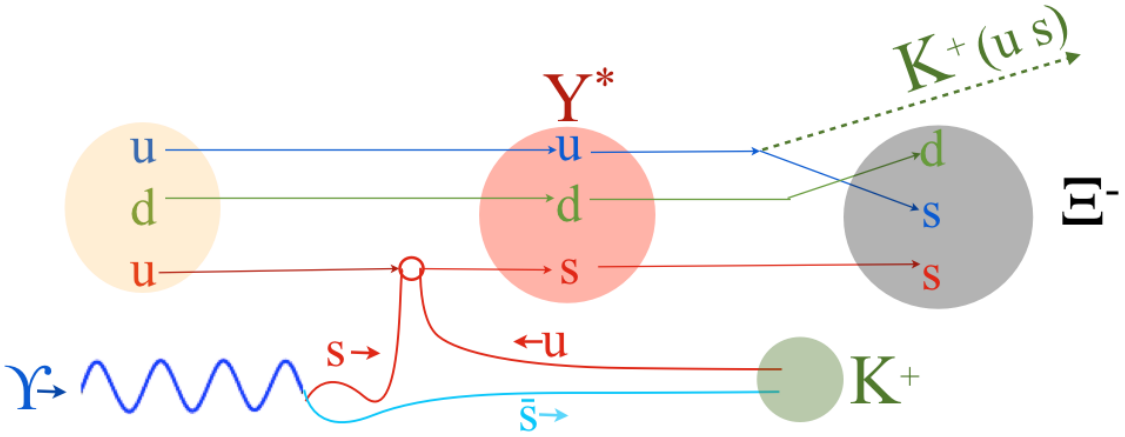


Figure 1.9: Cartoon depiction of cascade photoproduction through vector meson dominance. In this picture, the polarization of the cascade comes from the strange quark, which is produced through quantum fluctuations of the photon. While the strange quark from the photon may be fully polarized within the cascade, its effects are diminished since it may only contribute a fraction to the total cascade spin. Thus, only some of the photon polarization transfers to the cascade.

### 1.3.5 Motivation: Universal Hyperon Polarization at High Energies

[h] Polarization is a coherent phenomenon that depends on the interference of complex amplitudes. In reactions with energies well above threshold, there are a large number of available amplitudes, with different phases. Because of the presumed cacophony from the addition of the various phases, it was expected that no polarization would be observed for hyperons from reactions around 10 GeV above their threshold energy. The 1976 discovery [21] at Fermilab of non-zero induced (or transverse) $\Lambda$ polarization in baryon-baryon collision at 300 GeV was highly unexpected. Since the discovery, a considerable experimental effort has been underway to characterize the polarization of all the hyperons. As it turns out, $\Lambda, \Sigma^0, \Sigma^-, \Sigma^+, \Xi^0$ and $\Xi^-$ are all produced polarized.

The most basic applications of perturbative Quantum Chromodynamics (pQCD), which assume massless quarks, predicts no polarization at high energies. On the other hand, recent developments in pQCD do in fact exhibit non-zero hyperon polarization, however the predictive power of such theories are limited. At present, hyperon polarization is still mysterious and there is no model that can explain the observations.

Although high energy cascade experiments have been extensively conducted, where partonic effects dominate, no one has explored cascade polarization near threshold, in the hadronic regime. The data in the present work provides a unique opportunity to study cascade polarization in this unexplored region.

### 1.3.6 Motivation: Connection Between Polarization Observables and Production Amplitudes

[H] Single pseudoscalar-meson photoproduction off nucleons is fully described by four complex amplitudes. The bilinear combinations of these amplitudes enumerate a total of 16 observables [22, 23]. As it turns out, of these 16 observables, seven are needed to determine the amplitudes up to discrete ambiguities (and an overall phase), known as a *complete experiment*. It is also known that two further measurements (totaling nine) are sufficient to eliminate all ambiguities (up to an overall phase) [22]. The set of observables necessary for an amplitude analysis has been shown to include the differential cross-section, $\frac{d\sigma}{dt}$, and three single-polarization observables; namely the polarized photon-beam asymmetry, $\Sigma$, the target-polarization asymmetry, $T$, and the *induced* baryon recoil polarization $P$. The twelve remaining unique quantities are double polarization observables that characterize the reactions under different combinations of beam, target, and baryon recoil polarization. The double polarization observables can be categorized into three groups of four, beam-recoil (BR), target-recoil (TR) and beam-target (BT) observables. The remaining three measurements, which are necessary and sufficient to uniquely determine the underlying complex amplitudes up to discrete ambiguities, include any three of the double polarization observables, so long as the measurements belong to more than one group. For the elimination of discrete ambiguities, the measurement of two more double polarization observables suffices provided that no four measurements come from the same group [22, 23, 24].

Similar requirements for complete experiments have been formulated in Ref. [25] for the case of two pseudoscalar photoproduction off a nucleon. It was shown for double meson production that one needs at least 15 observables to constitute a complete experiment. Current theoretical efforts are underway with the intention of charac-

terizing complete experiments with a further reduction of observables. For cascade photoproduction, no polarization observables have been measured to date. The current research, measuring three of the needed polarization observables, $P, C_x$ and $C_z$, in the energy range from 2.8 GeV $< E_\gamma <$ 5.5 GeV. While the realization of a complete measurement is still infeasible with current nuclear physics instrumentation, there is much to be learned along the way, and polarization observables provide detailed information on the interference of the production amplitudes. Many $\Lambda$ and $\Sigma$ resonances have been observed and studied, but there are still large gaps to close in the world database regarding the spectrum of possible hyperon states and their properties.

### 1.3.7 Proton Spin Crisis and Baryon Polarization

In the naive quark model, the nucleon consists of three bound, spin-half valence quarks which gives rise to a rather simple spin structure: the one-half overall spin of the nucleon should arise solely from the alignment of two valence quarks with the remaining quark in an anti-aligned configuration. In this picture, non-contribution from orbital angular momentum to the nucleon is assumed since its stability suggests that it occupies the lowest possible energy state, hence having a total orbital angular momentum of zero.

An experiment carried out in 1987 at the European Muon Collaboration (EMC) [26] found that, contrary to widespread expectations from the naive quark model, the valence quark spin contribution to the total spin of proton was $20 \pm 20\%$, which was not only far smaller than 100%, but consistent with 0% [26]. The mysterious result coined the *proton spin crisis* or *proton spin puzzle* prompted an ongoing and vigorous attempt within the nuclear and particle physics community to understand the spin structure of the proton. Today, a quarter-century after the EMC results were published, the proton spin puzzle is largely resolved, although still not in its entirety.

Physicists realized that in order to decipher the spin structure of the nucleon, a more complete quantum chromodynamical model must be considered with non-zero orbital angular momentum. In this model, the nucleon's spin comes from it being made up three constitute quarks along with mediating spin-1 gluons in addition to virtual quark anti-quark pairs that arise from quantum fluctuations. More exactly, the postulated spin originating from four basic components is given as,

$$\frac{1}{2} = \frac{1}{2}\Sigma + G + L_q + L_g. \tag{1.5}$$

Each term from left to right (on the right-hand-side) represents the spin component of the quarks, gluons, followed by the angular momentum component of the quarks and gluons. The quark spin component can be further decomposed into separate quark contributions,

$$\Sigma = (\Delta u + \Delta d) + (\Delta \bar{u} + \Delta \bar{d}) + (\Delta s + \Delta \bar{s}) + ... \tag{1.6}$$

where the unincluded remaining terms in the sum consist of spin components from the heavier quarks, from which contributions should be negligible due to their large masses and resulting sparsity in the nucleon.

Current world data, accumulated over a period of 27 years, suggests that the quark-spin contribution term is no longer consistent with zero, having a value of, [3]

$$\frac{1}{2}\Sigma \approx 0.33 \pm 0.05. \tag{1.7}$$

The measured value of the quark-spin contribution reduces the nucleon's proportion of *missing* spin to be on the order of 66%. Recent experiments seem to indicate that most of the quark spin contribution comes from valence quarks, and very little is from

the quark sea [27]. Additionally, experiments have also shown that the gluon spin term $G$, may account for up to 50% of the missing nucleon spin [27]. The remainder of the nucleon's missing spin is believed to lie predominantly in the finite orbital angular momentum of the valence quarks.

Although significant experimental and theoretical progress has been made in understanding nucleon's spin structure, the proton spin puzzle continues to be considered as one of the most important unsolved problems in the field of physics. Some remaining unanswered questions include:

- What are the underlying factors that determine the relative contributions to the total spin of the nucleon?
- Why does the quark spin contribute so little?
- Does the missing proton spin arise due to effects from valence quarks, sea quarks or gluons?
- Is it possible to separate the quark and gluon orbital angular momentum contributions from experiments in a model-independent way?

Further questions can be asked relating the study of hyperons to the spin puzzle which include,

- Do the heaver quarks, particularly strange quarks, contribute to the spin structure of the nucleon?
- Are the strange quarks themselves polarized within the nucleon?
- Are the spin structures of ground-state hyperons similar to what the naive quark model suggests?
- Is the spin structure of ground-state hyperons different from that of the nucleon?

- Can the individual valence up and down quark contributions be separated through the photoproduction of hyperons off polarized a nucleon target?

Results of the present analysis when combined with similar future experiments in CLAS12, involving large amounts of data and target polarization could shed light on a number of the above questions. Target polarization measurements in particular could help decipher the separate contributions of the up and down valence quarks in the nucleon.

# Chapter 2

## The g12 Experiment

The data analyzed in this work, collectively known as g12 (or E04-005), were collected at Thomas Jefferson National Accelerator Facility (Jefferson Lab) using the CEBAF Large Acceptance Spectrometer (CLAS). The g12 dataset is, at present, the world's largest for meson photoproduction in its energy range and provides a unique opportunity to study the cascade. Physics events were generated in 2008 using a circularly polarized photon beam incident on a 40-cm unpolarized liquid-hydrogen target. The photon beam was produced through a bremsstrahlung process using a 5.71 GeV electron beam provided by Jefferson Lab's Continuous Electron Beam Accelerator Facility (CEBAF). The main component of CLAS is a superconducting toroidal magnet coupled with multi-wire drift-chambers, which track the charged particles emanating from the nuclear reactions of interest and enable momentum reconstruction. The other components of CLAS are mostly utilized to obtain particle identification and timing information. Since the time of the g12 data collection, CEBAF has undergone an upgrade doubling the electron energy, enhancing or replacing preexisting spectrometers, and adding a fourth spectrometer (GLUEX). Laboratory conditions at the time of data collection will be described.

## 2.1 CEBAF Accelerator

CEBAF was built to provide a platform for scattering experiments to explore the rules governing the interaction between quarks. The accelerator was engineered to provide a high quality, continuous-wave electron beam with up to 80% polarization, energies up to 6 GeV, and currents up to 200 $\mu$A. The design makes use of superconducting niobium radio-frequency (SRF) cavities to provide the acceleration gradient. After

construction, CEBAF was the world's only accelerator to implement superconducting niobium technology. Earlier accelerators used non-superconducting copper cavities, which due to resistive heating, would have been economically impractical to power under CEBAF's quality specifications. A photograph of a cavity used at CEBAF is shown in Fig. 2.1

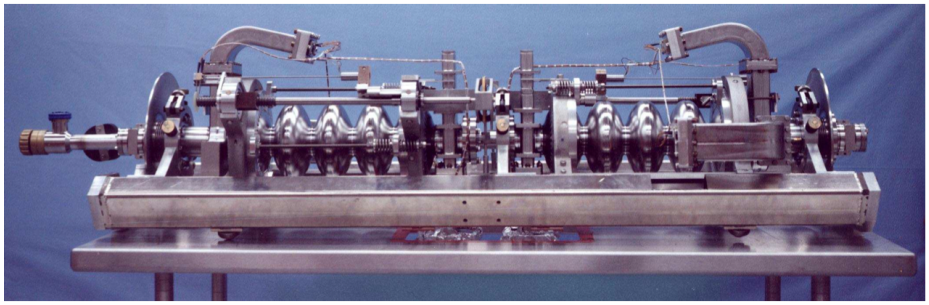

Figure 2.1: A photograph of an SRF cavity made from superconducting niobium. As electron clusters travel through the cavity, they experience a continuous acceleration due to a standing electromagnetic wave. The energy resonances can be tuned by mechanically adjusting the cavity lengths. Image source [28].

The large-scale design of CEBAF comprises two linear accelerators (linacs) connected by arcs at either far end, reminiscent of a racetrack, as shown in Figs. 2.2 and 2.3. Electrons are first produced by a laser incident on a photo-cathode and are injected into the linac. The cavity geometry of each linac results in electron bunches approximately 90 $\mu$m in length, separated by 667 picoseconds. After each pass through a linac, the electrons enter the recirculation arcs made up of bending magnets. The track that the electron enters within the recirculation arc is determined by it's momentum. The electron bunches increase in energy by 1200 MeV after every lap around the track, completing a full lap up to five times before being delivered to experimental halls. Having a final energy of up to 6 GeV, the beam bunches are injected sequentially into the halls by the beam switchyard, with a separation between bunches of 2 ns [29, 30, 31].

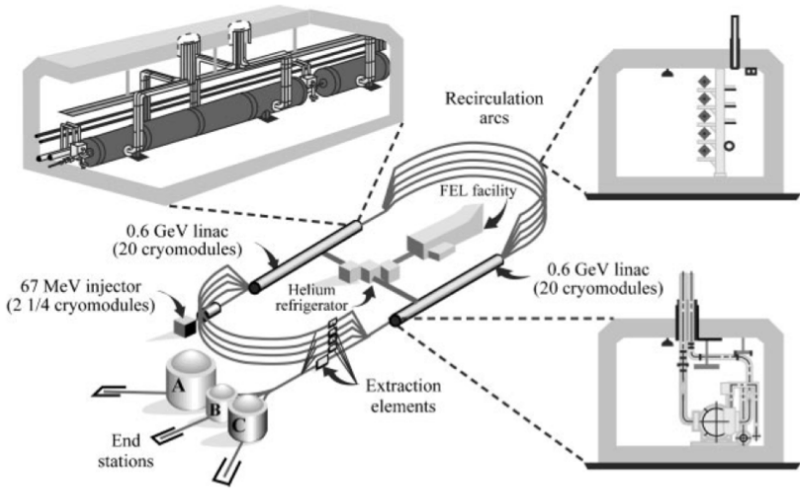


Figure 2.2: The large-scale design of CEBAF and it's components. Image Source [28].

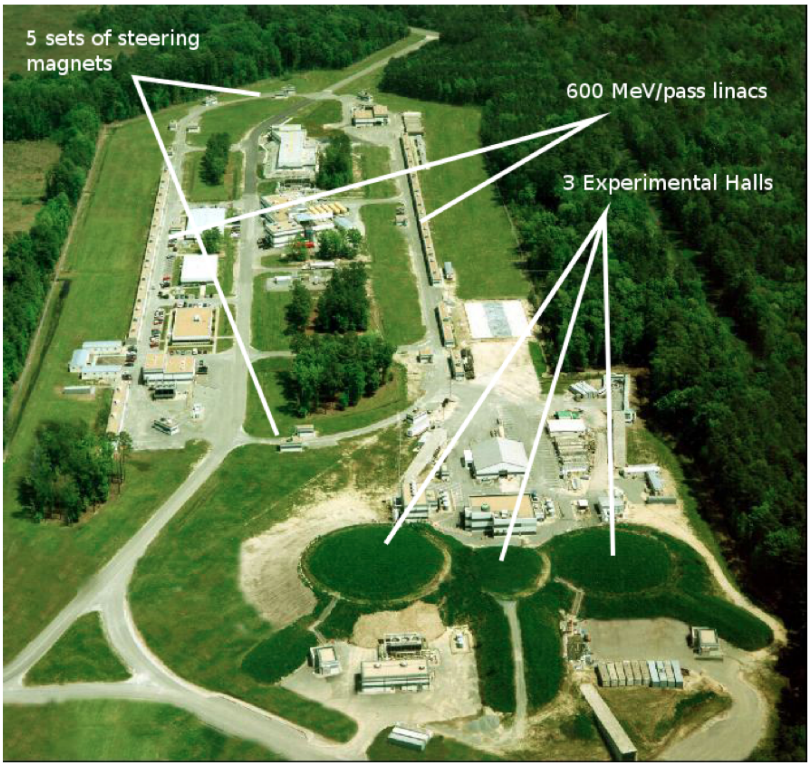


Figure 2.3: An aerial photograph of CEBAF. Image Source [31].

## 2.2 Hall B Photon Tagger

Hall B has a Bremsstrahlung radiator and a photon tagging system know as the "tagger", which is shown in Fig 2.4. The tagger enables scattering experiments using a real photon beam in addition to the electron beam provided by CEBAF. The radiator typically consists of a thin gold target in the path of the electron beam. A dipole magnet produces a 1.75 T uniform field that bends scattered electrons where they are detected by a two-layer set of scintillators. [30, 31, 32]. The position of each scattered electron in is determined by the first layer of scintillators while the timing is measured by the second layer.

The Bremsstrahlung process takes place due to the incident electrons decelerating in the coulomb field of radiator's nuclei, producing a photon in accordance with energy-momentum conservation. The mass of gold nuclei are much greater than the scattered electron mass, hence a negligible amount of momentum is transferred. Thus one can write to high precision,

$$E_\gamma = E_e^i - E_e^f, \tag{2.1}$$

where $E_\gamma$ is the energy of the bremsstrahlung photon, $E_e^i$ is the energy of the incident electron and $E_e^f$ is the energy of the scattered electron, which is measured by the taggers's magnetic spectrometer. The scattered electron position along with knowledge of the magnetic field gives $E_e^f$, while the timing is used to identify which electron bunch created the photon. Tagger timing along with times from particle tracks in CLAS give the time of creation for the photon responsible for the physics event [32].

## 2.3 Hydrogen Target

The g12 experiment used an unpolarized cylindrical target that was 40 cm in length and 4 cm in radius made of liquid hydrogen ($H_2$) and housed in Kapton. The $H_2$ target cell is shown in Figure 2.5

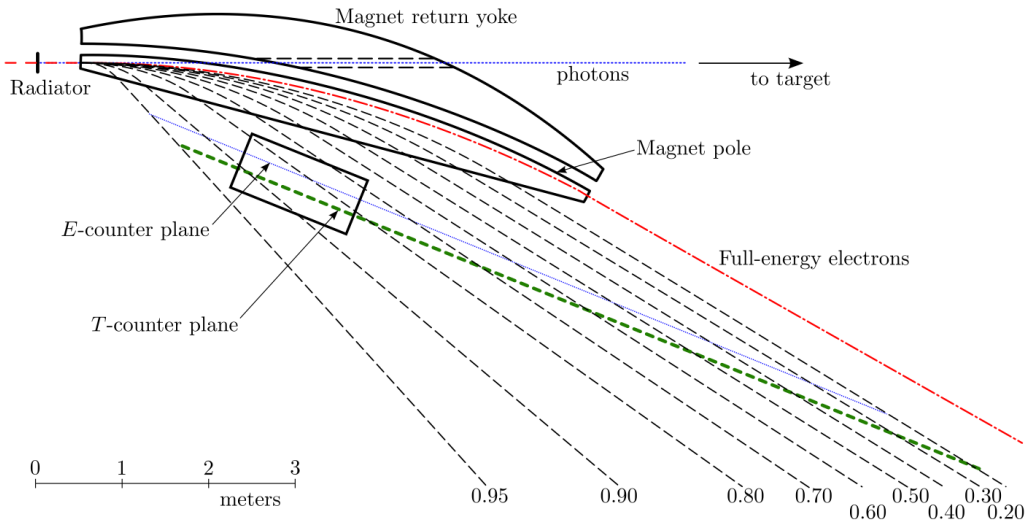


Figure 2.4: A profile of the photon tagger. Incident electrons are scattered in the radiator and then steered by a dipole magnet. Energy and timing information of the scattered electrons are measured by the scintillator array. Image Source [28].

The target was placed 90 cm *upstream* of CLAS's geometrical center. The upstream placement had the advantage that it increased the efficiency of events at small deflection angles by reducing the angular size of the forward hole in the detector. The main drawback to the upstream placement of the target's center was that it caused the drift chamber resolution to suffer as a result of the particle tracks passing on more oblique angles relative to the detector planes [29, 30, 31, 33].

Figure 2.5: A drawing of the target. Image Source [28].

## 2.4 The CLAS spectrometer

The CLAS detector, which is shown in Figs. 2.6 and 2.7, (acronym for the CEBAF Large Acceptance Spectrometer) consists of six sectors segmented in $\phi$ (azimuthal to the beamline). Each sector comprises a four scintillator start counter (ST), three layers of drift chambers (DC), a gas Cherenkov counter (CC), a series of scintillating time-of-flight (TOF) paddles and finally an electromagnetic calorimeter (EC). A magnetic field produced in the $\phi$ direction by a toroidal magnet located in the middle DC layer, bends charged particles toward or away from the beamline (polar angle $\theta$). The magnetic field being solely in the $\phi$ direction forces the trajectory of each charged particle to lay in a plane, allowing for a simplified reconstruction algorithm. Whether inward or outward bending of trajectory takes place depends on the polarity of the toroidal magnet and sign of the particle charge [29, 30, 31, 33].

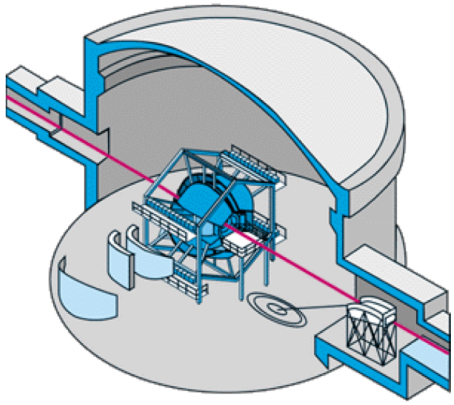

Figure 2.6: Drawing of CLAS nested within Hall B. The electron beam enters the tagger on the right and produces a photon beam. The photon beam continues through the target near the center of CLAS where physics events take place. The photons that do not interact with the target pass through the detector to the main beam dump on the left. Image Source [30]

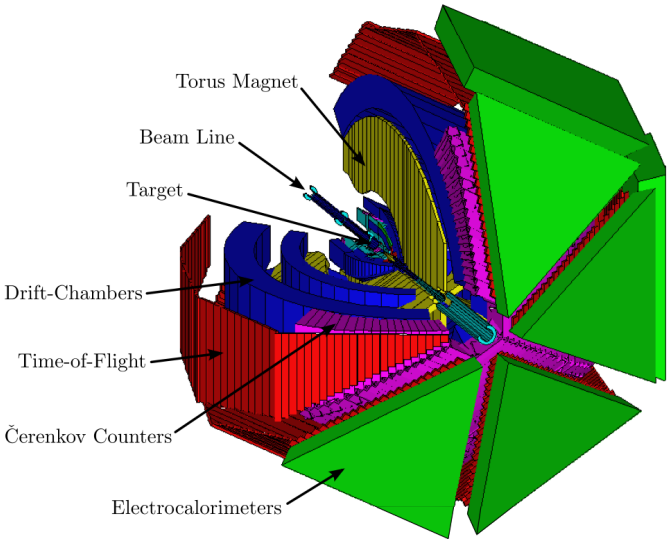


Figure 2.7: Schematic of the CLAS. CLAS is approximately 4 meters in radius. Image Source [28].

## 2.5 Start Counter

The start counter (ST) shown in Fig. 2.8 surrounds the target is the inner-most detector system in CLAS, and is only used in photon-beam experiments. The purpose of the ST is to collect timing information for the outgoing particles emanating from the target. The basic design is a hexagonal array of 24 scintillator paddles. For coverage at smaller angles in $\theta$. The downstream ends of the scintillators are bent inwards converging into a six-sided cone [29].

The start counter provides timing measurements close to the event vertex. It was used in the trigger logic in coincidence with the tagger readout and the time-of-flight readout. Additionally, the start counter helps select the appropriate RF-beam-bucket, which leads to precise measurements of the photon-time, and hence vertex-time. Events with a large number of tracks give better timing estimates since they provide repeated measurements. The hexagonal segmentation of the ST provides flexibility for trigger logic as individual segments can be excluded [29].

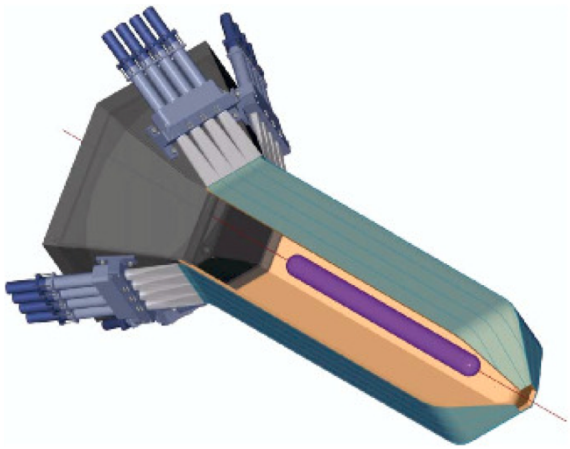

Figure 2.8: A drawing of the CLAS start counter. Image source [28]

## 2.6 Drift Chambers

Each of the six sectors of CLAS contain three large multi-layer drift chambers for tracking charged particles emanating from the event vertex within the target [34]. The geometry of the detector, as shown in Fig. 2.9, provides good tracking resolution, efficiency, and large acceptance [34]. The entire detector contains 35,148 individually instrumented hexagonal drift cells [34]. Fig. 2.10 shows the toroidal magnetic field in relation to the regions of the DC [29].

All regions of the DC contain two *superlayers* as shown in Fig. 2.11 which comprise six layers strung with 20 $\mu m$ diameter gold-plated tungsten sense wires and 140 $\mu m$ diameter gold-plated aluminum field wires [34]. The field wires are arranged to form a hexagon *drift cell* with a single sense wire in the middle as shown in Fig. 2.12. The sense wires receive a current when a charged particle of sufficient energy passes through the DC, ionizing a non-flammable 90% argon 10% carbon-dioxide gas mixture. The ionized electrons are accelerated towards their nearest sense wires by the electric gradient, which is produced by the surrounding field wires [29]. Further details on the CLAS drift chamber can be found in Refs. [29], [34] and [35].

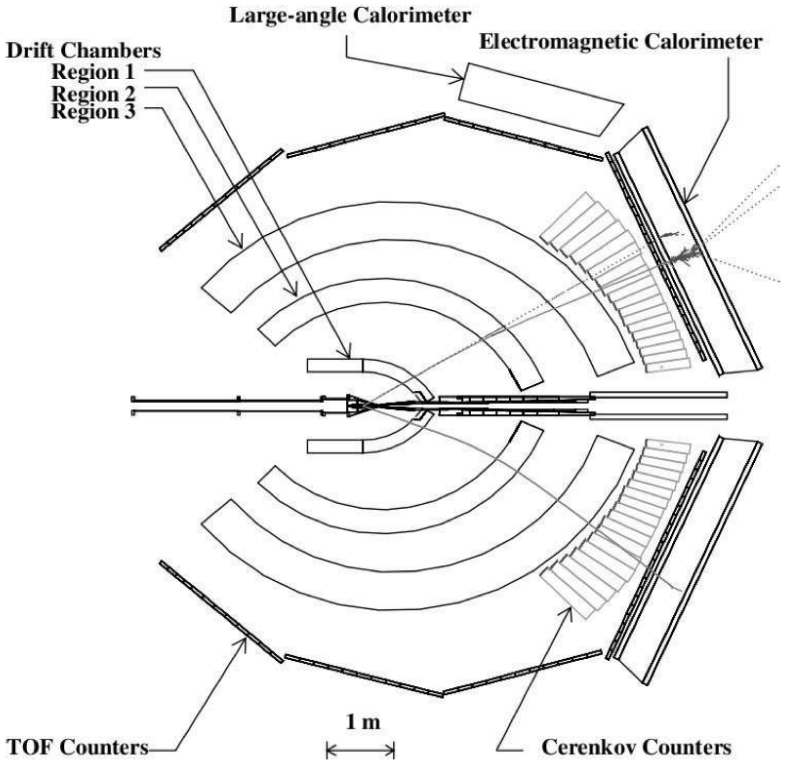


Figure 2.9: A profile drawing of CLAS detecting a two-track event coming from the target. Image Source [31].

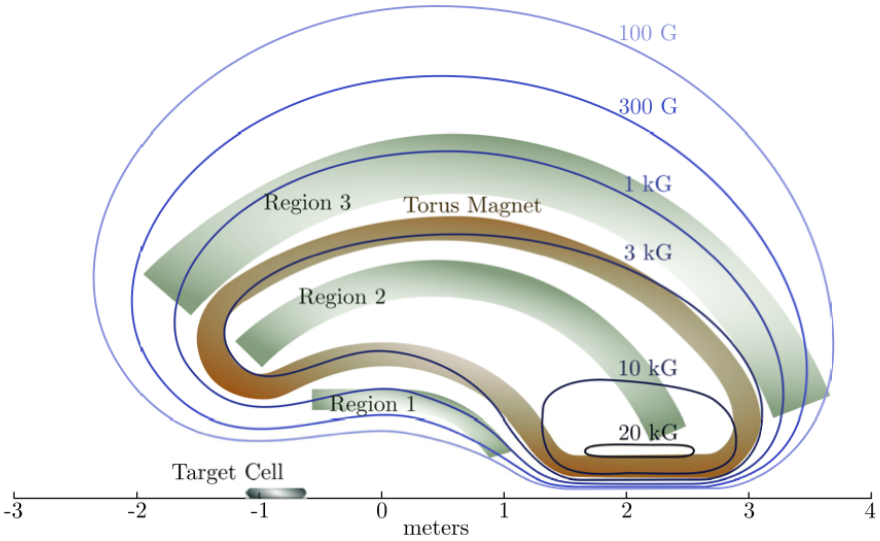


Figure 2.10: Drawing of a cross-sectional view of the DC regions and the toroidal magnetic field at half current (1930 A). Image Source [30]

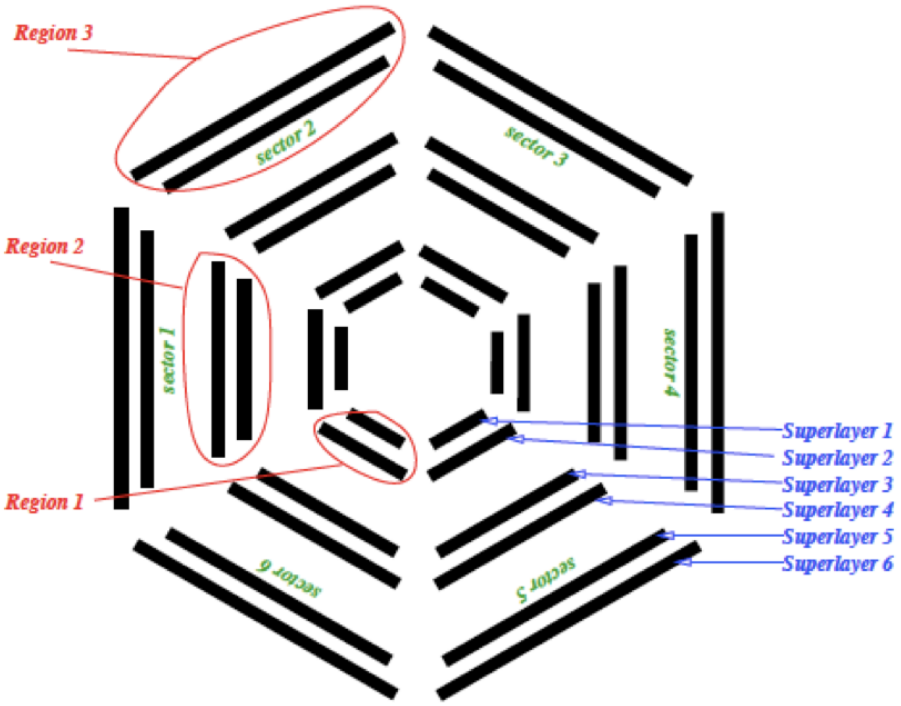


Figure 2.11: Diagram of the sectors, regions and super layers of the DC. Image Source [36]

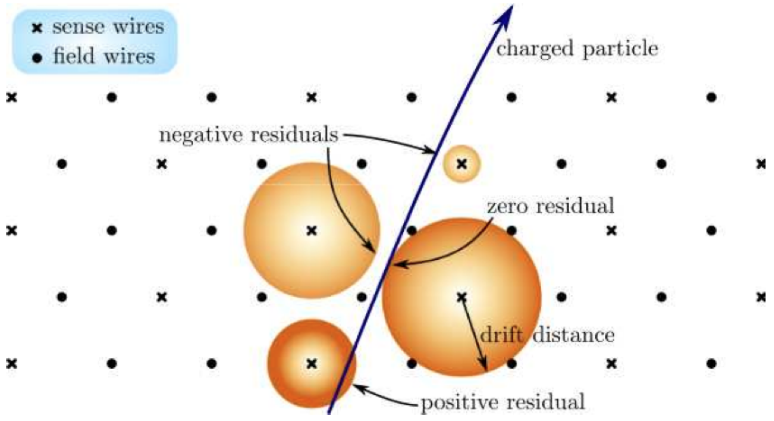


Figure 2.12: Drawing of a track going through the five layers of the DC. Image Source [28]

## 2.7 Superconducting Toroidal Magnet

The toroidal magnetic field in CLAS is produced by six kidney-shaped superconducting coils [29] in between each of the six sectors of the drift-chamber (DC), which can be seen in Fig. 2.7. Each coil consists of four layers of 54 windings of superconducting niobium (NbTi/Cu), stabilized by aluminum [29].

During the g12 production runs, the magnet operated at a current of 1930A (corresponding to half capacity) with a half-maximum field of 1.75 T [18] and a polarity such that negatively charged particles are bent inward towards the beam line. The benefit of running at half field-strength was that it increased the efficiency of detecting negatively-charged particles. Higher field strength tends to bend the inward-going negative-tracks more closely to the "hole" in the forward region where they cannot be detected. The main drawback of the half field-strength operation is that it decreases momentum resolution [31, 29].

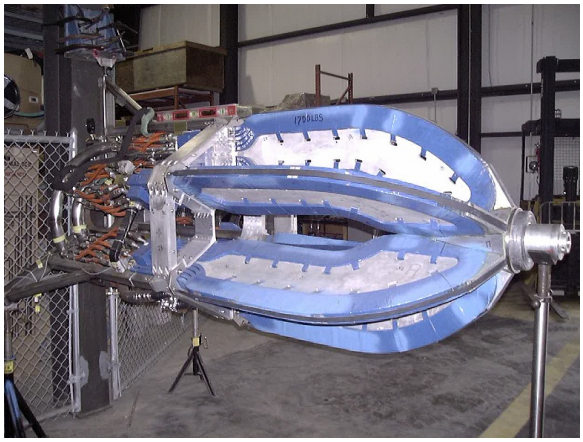

Figure 2.13: Photo of the torus magnet during construction. Image Source [28]

## 2.8 Time-of-Flight Detectors

Accurate time-of-flight information is essential to particle identification. Along with the vertex time, time-of-flight provides a calculation of velocity for each particle. The velocity, in conjunction with momentum from the drift chambers, yields particle

mass, which is used to identify the particle. The CLAS time-of-flight (TOF) detector is a scintillating shell surrounding the Cherenkov counter region about 5 m from the center of the target. Each of the six identical sectors are made up of 57 scintillator paddles of 5.08 cm thickness and various lengths. Each paddle has a PMT attached to both ends. The detector system with nearly 100% efficiency for minimum ionizing particles provides timing measurements with a resolution between 150-200 ps. Timing information from the TOF is integrated with the start counter in the trigger logic [29, 37].

The 57 scintillator paddles are bundled into three groups in lab-frame polar angle ($\theta$):

- $8.6° < \theta < 49.9°$: scintillator 1-23: width = 15 cm
- $49.9° < \theta < 131.4°$: scintillator 24-53: width = 22 cm
- $134.2° < \theta < 141.0°$: scintillator 54-57: width = 15 cm

Further information on the time of flight detectors can be found in Ref. [37].

## 2.9 Cherenkov Counters

The CLAS Cherenkov counter (CC), shown in Fig. 2.14 surrounds the region-three drift chamber and is used exclusively in particle identification for lepton-pion discrimination. The CC is capable of detecting leptons within $8° < \theta < 45°$. As with all CLAS subsystems, the CC is divided into six identical sectors in $\phi$ [29].

Each fixture is filled with a perfluorobutane (C4F10) gas medium with an index of refraction of 1.00153. The velocity of any hadron track with energy less than 2.5 GeV is less than the speed of light in perfluorobutane and thus will pass through the CC without emitting Cherenkov radiation. Leptons, being lighter however, will mostly be traveling above the threshold velocity and thus will emit light and be detected, which provides a means to distinguish between leptons and pion.

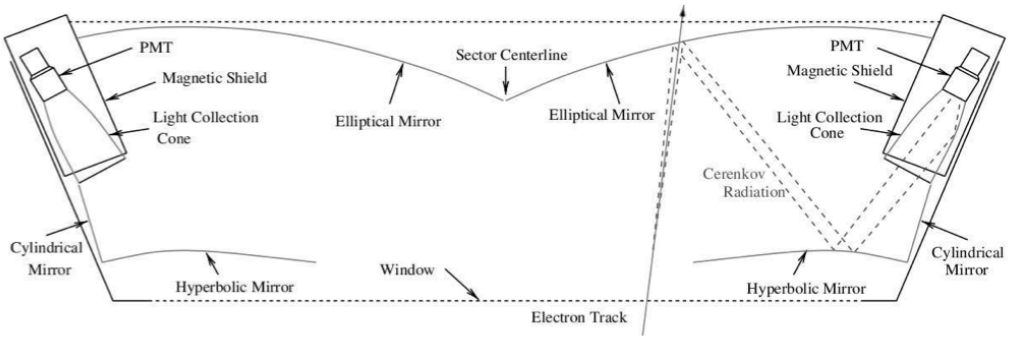


Figure 2.14: A diagram showing the CC response to a single lepton track entering One of the six segments. Lepton tracks emit Cerenkov radiation as they pass through the perfluorobutane (n = 1.00153) gas medium. The Cerenkov light first travels to and is focused by the elliptical outer-surface mirror onto the hyperbolic inner-surface mirror where it is finally directed into one of the photomultiplier tubes at either end of the fixture. Image Source [28]

The Cherenkov detector was not used in the present work. More information on the design and construction of the CC can be found in Ref. [29] and [38].

## 2.10 Electromagnetic Calorimeters

In the very outer layer of CLAS lies the electromagnetic calorimeter (EC) as shown in Fig 2.15. The EC is a 102 ton, six-sector, triangular subsystem composed of 39 alternating layers of lead sheets and 36, 10 mm-wide scintillating bars. Each layer is sequentially rotated by 120° repeating after three layers. The naming scheme for the layers is u-v-w (see Fig. 2.15). The convention provides the ability to make position measurements with a resolution on the order of the scintillator thickness. Since the EC is designed to absorb all of the kinetic energy associated with each particle track, the readout can be related to the total energy of the track. The utility of the EC is multifold: In electron beam experiments, the EC is useful to detect scattered electrons originating from the beam. The EC also provides reliable reconstruction of high energy neutral particles such as photons and neutrons. Furthermore, due to the EC's fast response time, it is useful as input for the trigger logic, which was

it's primary use in g12 [30, 33]. More information on the design, construction, and performance of the EC can be found in Ref. [39].

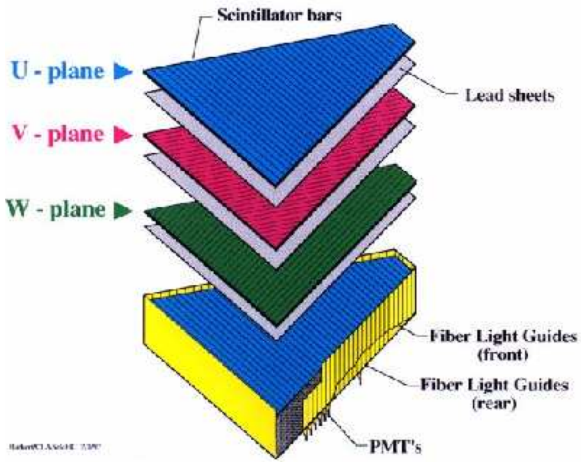


Figure 2.15: A diagram of one dissected sector of the EC with the three u-v-w layering convention illustrated. Image Source [28].

## 2.11 Trigger and Data Acquisition System

The data acquisition (DAQ) used by CLAS is a multi-layer suite of electronics for recording signals in real time. The experimental *trigger* is a user-defined logical set of coupled subsystem signal-criteria, used to distinguish desired events from background. The primary trigger required a 100 ns coincidence between the tagger, ST and TOF, and also requiring two-track events have high incident photon energy [30, 31, 33]. Fig. 2.16 shows an example of the basic trigger logic used in data collection for a single sector. A detailed discussion of the trigger configurations used in g12 is found in Ref. [30].

The g12 experiment recorded events faster than any previous CLAS experiment, with a trigger rate of 8 KHz. As a consequence of the high trigger rate, g12 amounted to the world's largest dataset for the photoproduction of mesons in this energy range; 26B events were recorded, totaling 121 TB of data and an experimental luminosity of 68 $pb^{-1}$ [30, 31, 33].

Signals that pass the trigger are recorded in an *event-based* data format where an event occupies a set time interval. At the end of each event's time interval, the signals from every CLAS subsystem are read out and recorded. After going through a type of high-pass voltage-filter known as a *discriminator* the subsystem signals are digitized by two electronic components: Analog-to-digital converters (ADC), which report the time integral of the signal voltage and time-to-digital converters (TDC), which report the time at which a signal arrives. The digitized data stream is then integrated and written to disk in the event-based data format while being monitored by the DAQ system before being written to a tape-silo for long-term storage [33, 30, 31].

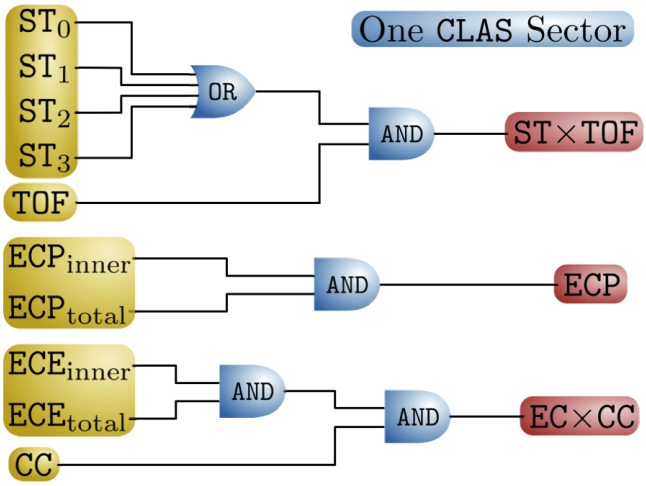


Figure 2.16: Illustrated are three distinct coincidence trigger criteria. $\mathrm{ECP}_{inner}$ and $\mathrm{ECP}_{total}$ represent a photon signal above threshold for the inner layer of the EC and entire EC respectively. $\mathrm{ECE}_{inner}$ and $\mathrm{ECE}_{total}$ represent an electron signal above threshold for the inner layer of the EC and entire EC respectively. $\mathrm{ST}_{0,1,2,3}$ are the four TDC signals for the start counter. Image Source [30]

## 2.12 Event Reconstruction

The toroidal magnetic field geometry allows event reconstruction to be performed in each sector independently since, in general, the particle tracks will not transverse from one sector to the other. Reconstruction is done via hit-based tracking and time-based tracking. Hit-based tracking within the DC is done by finding tracks that produce

aligned clusters of superlayer hits within six layers of the DC in any given region. The segments that align to a physically permissible curve in all three layers are then selected to construct a full track [30, 31, 33]. The curvature of this track gives the magnitude of it's momentum by,

$$p = \frac{l^2 qB}{8s}, \tag{2.2}$$

where $p$ is the track momentum, $l$ is the chord length, $q$ is the charge of the particle, $B$ is the field strength and $s$ is the sagitta length. The chord and sagitta are diagrammed in Fig. 2.17. To further eliminate reconstructed tracks that are not associated with a true particle track, each track is extrapolated back to the TOF detector where only those that have an aligned hit are selected. The time-based tracking refines the momentum and track-path resolution; it limits DC hits, according to its drift time, to those falling within a specified time window [30, 33]. All good tracks are further

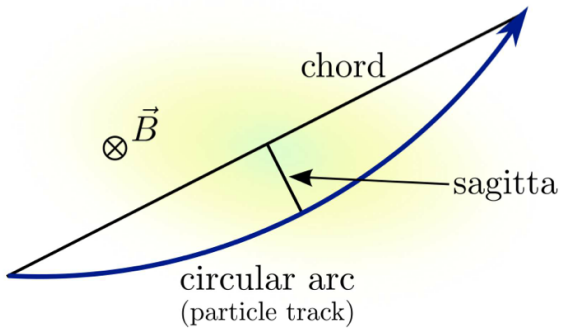


Figure 2.17: The path of a charged particle going through a magnetic field. When the radius of curvature is large when compared with the sagitta, the radius of curvature can be approximated by $r \approx \frac{l^2}{2s}$ where $l$ is the chord length and s is the sagitta length. Image source [30]

extrapolated to the remaining components of CLAS, if hits show up in all components within the appropriate volume, the track is kept.

In the final reconstruction, a known hadronic state is assigned to the track based

on its charge and mass calculation. The measurement of the mass is made through momentum and timing measurements,

$$m^2 = \frac{p^2}{\beta^2}(1-\beta^2) \tag{2.3}$$

with,

$$\beta = \frac{t'-t}{cl}. \tag{2.4}$$

Above, $p$ is the measured momentum, $t'$ is the time of the TOF hit, $t$ is the calculated vertex time and $l$ is the track length from the vertex to the hit TOF paddle. The initial particle identification (PID) is assigned according to the following threshold criteria for the measured mass ($m$),

$$PID = \begin{cases} \pi & m < 0.3 \text{ GeV} \\ K & 0.35 < m < 0.65 \text{ GeV} \\ p & 0.8 < m < 1.2 \text{ GeV} \\ d & 1.5 < m < 2.2 \text{ GeV} \end{cases} \tag{2.5}$$

Tracks with calculated masses outside of the above ranges are not identified[30, 31, 33].

## 2.13 Cascade Data

The g12 data had a total luminosity of 68 pb$^{-1}$. The g12 dataset, is at present the world's largest for photoproduction near its energy range and provides a first time opportunity to study the polarization of the $\Xi^-$ in photoproduction. By detecting $K^+K^+\pi^-(\Lambda)$ in the final state, the full kinematics for the $\gamma p \to K^+K^+\Xi^-$ reaction were reconstructed. After all event selection criteria, we detected a nearly background free signal of approximately 5000 events in which the cascade undergoes the weak decay $\Xi^- \to \Lambda\pi^-$, a globally unprecedented yield. A higher yield for cascade events is possible through the exclusion of pion detection requirements, however the angular

distribution of one of the cascade decay products is necessary to infer its polarization. Although the detection of the pion results in a decreased signal yield because of the decrease in overall efficiency, the pion detection nearly eliminates the background by providing additional kinematic requirements. Extensive details on the method of data analysis are provided in the ensuing chapters.

### 2.13.1 Reconstructed Cascade and Lambda Tracks

The four-vectors of the missing $\Lambda$ and intermediate $\Xi^-$ are reconstructed through energy and momentum conservation. Momentum of the $\Xi^-$ is identified from the missing momentum of the $K^+K^+$ system while the momentum of the $\Lambda$ is identified with the missing momentum of the $K^+K^+\pi^-$ system,

$$\mathbf{p_{\Xi^-}} = \mathbf{p_{missKK}}, \tag{2.6}$$

and

$$\mathbf{p_{\Lambda}} = \mathbf{p_{missKK\pi}}. \tag{2.7}$$

The cascade four momentum is found by,

$$p_{\Xi^-} = \begin{pmatrix} \sqrt{m^2_{\Xi^-} + \mathbf{p^2_{\Xi^-}}} \\ p_x \\ p_y \\ p_z \end{pmatrix}, \tag{2.8}$$

where $m_{\Xi^-}$ is the known mass of the $\Xi^-$, $\mathbf{p_{\Xi^-}}$ represents it's three momentum and $p_x, p_y, p_z$, the Cartesian components thereof. Similarly for the $\Lambda$,

$$p_\Lambda = \begin{pmatrix} \sqrt{m_\Lambda^2 + \mathbf{p_\Lambda^2}} \\ p_x \\ p_y \\ p_z \end{pmatrix}. \tag{2.9}$$

Above, $m_{\Xi^-} = 1.32131 \pm 0.00013$ GeV is the known $\Xi^-$ mass, and similarly $m_\Lambda = 1.115683 \pm 0.000006$ GeV [3]. With knowledge of each four-vector for a sample of $\gamma p \to K^+K^+\pi^-(\Lambda)$ events, the polarization of the $\Xi^-$ can be determined.

# Chapter 3

## Formalism and Methodological Framework

The present work seeks to make a first-time determination of the recoil-polarization $P$, along with the double polarization observables $C_x$ and $C_z$ for the $\Xi^-$ hyperon in the $\gamma p \to K^+K^+\Xi^-$ reaction [1]. Loosely speaking, $C_x$ and $C_z$ measure the degree of polarization transfer from the circularly polarized photon-beam to the $\Xi^-$ while $P$ is a measure of it's induced polarization.

The weak decay of the cascade, as depicted in Fig. 3.1, provides the physical basis for the methods used in extracting our results, which are detailed in the remainder of the current chapter.

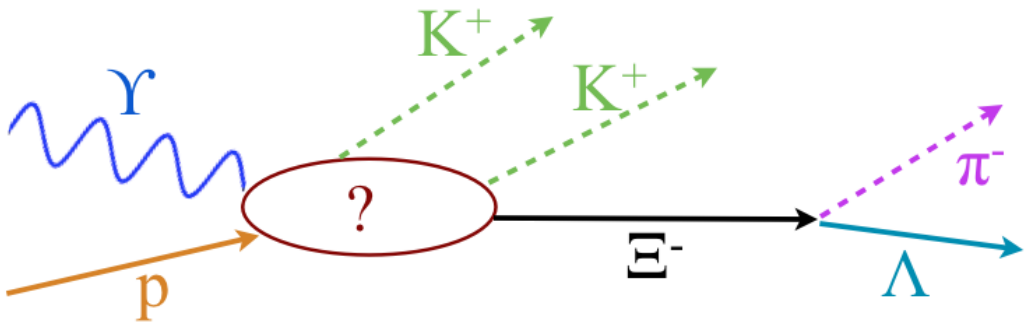


Figure 3.1: The $\gamma p \to K^+K^+\Xi^-$ reaction through an arbitrary mechanism with the subsequent $\Xi^- \to \Lambda\pi^-$ weak decay.

## 3.1 Spin Observables and the Coordinate System

As a consequence of the fact that cascade production occurs via electromagnetic and strong interactions, parity is conserved in the transition from the initial $\gamma p$ state to the final $K^+K^+\Xi^-$ state[2]. The parity conserving nature of cascade photoproduction has

[1] For double meson production, $P$, $C_x$ and $C_z$ are often written as $P_y$, $B_{zx}$ and $B_{zz}$ respectively.

[2] Note that *final state* may refer to either $K^+K^+\Xi^-$ or $K^+K^+\pi^-(\Lambda)$ depending on the context.

an important implication; *induced* polarization is strictly prohibited along vectorial-axes while *transfered* polarization is prohibited along pseudo-vectorial-axes. The last point follows from the respective odd and even parity of vectors and pseudo-vectors and the fact that polarization observables take on the parity of their *quantization* axes. We will choose our coordinates in a way where it is natural to identify the induced and transfered polarizations separately.

For the sake of clarity in defining our coordinates, the reaction may be written in terms of its four-vectors, chosen in the center-of-momentum frame,

$$\gamma(q_1) + p(q_2) \to K^+(k_1) + K^+(k_2) + \Xi^-(p). \tag{3.1}$$

Above, $q_1, q_2, k_1, k_2, p$ represent the four-momenta of each respective particle while their associated three-momenta will be denoted by, $\vec{q_1}, \vec{q_2}, \vec{k_1}, \vec{k_2}, \vec{p}$. For convenience, we will call the four-vector representing our two meson system $k \equiv k_1 + k_2$. The *reaction* or *production plane* contains the proton and the recoiling $\Xi^-$ as shown in Fig. 3.2.

The production plane is defined by the unit vector,

$$\hat{y} \equiv \frac{\vec{q_2} \times \vec{p}}{|\, \vec{q_2} \times \vec{p}\,|}, \tag{3.2}$$

or, the more conventional equivalent,

$$\hat{y} \equiv \frac{\vec{q_1} \times \vec{k}}{|\, \vec{q_1} \times \vec{k}\,|}, \tag{3.3}$$

which is the cross production of the beam and two-kaon momentum. The $\hat{z}$ axis is

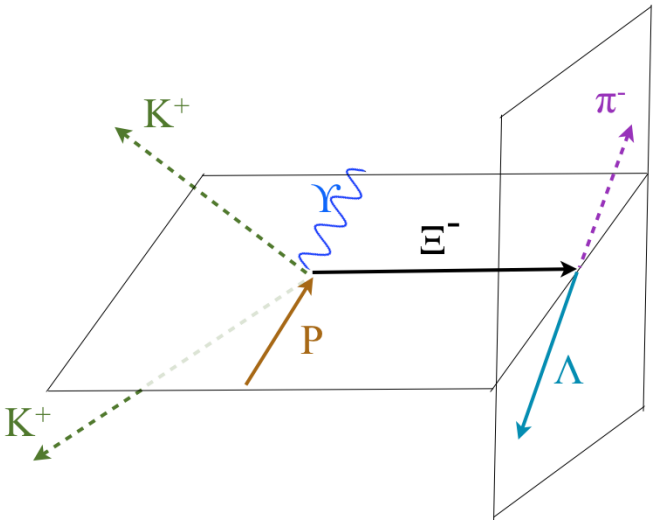


Figure 3.2: The production plane (left plane) is shown; defined in the center-of-momentum, it contains the incoming photon and recoiling cascade. The two kaons in general lie above and below the production plane. The so called *decay plane* (right plane), is defined in the rest-frame of the cascade and contains its decay products (pion and lambda).

defined to be along the photon momentum,

$$\hat{z} \equiv \frac{\vec{q_1}}{|\vec{q_1}|}, \tag{3.4}$$

while $\hat{x}$ is defined to give a right-handed coordinate system,

$$\hat{x} \equiv \hat{y} \times \hat{z}. \tag{3.5}$$

Note that in the above definition of coordinates, $\hat{x}$ and $\hat{z}$ are vectors while $\hat{y}$ is a pseudo-vector. As mentioned, pseudo-vectors remain invariant under parity transformations $\mathcal{P}$. The beam and two-meson momenta have negative parity,

$$\begin{aligned} \mathcal{P}q_1 &= -q_1 \\ \mathcal{P}k &= -k. \end{aligned} \tag{3.6}$$

Thus referring to the above equation and the coordinate definitions we find,

$$\begin{aligned} \mathcal{P}\hat{x} &= \hat{x} \\ \mathcal{P}\hat{y} &= -\hat{y} \\ \mathcal{P}\hat{z} &= \hat{z} \end{aligned} \tag{3.7}$$

The respective parity of each coordinate implies induced cascade polarization is constrained along the pseudovector $\hat{y}$, normal to the production plane. Similarly, polarization transfer to the hyperon is constrained within the production plane, along the vectors $\hat{x}$ and $\hat{z}$. Our polarization results will be expressed in terms of the center-of-momentum coordinate system.

Because of differences in the literature regarding polarization observables, it is important to be clear regarding one's definitions so that meaningful comparisons can be drawn. We follow the convention used by K. Nakayama in [40]. The spin observables, expressed in terms of the reaction's differential cross sections ($\frac{d\sigma_u}{d\Omega}$) are

$$\frac{d\sigma_u}{d\Omega}P \equiv \frac{d\sigma_u}{d\Omega}P_y = \frac{1}{6}Tr[\mathcal{M}\mathcal{M}^\dagger\vec{\sigma}\cdot\hat{y}], \tag{3.8}$$

$$\frac{d\sigma_u}{d\Omega}C_x \equiv \frac{d\sigma_u}{d\Omega}B_{zx} = \frac{1}{6}Tr[\mathcal{M}\vec{\sigma}\cdot\hat{n}_z\mathcal{M}^\dagger\vec{\sigma}\cdot\hat{x}], \tag{3.9}$$

$$\frac{d\sigma_u}{d\Omega}C_z \equiv \frac{d\sigma_u}{d\Omega}B_{zz} = \frac{1}{6}Tr[\mathcal{M}\vec{\sigma}\cdot\hat{n}_z\mathcal{M}^\dagger\vec{\sigma}\cdot\hat{z}], \tag{3.10}$$

where $\mathcal{M}$ represents the amplitude for our reaction and $\sigma_{x,y,z}$ are the usual Pauli spin-matrices, $\sigma_x = \begin{pmatrix} 0 & 1 \\ 1 & 0 \end{pmatrix}, \sigma_y = \begin{pmatrix} 0 & -i \\ i & 0 \end{pmatrix}$, $\sigma_z = \begin{pmatrix} 1 & 0 \\ 0 & -1 \end{pmatrix}$. It follows that the

spin observables are expressed as,

$$P = \frac{\frac{d\sigma}{d\Omega}(+) - \frac{d\sigma}{d\Omega}(-)}{\frac{d\sigma}{d\Omega}(+) + \frac{d\sigma}{d\Omega}(-)}, \tag{3.11}$$

where $\pm$ indicates parallel or anti-parallel spin of the recoil $\Xi^-$ relative to the $\hat{y}$-axis. The beam-recoil asymmetries $C_i$ $(i = x, z)$ are similarly expressed,

$$C_i = \frac{[\frac{d\sigma}{d\Omega}(+,+) + \frac{d\sigma}{d\Omega}(-,-)] - [\frac{d\sigma}{d\Omega}(+,-) + \frac{d\sigma}{d\Omega}(-,+)]}{[\frac{d\sigma}{d\Omega}(+,+) + \frac{d\sigma}{d\Omega}(-,-)] + [\frac{d\sigma}{d\Omega}(+,-) + \frac{d\sigma}{d\Omega}(-,+)]} \tag{3.12}$$

where $(\pm, \pm)$ denotes the (positive/negative) photon helicity and the (positive/negative) helicity of the recoil $\Xi^-$ across the $\hat{i}$-axis respectively.

## 3.2 Connection Between Spin Observables and Polarization

The spin-dependent cross section for the $\gamma p \to K^+K^+\Xi^-$ reaction can be written [15, 16] in terms of the polarization observables as,

$$\rho_\Xi \frac{d\sigma}{d\Omega} = \frac{d\sigma}{d\Omega}|_{unpol}\{1 + \sigma_y P + P_\odot(C_x\sigma_x + C_z\sigma_z)\}. \tag{3.13}$$

$P_\odot \in [-1, 1]$ denotes the degree of circular photon-beam polarization, $\sigma_{x,y,z}$ are the Pauli spin-matrices and $\rho_\Xi$ is two times the density matrix for an ensemble of $\Xi$ hyperons given explicitly as

$$\rho_\Xi = (1 + \vec{\sigma} \cdot \vec{P_\Xi}). \tag{3.14}$$

The $\Xi^-$ recoil polarization and spin observables can be related by equating the expectation value of the Pauli-spin operators acting on the density matrix, i.e. the trace

$\vec{P}_\Xi = Tr(\rho_\Xi \vec{\sigma})$ [15, 16] leading to,

$$\begin{aligned} P_{\Xi_x} &= P_\odot C_x, \\ P_{\Xi_y} &= P, \\ P_{\Xi_z} &= P_\odot C_z. \end{aligned} \tag{3.15}$$

Thus, the induced or $\hat{y}$-component of hyperon polarization $P_{\Xi y}$ is equivalent to the spin observable $P$. The transfered, or $\hat{x}$- and $\hat{z}$-components of the hyperon polarization are equal to $C_x$ and $C_z$ multiplied by the photon-beam polarization $P_\odot$.

## 3.3 Self Analyzing Decay

The connection between the hyperon recoil polarization and the spin observables in Equation 3.15 indicates that knowledge of the beam polarization $P_\odot$, along with a measurement of $\vec{P}_\Xi$, yields $C_x, P$ and $C_z$.

As previously mentioned, there is some confusion in the literature regarding the sign convention for the polarization observables. Part of the confusion involves instances of incorrect quotations for decay angular distributions of hyperons. Consequentially we found it important to explicitly define what is being measured, thus we provide a derivation of the decay angular distribution of the $\Xi^-$.

The $\Xi^-$ recoil-polarization ($\vec{P}_\Xi$) can be measured by exploiting the self analyzing nature of it's decay $\Xi^- \to \pi^- \Lambda$. The relationship between the angular distribution of the decay products and the polarization can most easily be seen by first considering a single $\Xi^-$ prepared in the spin-up state across an arbitrary $\hat{i}$-axis. Consider our initial spin-half particle ($\Xi^-$) prepared at rest, subsequently decaying to a final state consisting of a pseudo-scalar ($\pi^-$) and a spin-half ($\Lambda$) particle. By conservation of total angular momentum, the final state may only have orbital angular momentum $l = 0$ or $l = 1$. For the $l = 0$ (s-wave) final state, the spin of the $\Lambda$ must be spin up

$(X^+)$ and the contribution to its full angular wave function can be written as,

$$\Psi_s = a_s X^+ Y_{00} \tag{3.16}$$

where $a_s$ is the relative amplitude for the s-wave. For the $l = 1$ (p-wave) state, the spin of the $\Lambda$ may be up $(X^+)$ or down $(X^-)$. The p-wave contribution to the total wave function can be written as,

$$\Psi_p = a_p(X^+ Y_{10} C^{\frac{1}{2}1\frac{1}{2}}_{\frac{1}{2}0\frac{1}{2}} + X^- Y_{11} C^{\frac{1}{2}1\frac{1}{2}}_{\frac{-1}{2}1\frac{1}{2}}), \tag{3.17}$$

where $a_p$ is the relative amplitude for the p-wave, and the C variables are the appropriate Clebsch-Gordan coefficients. The total wave function is then the sum of contributions from s and p waves.

$$\Psi_\uparrow = \Psi_s + \Psi_p = a_s X^+ Y_{00} + a_p(X^+ Y_{10} C^{\frac{1}{2}1\frac{1}{2}}_{\frac{1}{2}0\frac{1}{2}} + X^- Y_{11} C^{\frac{1}{2}1\frac{1}{2}}_{\frac{-1}{2}1\frac{1}{2}}), \tag{3.18}$$

or,

$$\Psi_\uparrow = X^+(a_p Y_{10} C^{\frac{1}{2}1\frac{1}{2}}_{\frac{1}{2}0\frac{1}{2}} + a_s Y_{00}) + X^- a_p Y_{11} C^{\frac{1}{2}1\frac{1}{2}}_{\frac{-1}{2}1\frac{1}{2}}. \tag{3.19}$$

The Clebsch-Gordan coefficients and the spherical harmonic functions are given by,

$$C^{\frac{1}{2}1\frac{1}{2}}_{\frac{1}{2}0\frac{1}{2}} = -\sqrt{1/3}, \;\; C^{\frac{1}{2}1\frac{1}{2}}_{\frac{-1}{2}1\frac{1}{2}} = -\sqrt{2/3}, \tag{3.20}$$

$$Y_{00} = 1, \;\; Y_{10} = \sqrt{3}\cos\theta, \;\; Y_{11} = -\sqrt{3/2}e^{i\phi}\sin\theta. \tag{3.21}$$

We may write,

$$\Psi_\uparrow = X^+(-a_p\cos\theta + a_s) + X^- a_p e^{i\phi}\sin\theta. \tag{3.22}$$

By orthonormality of the spin wave functions we have,

$$\Psi_{\uparrow}^2 = |a_s|^2 + |a_p|^2 + (a_p^* a_s + a_p a_s^*)\cos\theta, \tag{3.23}$$

or,

$$\Psi_{\uparrow}^2 = |a_s|^2 + |a_p|^2 + 2Re(a_s^* a_p)\cos\theta. \tag{3.24}$$

By letting,

$$\alpha = \frac{2Re(a_s^* a_p)}{|a_s|^2 + |a_p|^2}, \tag{3.25}$$

where $\alpha$ is known as the analyzing power or decay asymmetry with value of $-0.458 \pm 0.012$ [3], we finally arrive at, after normalization,

$$|\Psi_{\uparrow}(\theta)|^2 = \frac{1}{2}(1 + \alpha\cos\theta). \tag{3.26}$$

One can immediately write the final state wave function corresponding to the case where the initial $\Xi^-$ is prepared in the spin down state by rotating $\theta$ by 180°,

$$|\Psi_{\downarrow}(\theta)|^2 = \frac{1}{2}(1 - \alpha\cos\theta). \tag{3.27}$$

For an ensemble of $N$ cascades with $n_{\uparrow}$ prepared with the spin-up state and $n_{\downarrow}$ prepared in the spin-down state, the total angular distribution of the decay-lambda is given by the weighted sum,

$$n(\theta) = n_{\uparrow}|\Psi_{\uparrow}(\theta)|^2 + n_{\downarrow}|\Psi_{\downarrow}(\theta)|^2. \tag{3.28}$$

By identifying the hyperon recoil-polarization ($P_{\Xi\hat{n}}$) across the $\hat{n}$-axis as,

$$P_{\Xi\hat{n}} = \frac{n_{\uparrow} - n_{\downarrow}}{n_{\uparrow} + n_{\downarrow}}, \tag{3.29}$$

and making explicit that $\theta = \theta_{\Lambda n}$, we arrive at,

$$n(\theta_{\Lambda n}) = \frac{N}{2}(1 + P_{\Xi\hat{n}}\alpha\cos\theta_{\Lambda_{\hat{n}}}). \tag{3.30}$$

Equation 3.30 describes the polar-angular distribution of the $\Lambda$ off the $\hat{n}$-axis in the $\Xi^-$ rest frame and it's relation to the $\Xi^-$ polarization. In order to obtain a similar distribution for the pion, one should recognize that in the $\Xi^-$ rest frame, the pion and the $\Lambda$ are produced back-to-back. This equates to a 180° rotation giving,

$$n(\theta_{\pi_n}) = \frac{N}{2}(1 - P_{\Xi_n}\alpha\cos\theta_{\pi_n}). \tag{3.31}$$

The distribution in terms of the negatively charged pion as opposed to the neutral lambda is more convenient from an experimental stand point since it is generally more easy to detect charged particles. What has been shown is that from the rest frame of the cascade, it's decay angular distribution measured against the previously defined center-of-momentum coordinate-system yields its polarization.

## 3.4 Calculation of $P$

The equivalence of the recoil polarization's $y$-component, $P_{\Xi y}$, and the spin-observable $P$, along with Equation 3.31, allows for a direct measurement of $P$. This can be done multiple ways, one by fitting the acceptance corrected number of events as a function of $\cos\theta_\pi^{\hat{y}}$ to a first-degree polynomial,

$$y = p_0 + p_1\cos\theta_\pi^{\hat{y}}. \tag{3.32}$$

The fitting parameters $(p_0, p_1)$ relate to the recoil asymmetry $(P)$ by,

$$p_1 = \frac{-NP\alpha}{2} \tag{3.33}$$

or,

$$P = \frac{-p_1}{\alpha p_0}. \tag{3.34}$$

The above method requires extensive Monte Carlo simulation, which was carried out to correct for acceptance effects of the detector (see Chapter 5).

Similar to the first mentioned method of measuring $P$, a relation between the $\Xi^-$ polarization and the forward-backward-asymmetry ($A^y$) of the pion angular distribution can be derived. The forward-backward asymmetry is defined as,

$$A_y \equiv \frac{N^{y+} - N^{y-}}{N^{y+} + N^{y-}}, \tag{3.35}$$

where $N^{y+}$ and $N^{y-}$ represent the number of events with $\cos\theta_\pi$ as positive and negative respectively. The relation between induced polarization $P$ and $A_y$ can be seen by considering,

$$N^{y-} = \int_{-1}^{0} n(\theta_\pi)\,\mathrm{d}\cos\theta_\pi = \frac{N}{2}(1 + \frac{\alpha P}{2}) \tag{3.36}$$

and

$$N^{y+} = \int_{0}^{1} n(\theta_\pi)\,\mathrm{d}\cos\theta_\pi = \frac{N}{2}(1 - \frac{\alpha P}{2}). \tag{3.37}$$

Thus the asymmetry can be expressed as,

$$P = \frac{-2A_y}{\alpha}. \tag{3.38}$$

The advantage of using a forward-backward-asymmetry method for calculating $P$ is that, as will be demonstrated with a Monte Caro simulation in Chapter 7, the detector acceptance mostly cancels. The cancellation follows from the polarization axis $\hat{y}$ pointing isotropically in the lab-frame-defined azimuthal angle $\phi_{lab}$ and the geometry of CLAS.

The statistical uncertainty in the asymmetry measurement of $P$ is related to the Poissonian uncertainty in $N^{y+}$ and $N^{y-}$, where for typographical simplicity we momentarily denote as $N_+$ and $N_-$ respectively. Taking the partial derivative,

$$\frac{\partial A}{\partial N_\pm} = \frac{\pm 2 N_\mp}{(N_+ + N_-)^2}, \tag{3.39}$$

we find total statistical uncertainty, through quadrature, is given as,

$$\delta_{A_y} = \frac{2}{(N_+ + N_-)^2}\sqrt{N_-^2 \delta_{N_+}^2 + N_+^2 \delta_{N_-}^2}, \tag{3.40}$$

or,

$$\delta_{A_y} = \frac{2}{(N_+ + N_-)^2}\sqrt{N_-^2 N_+ + N_+^2 N_-}. \tag{3.41}$$

## 3.5 Calculation of Double Polarization Observables $C_x$ and $C_z$

The double polarization observables $C_i$ $(i = x, y)$ characterize the transfered photon helicity to the $\Xi^-$ in the x- and z-directions (represented as $P_{\Xi x}$ and $P_{\Xi z}$). An important experimental aspect is that the photon-beam helicity $P_\odot$ was flipped $(P_\odot \to -P_\odot)$ at a rate of 30 Hz. Assuming equal photon intensities for positive and negative helicity states, there is a net beam polarization of $\bar{P}_\odot = 0$.

There are two ways to measure the transfered polarization. One way is to bin in forward and backward photon helicity bins and fit the acceptance-corrected pion distributions, similarly to how $P$ was measured. However, the need for helicity binning in the mentioned method increases the statistical uncertainty, approximately by a factor of $\sqrt{2}$. Furthermore, the acceptance $(\epsilon(\theta_{\hat{y}}^\pi))$ as a function of pion angle with $\hat{y}$ is much more well behaved than with $\hat{x}$ and $\hat{z}$: while $\epsilon(\theta_{\hat{y}}^\pi)$ is even about $\theta_{\hat{y}}^\pi = 0$, relatively flat and non-zero for all angles, $\epsilon(\theta_{\hat{x}}^\pi)$ and $\epsilon(\theta_{\hat{z}}^\pi)$ are highly asymmetric, non-zero for only a small subset of angles, and contain regions of high gradients. In

fact, measurements of $C_x$ and $C_z$ based on fitting acceptance-corrected pion angular distributions were attempted and proved to be reliable only in the small sub range of pion angles where the acceptance is "well behaved".

The most straightforward and reliable way to extract $C_x$ and $C_z$ employs the photon-helicity asymmetry,

$$A = \frac{N^+ - N^-}{N^+ + N^-}, \tag{3.42}$$

where $N^+$ and $N^-$ are the number of events associated with positive and negative photon-beam helicity states respectively. The form of asymmetry as a function of pion angle can be seen by associating $N^{\pm}$ in Equation 3.42 with $P_{\Xi i} = \pm|P_{\odot}|C_i$ in Equation 3.31 yielding,

$$A(\cos\hat{\theta_{\pi}^{i}}) = -|P_{\odot}|\alpha C_i \cos(\hat{\theta_{\pi}^{i}}) \tag{3.43}$$

Equation 3.43 states that the slope of asymmetry with respect to $\cos(\hat{\theta_{\pi}^{i}})$ is directly proportional to the transfer polarization observable $C_i$. $C_i$ is thus obtained by determining the slope of a two-parameter linear fit to $A(\cos\hat{\theta_{\pi}^{i}})$ in each relevant kinematic bin. The photon-helicity asymmetry method has the benefit that to first approximation, the detector acceptance and various other systematic effects which do not have a photon-helicity dependence cancel.

Monte Caro simulations matching the data showed that the non-cancellation of acceptance had a larger effect for the photon-helicity asymmetry than for the forward-backward asymmetry used to calculate $P$. In fact, acceptance effects turn out to be the largest source of systematic error for the measurement of $C_x$ and $C_z$. For a more detailed discussion on the effect of detector acceptance see Section 3.6 or Chapter 7.

Note that if the photon-beam intensity was not equal for positive and negative helicity phases, there would be a non-zero net beam-polarization. Since this quantity is not

covariant with the pion angle, it does not effect the slope of asymmetry in Equation 3.42, and therefore does not affect the measured values of $C_i$. Similarly, the reaction's intrinsic beam asymmetry $\Sigma$, also being independent of pion angle will not affect the measured values of $C_i$.

## 3.6 Acceptance Independence of $C_x$ and $C_z$

To examine the extent to which the acceptance cancels in the photon-helicity asymmetry, consider,

$$A = \frac{N^+ - N^-}{N^+ + N^-} = \frac{\frac{n^+}{\epsilon^+} - \frac{n^-}{\epsilon^-}}{\frac{n^+}{\epsilon^+} + \frac{n^-}{\epsilon^-}} \tag{3.44}$$

If $\epsilon^+ \neq \epsilon^-$, acceptance does not cancel in the asymmetry. Let the phase-space distribution of $K_1^+, K_2^+, \pi^-$ be represented by the random variables $Y_1, Y_2, X$ respectively. We assume the total acceptance for detecting the final state $K^+K^+\pi^-$ can be written as the product of the acceptance associated with each final state particle.

$$\epsilon = C\epsilon(Y_1)\epsilon(Y_2)\epsilon(X), \tag{3.45}$$

where $C$ is an overall factor representing all other acceptance effects that are not helicity dependent. Strictly speaking, the incoming photon's helicity does not change the form of each acceptance function, it rather changes the underlying distributions $Y_1, Y_2$ and $X$. Let the distributions associated with positive and negative helicity be $Y_1^\pm, Y_2^\pm, X^\pm$. The total acceptance for positive and negative photon helicity ($\epsilon^\pm$) is given by

$$\epsilon^\pm = C\epsilon(Y_1^\pm)\epsilon(Y_2^\pm)\epsilon(X^\pm) \tag{3.46}$$

Consider that all dominant underlying mechanisms in the $\gamma p \to K^+K^+\Xi^-$ reaction has the kaons coming from parity-conserving strong or electromagnetic processes. It follows that all the kinematic distributions for both kaons are independent of the photon-beam helicity. The only helicity dependent parts of the reaction are those

following a weak decay, which strictly is limited to the decay of ground-state hyperons. The two ground state hyperon decays in the reaction are $\Xi^- \to \Lambda\pi^-$ and $\Lambda \to p\pi^-$. Only the $\Xi^-$ decay contributes to the acceptance, since the signal is mostly free of background from the $\Lambda$ decay. Furthermore the acceptance can only be dependent on the projection of the $\pi^-$ angular distribution on the $\hat{x}$- and $\hat{z}$- axis since the polarization cannot be transfered to the $\Xi^-$ in the y-axis direction. Thus,

$$\epsilon^{\pm} = C\epsilon(X^{\pm}), \tag{3.47}$$

where the non-helicity-dependent factors of the acceptance have been absorbed in $C$. Expanding $X^{\pm}$,

$$X^{\pm} = \{x^{\pm}, y, z^{\pm}\}, \tag{3.48}$$

where $x, y, z$ respectively represent the polar angle distribution of the pion off $\hat{x}-, \hat{y}-$ and $\hat{z}$ for positive (negative) photon helicity states. Finally the acceptance takes on the form,

$$\epsilon^{\pm} = C\epsilon(x^{\pm})\epsilon(z^{\pm}). \tag{3.49}$$

Out of the two terms above, one, which we shall call the *finite binning effect*, should be (shown in Chapter 7) considerably smaller than the other. The finite binning term is $\epsilon(x^{\pm})$ when binning the asymmetry in $\cos\theta_{\pi}^{x}$ (for the calculation of $C_x$) and $\epsilon(z^{\pm})$ when binning in $\cos\theta_{\pi}^{z}$ (for the calculation of $C_z$). The insignificance of the finite binning effect can be understood by considering that the distribution surrounding a point in $\cos\theta_{p}^{x}$ or $\cos\theta_{p}^{z}$, is limited by the bin width. The distribution, call it $x_i$, approaches invariance under helicity flipping $x_i^{+} = x_i^{-}$ as the bin width becomes arbitrarily fine. Of course the bin width must be finite and as a result there will be a an effect, albeit a small one. The systematic uncertainty from the two leading-order, effects were estimated by simulating events as discussed in Chapter 7.

## 3.7 Frame Transformation Effect on Hyperon Polarization

Because of the precession of spin under Lorentz transformations, baryon spin projections may possess differing values in different reference frames. The current analysis measures the cascade spin projections in it's rest frame, here we will show that such measurements remain invariant under a Lorentz-boost to the center-of-momentum-frame. The mentioned effect, commonly referred to as Wigner-Thomas precession, comes about from the non-commutativity of boosts and rotations.

Here we adopt an argument similar to one presented in Ref. [15]. Consider a particle p in a frame S with velocity $\vec{\beta}$ and polar angle $\theta$ with respect to a boost to a frame $\tilde{S}$. The velocity and polar angle of p as viewed from $\tilde{S}$ with respect to the boost direction is denoted $\tilde{\vec{\beta}}$ and $\tilde{\theta}$. Additionally, let the corresponding Lorentz factor for the particle in S and $\tilde{S}$ be $\gamma$ and $\tilde{\gamma}$, respectively, while letting the Lorentz factor for the boost from $S$ to $\tilde{S}$ be denoted by $\Gamma$. The Wigner-Thomas precession angle $\alpha_W$ about the $y$-axis for an arbitrary boost within the $x, z$ plane has been shown to be,

$$\sin\alpha_W = \frac{1+\Gamma}{\gamma+\tilde{\gamma}}\sin(\theta-\tilde{\theta}) \tag{3.50}$$

[15, 41, 42]. For this analysis, the boost from the hyperon rest-frame $\tilde{S}$ to the lab-frame S is by definition, in the direction of the hyperon momentum, meaning zero polar angle between the frame boost and and the particle momentum (hence $\tilde{\theta} = \theta = 0$ ). It follows that spin precession angle, $\alpha_W$, is zero meaning that the hyperon polarization is left unchanged when boosting from the hyperon rest-frame to the center-of-momentum-frame [15, 16].

# Chapter 4

## Data Processing and Event Selection

This chapter details the method of extracting the $\Xi^- \to \Lambda\pi^-$ events from the 121 Terra bites of raw data. We derived various algorithms intended to maximize our sample, whilst minimizing background contamination from other reactions. As a consequence of the low cross sections for cascade production, the vast majority of physics events composing the g12 dataset are extraneous to our analysis. Out of the some 26 billion reconstructed events, only 5143 survived the final selection criteria. Additionally, we derived important corrections and calibrations that were applied to the data, which are discussed in Section 4.3.

## 4.1 Physics Event Selection

### 4.1.1 Topology Requirement

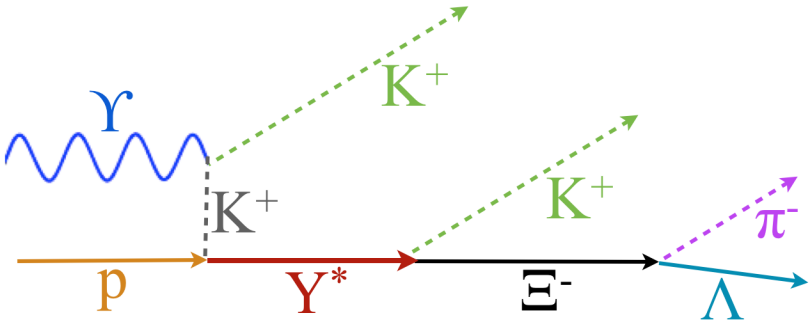


Figure 4.1: Cartoon representing $\Xi^-$ photoproduction via virtual-meson exchange in the $t$-channel and its weak decay.

Figure 4.1 shows a toy model of our reaction. Events with all three mesons, $K^+K^+\pi^-$, were required in the final state. Specifically, the topology requirements implemented were,

- Number of $K^+ = 2$,

- Number of $\pi^- = 1$,
- Number of $p = 0$ or 1,
- Number of $K^- = 0$,
- Number of $\pi^+ = 0$.

The number of protons was permitted to float since a large amount of data were expected to contain them due to the $\Lambda \rightarrow \pi^- p$ decay. Our dominant source of background comes from pions masquerading as kaons in the particle identification logic. Meson misidentification is further discussed in latter sections of the chapter. As will be shown, events with the decay $\Xi^- \rightarrow \pi^- \Lambda$ can be selected from the data by imposing kinematic requirements on the detected mesons.

### 4.1.2 Missing Mass Selection in the Hypersphere

In our topology there are four useful kinematic constraints that comprise two *missing mass*[1] and two *invariant mass* requirements. Rather than cutting on all four quantities individually, they are taken together in a single cut as orthogonal displacements within a hypersphere. All four kinematic quantities are divided by their associated detected widths ($3\sigma$) and taken as coordinates in the 4d space. The four kinematic constraints for our reaction are evident in the diagram in Fig. 4.1. The cuts are given separately as,

1. Require the missing mass of the $(\gamma + p) - (K^+ + K^+)$ system be the known mass of the $\Xi^-$.

[1]Missing mass is the conventional name attributed to invariant mass of an initial state minus a final state.

2. Require the missing mass of the $(\gamma + p) - (K^+ + K^+ + \pi^-)$ be equal to the known mass of the $\Lambda$

3. Require the invariant mass of the $\pi^- + \Lambda$ system be equal to the known mass of $\Xi^-$

4. Require the effective mass of the $\pi^- - \Xi^-$ system be equal to the known mass of $\Xi^-$

The amount by which the constraints were allowed to float was determined by the resolution of CLAS. The resolution of all four quantities were measured by fitting each corresponding distribution to a Gaussian function. Each fit and their associated widths are displayed in Fig. 4.2.

For typographical ease, a short hand notation for the missing mass, $MM(K^+ + K^+)$ and $MM(K^+ + K^+\pi^-)$ will be used. Similarly, $M(\pi^- + \Lambda)$ and $M(\pi^- - \Xi^-)$ denote the relevant invariant and effective mass quantities. The "hypersphere" has coordinates defined as,

$$x_1 = (MM(K^+ + K^+) - \Xi^-_{mass})/(3\sigma_1), \tag{4.1}$$

$$x_2 = (MM(K^+ + K^+ + \pi^-) - \Lambda_{mass})/(3\sigma_2), \tag{4.2}$$

$$x_3 = (M(\Lambda + \pi^-) - \Xi^-_{mass})/(3\sigma_3), \tag{4.3}$$

$$x_4 = (M(\Xi^- - \pi^-) - \Lambda_{mass})/(3\sigma_4), \tag{4.4}$$

$$r = \sqrt{x_1^2 + x_2^2 + x_3^2 + x_4^2}, \tag{4.5}$$

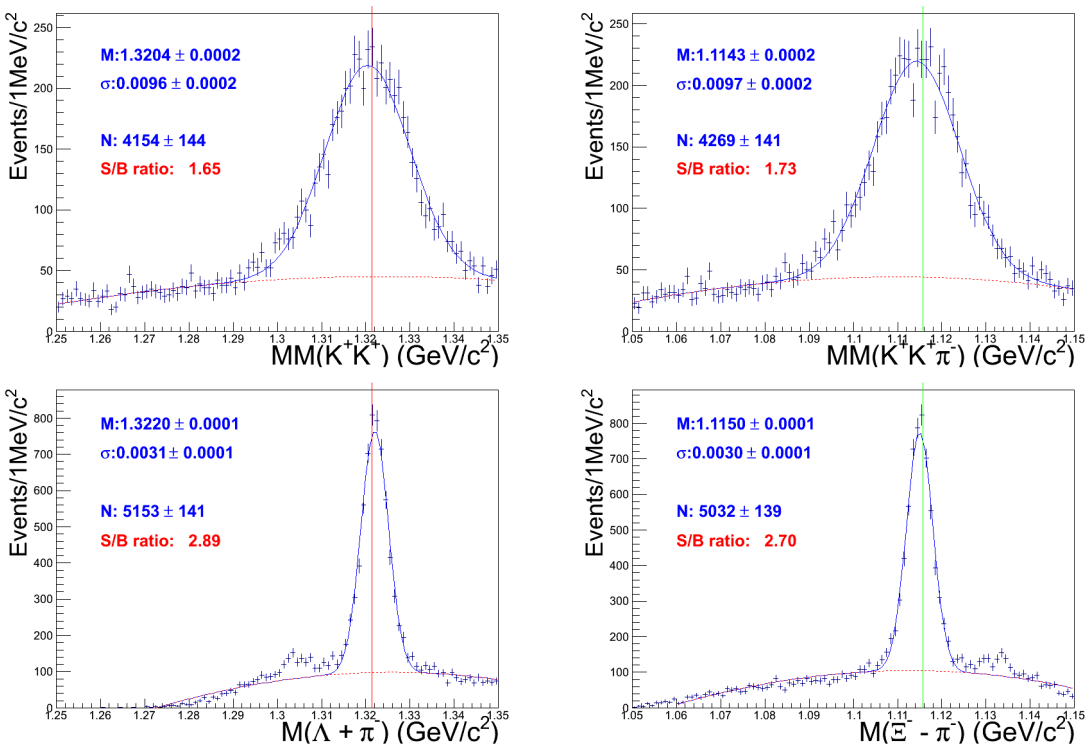


Figure 4.2: Top left: the missing mass spectrum of the $K^+K^+$ system, showing the $\Xi^-$ peak at 1.32 GeV. Top right: the missing mass spectrum of the $K^+K^+\pi^-$ system, showing the $\Lambda$ peak at 1.11 GeV. Bottom left: invariant mass spectrum of the $\Lambda\pi^-$ system, showing the $\Xi^-$ peak at 1.32 GeV. Bottom right: invariant mass spectrum of the $\Xi^- - \pi^-$ system, showing the $\Lambda$ peak at 1.11 GeV. In all plots a Gaussian is fit to the signal over a polynomial background. The vertical lines represents the known lambda or charged cascade masses. The parameter $\sigma$ of the Gaussian fit gives CLAS's "natural" resolution for its associated quantity.

where $\sigma_n$ denotes the Gaussian width of the associated quantity as measured in Fig. 4.2. Loosely speaking, a cut on the hypersphere radius $r$ represents a cut on "sigma"; a "three sigma" cuts equates taking events within the hypervolume defined by $r < 1$. Fig. 4.3 shows the mass spectra after various cuts on the hypersphere radius. The sample used in our analysis is the result of a $r < 1$ cut (shown in blue). Overlaying the signal in Fig. 4.3, are two sidebands taken from the two equal-hypervolume outer layers, $1 < r < \sqrt[4]{2}$ and $\sqrt[4]{2} < r < \sqrt[4]{3}$. A nearly background-free sample of $\Xi \to \pi^- \Lambda$ events is evident.

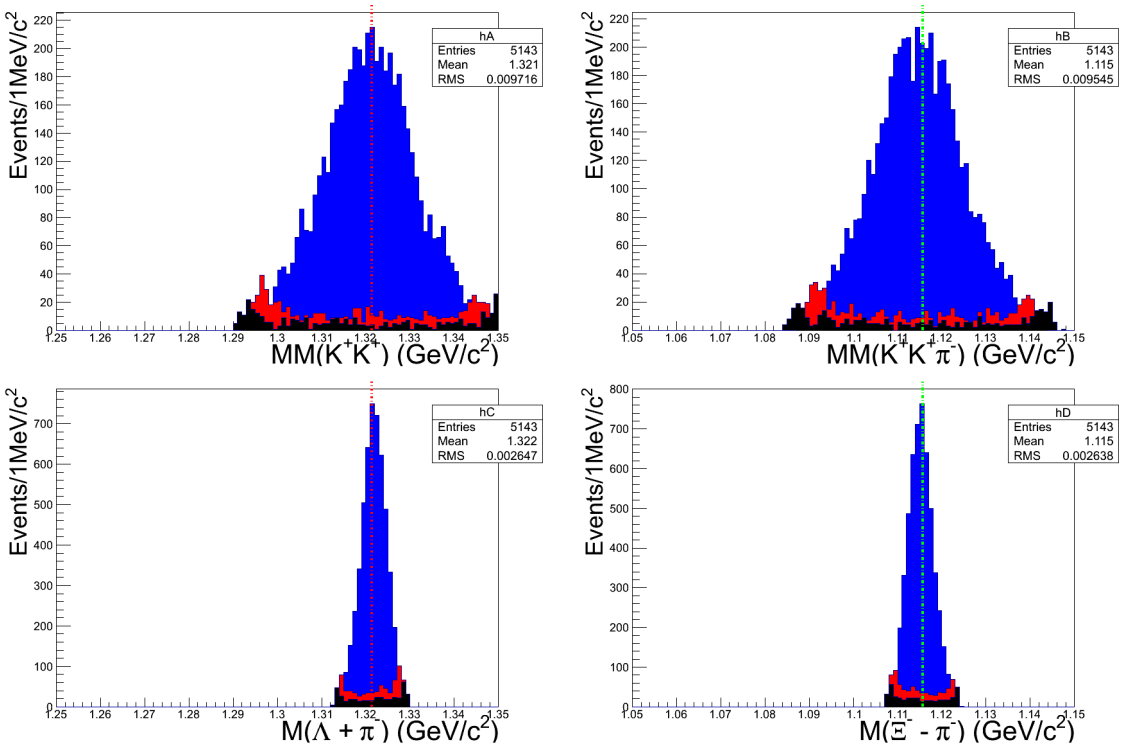


Figure 4.3: The nominal mass cut $r < 1$ represents a three sigma cut as shown in blue. The first sideband (in red) are the events lying in the hyper-shell $1 < r < \sqrt[4]{2}$ while the second sideband (black) lie in the region $\sqrt[4]{2} < r < \sqrt[4]{3}$.

### 4.1.3 Vertex Position Selection

[h] The event vertex time is taken as the average over all final state particles, required to lie within or near the physical region of the hydrogen target. Our vertex selection occupied a cylindrical volume from -120 to -60 cm along the beam, with a radius of 7 cm centered about zero. It is possible to have event vertices outside the target region due to the long decay time of the cascade, and the resultant detachment of the pion vertex. Figure 4.4 shows the vertex distribution for the $K^+K^+\pi^-(\Lambda)$ events used in our analysis.

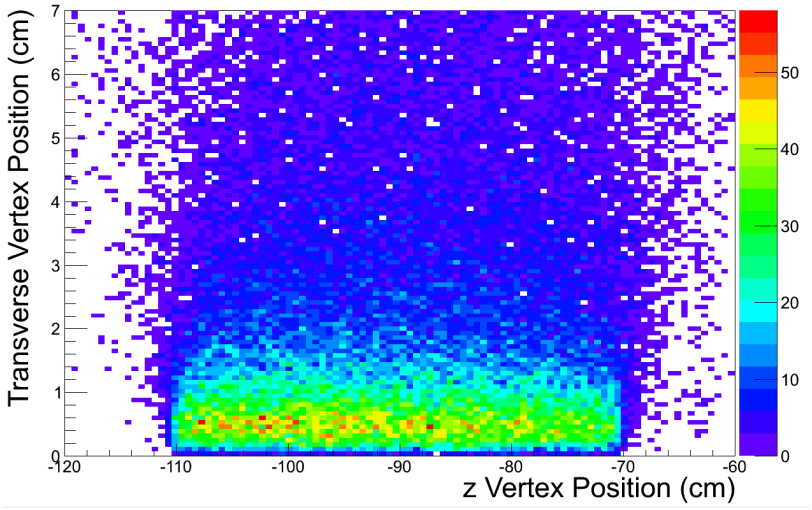


Figure 4.4: The cut region of spacial vertex distribution. All events lying outside the plot were excluded.

### 4.1.4 Vertex Timing Selection

The CEBAF Radio-Frequency signal (RF) responsible for the acceleration of electrons delivered to Hall B provides a precise ($\approx$ 15 ps) means of correcting the tagger time once the beam bucket is identified. The vertex time can also be calculated as follows: take the time readout for a particle hit in a region of the detector and subtract the

travel time. The calculation requires a knowledge of the particle speed, $\beta$. For each track $\beta$ is calculated as,

$$\beta_{ST_{TOF}} = \frac{l_{TOF} - l_{ST}}{c(t_{TOF} - t_{ST})}, \tag{4.6}$$

$$\beta_{vtx_{TOF}} = \frac{l_{TOF}}{c(t_{TOF} - t_{vtx}(TAG_{RF})}, \tag{4.7}$$

where

- $l_{TOF}$ and $l_{ST}$ are the path lengths from the vertex ot the time of flight counter and start counter respectively,
- $T_{TOF}$ and $T_{ST}$ are the hit times in the time of flight counter and start counter respectively,
- $t_{vtx}(TAG_{RF})$ is the RF-corrected vertex time.

Agreement of one nanosecond between the event-vertex time as calculated by the RF-corrected tagger and the start counter was required. The difference between both methods of calculation are shown in Fig. 4.5. Similarly, the difference between the RF-corrected tagger event-time and particle-vertex-time as calculated by the TOF for both kaons is shown in Fig. 4.6.

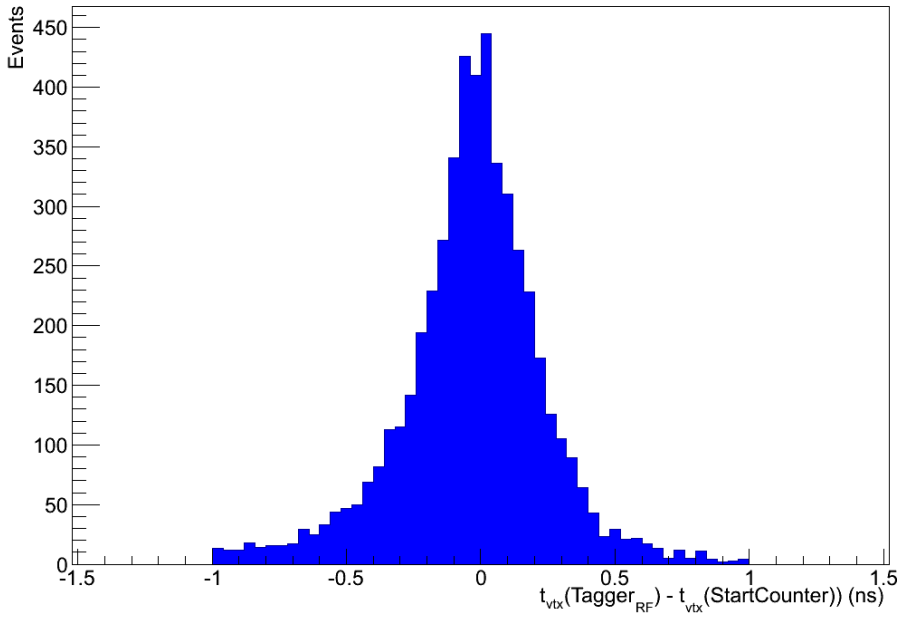


Figure 4.5: Difference between event-vertex time as calculated by the RF-corrected tagger and start counter, for events passing all cuts. A one nanosecond cut was imposed.

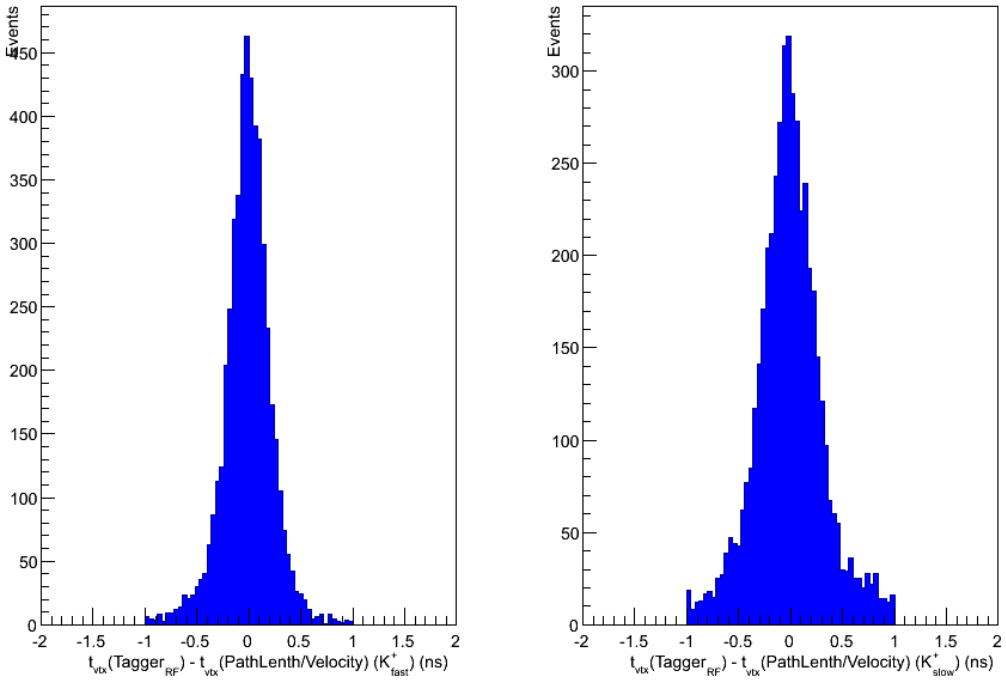


Figure 4.6: Difference between vertex-time and particle-vertex time as calculated by the RF-corrected tagger and TOF, for events passing all cuts. A one nanosecond cut was imposed. Left: fast kaon. Right: slow kaon.

### 4.1.5 Eliminating Particle Misidentification

As mentioned in Section 4.1.1, for CLAS, a dominant source of background in kaon analyses are pions misidentified as kaons. It turns out however, that our kinematic hypersphere cuts eliminate the pion background, as can be seen in Fig. 4.7 and 4.8.

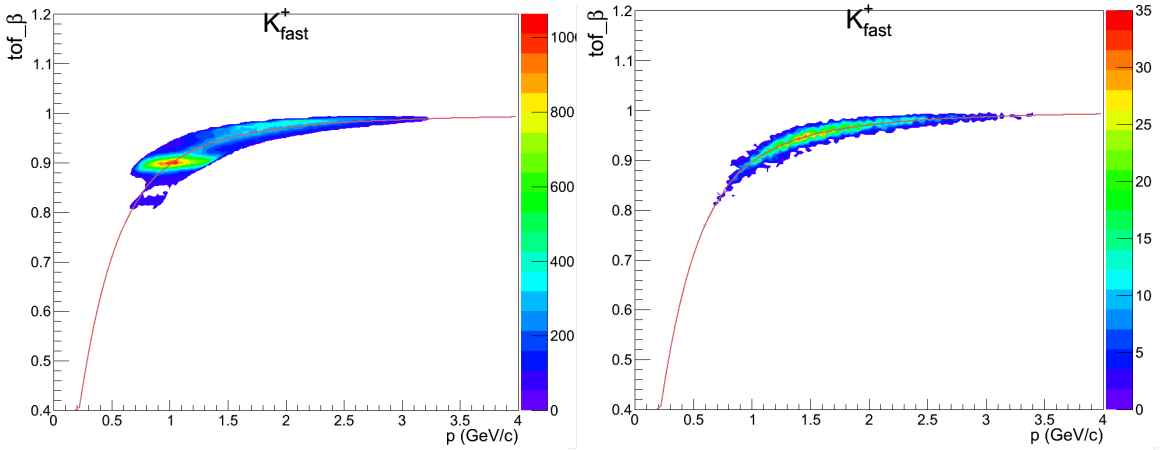


Figure 4.7: $\beta$ vs momentum for the fast kaon overlaid with it's theoretical curve. Left: before hypersphere cuts, an extra band is visible comprising misidentified pions. Right: after hypersphere cuts, the contamination is eliminated.

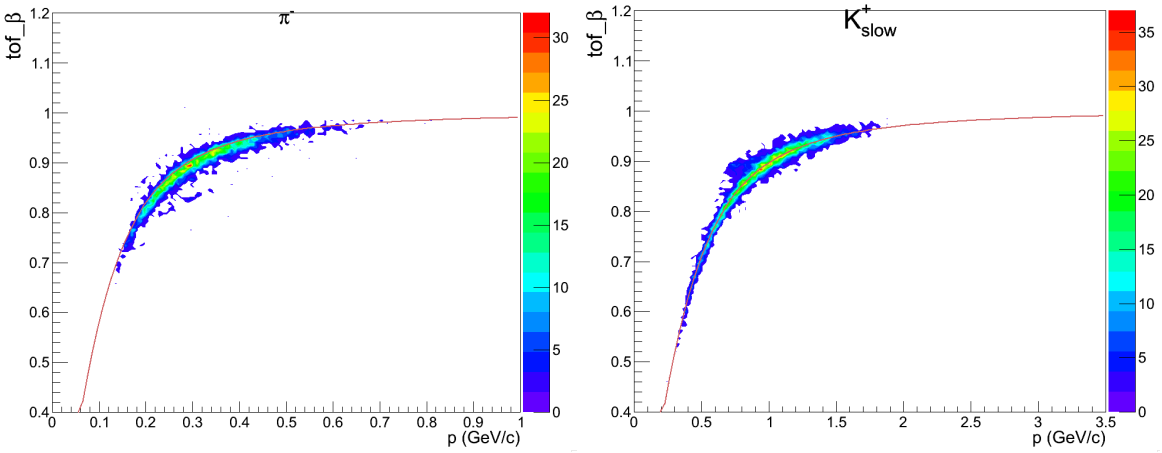


Figure 4.8: $\beta$ vs momentum for the pion (left) and slow kaon (right) overlaid with their respective theoretical curves. Both plots show the data after hypersphere cuts and indicate no contamination due to misidentification or timing inaccuracies

### 4.1.6 The Fiducial Region

The fiducial regions of the detector are those found to be *trustworthy*, as the name suggests. We derived *Geometric fiducial cuts* for the g12 data, which are cuts based on the exclusion of events laying outside regions where acceptance is well behaved and reliably reproduced in simulation. Such regions for all g12 data are expressed as an upper and lower limit of the difference in azimuthal angle between the center of a given sector, and a particle track. Because of the hyperbolic geometry of CLAS and the presence of the toroidal magnetic field, the fiducial boundaries on the angle $\phi$ are functions of momentum ($p$), charge, and polar angle ($\theta$) of each track. The boundaries were evaluated separately in each sector, nominally defined as the $\phi$ values in which occupancy drops below 50% of that in the respective sector's "flat" region. The flat regions were defined as $-10^\circ < \phi < 10^\circ$. The nominal upper and lower $\phi$ limits depend strongly on particle charge, $p$ and $\theta$, hence the need for functional characterization and extrapolation.

In order to determine the fiducial limits for charged hadrons, a sample of exclusive $\gamma p \to p\pi^+\pi^-$ events were sliced into 5x15x6 bins in $p$, $\theta$, and sector respectively. The $\phi$ distributions for $\pi^+$ and $\pi^-$ were plotted separately in each bin. The upper and lower $\phi$ limits of these *first-generation* plots were found according to the nominal fiducial definition of 50% occupancy as illustrated in Fig. 4.9. The results from the first-generation fits were represented in *second-generation* plots of $\phi_{min}$ and $\phi_{max}$ vs $\theta$ as also shown in Fig. 4.9. The data in the second-generation plots were fit with hyperbolas, chosen since they replicate the projection of the detector. Second-generation fitting parameters were then plotted vs $p$ in *third-generation* plots. These third generation plots were fit to power functions as shown in Fig. 4.10. Results of the third-generation fits define the sought after functional form $\phi_{min}(\theta, p)$ and $\phi_{max}(\theta, p)$

for each sector. The sector integrated results for positive and negative hadron tracks compose the nominal fiducial region. *Tight cuts* and *loose cuts* were defined as a contraction and expansion respectively, by 4° from the nominal fiducial cuts. The cuts are shown on the $p\pi^+\pi^-$ and $K^+K^-\pi^-$ data in Figs. 4.11-4.17. The effect of the fiducial cuts on the measured spin-observables are left for discussion in Chapter 7 of this dissertation.

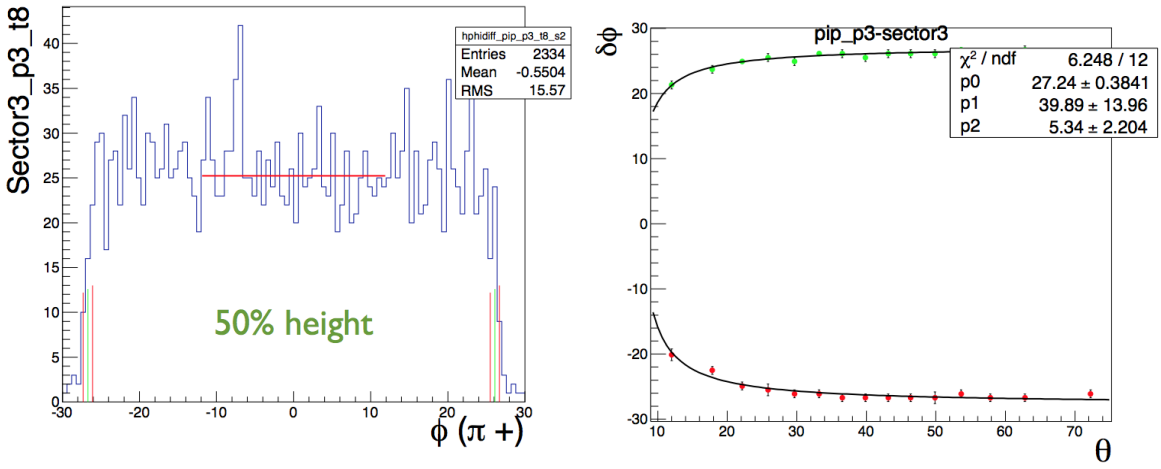


Figure 4.9: Left: shows the $\pi^+$ $\phi$ distribution for sector-three in one $p$ and $\theta$ bin along with the upper and lower limits of the fiducial region represented by the green vertical line. Right: a second-generation plot, fit to a hyperbola.

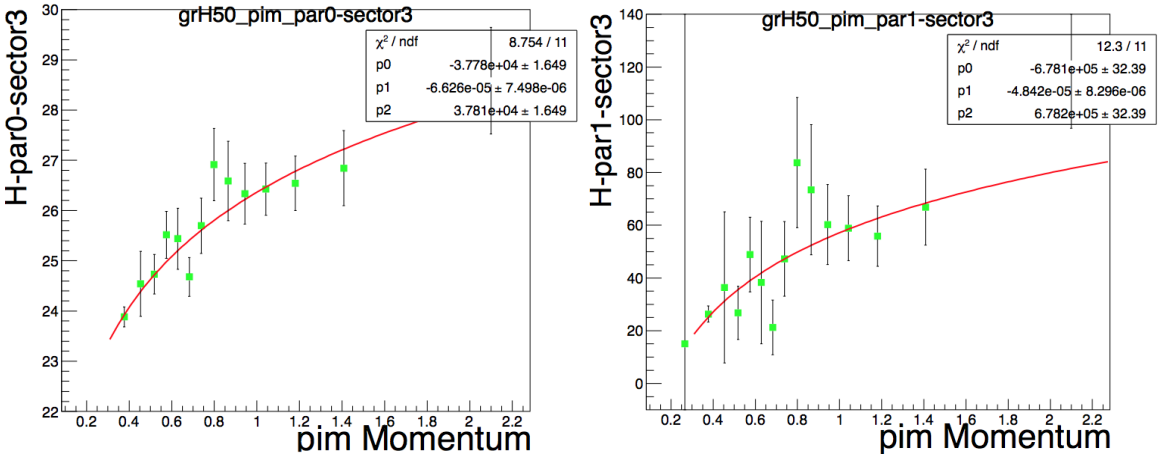


Figure 4.10: Third-generation plots of the fitting parameters from second-generation fits for sector three. The data are fit to power functions.

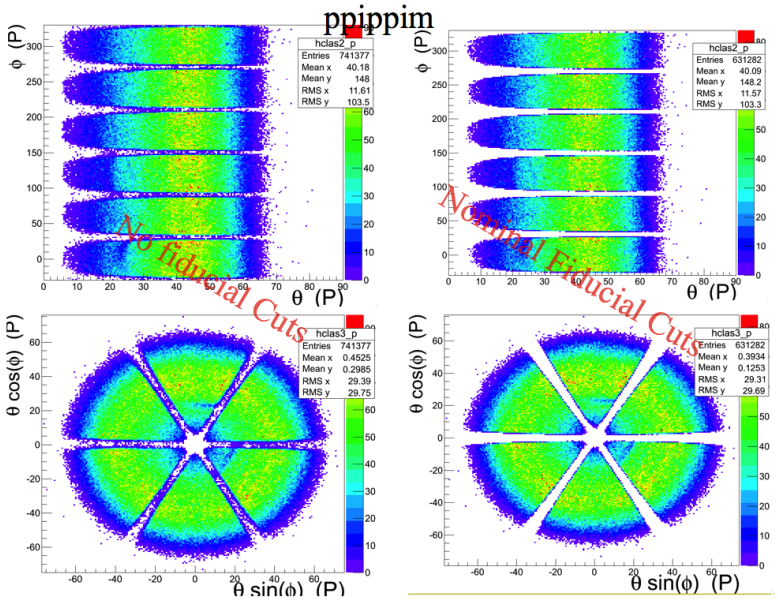


Figure 4.11: The angular distribution of the proton from exclusive $p\pi^+\pi^-$ events is shown. In the top, $\phi$ vs $\theta$ is plotted, the bottom plots conveys similar information mapped to mimic the geometry of CLAS. Left: No fiducial cuts. Right: nominal fiducial cuts on the proton.

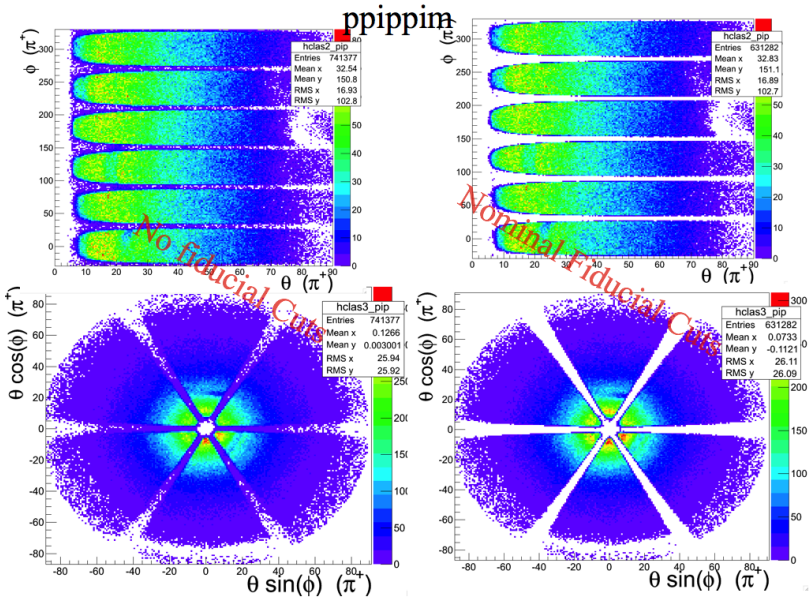


Figure 4.12: The angular distribution of the positive pion from exclusive $p\pi^+\pi^-$ events is shown. In the top, $\phi$ vs $\theta$ is plotted, the bottom plots conveys similar information mapped to reflect the geometry of CLAS. Left: no fiducial cuts. Right: nominal fiducial cuts on the positive pion.

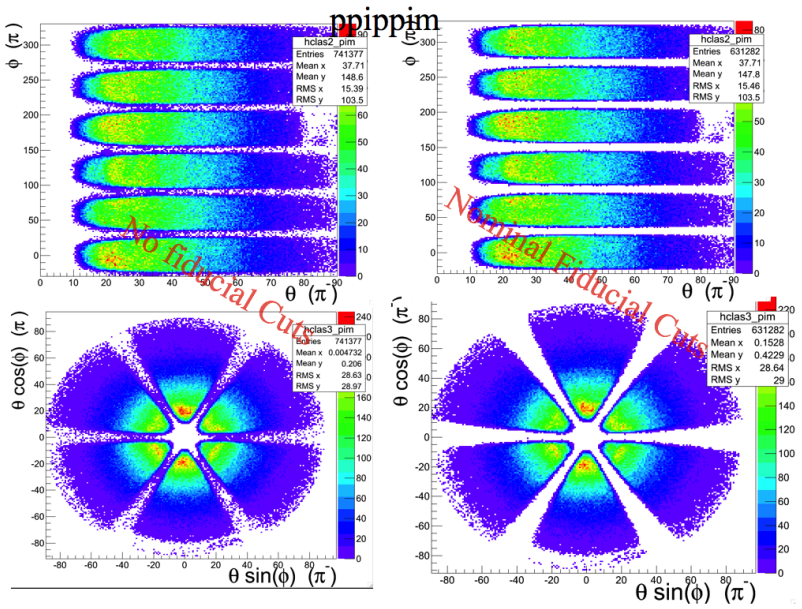


Figure 4.13: The angular distribution of the negative pion from exclusive $p\pi^+\pi^-$ events is shown. In the top, $\phi$ vs $\theta$ is plotted, the bottom plots conveys similar information mapped to reflect the geometry of CLAS. Left: no fiducial cuts. Right: nominal fiducial cuts on the negative pion.

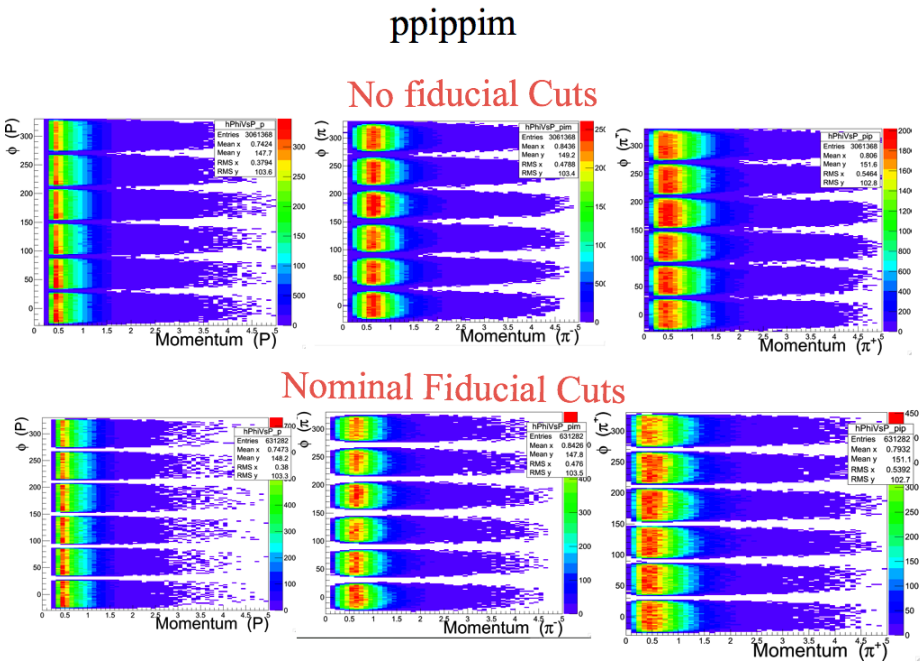


Figure 4.14: From left to right: $\phi$ vs momentum for the proton, negative pion and positive pion for $p\pi^+\pi^-$ events. Top: no fiducial cuts. Bottom: nominal fiducial cuts.

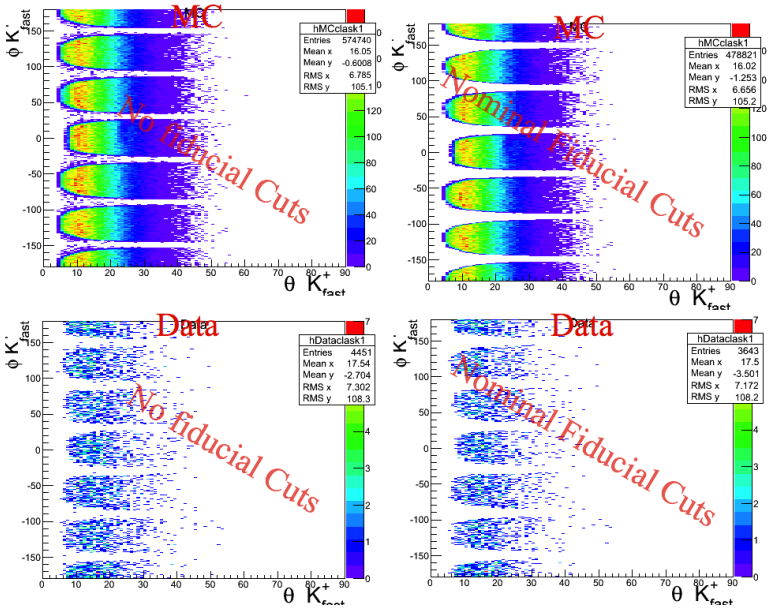


Figure 4.15: $\phi$ vs $\theta$ for the fast kaon from $K^+K^+\pi^-(\Lambda)$ events are shown. On the top, simulated Monte Carlo events are plotted, on bottom, the g12 data of our analysis. Left: No fiducial cuts. Right: nominal fiducial cuts on the fast kaon.

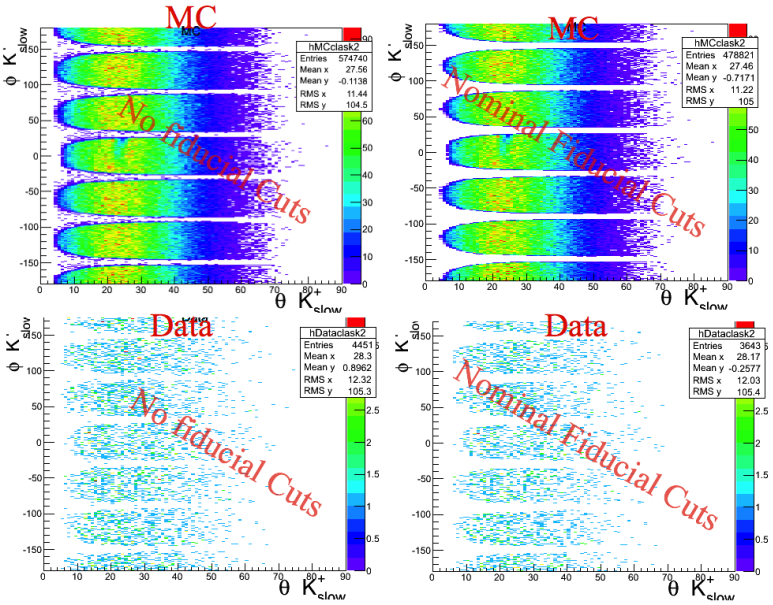


Figure 4.16: $\phi$ vs $\theta$ for the slow kaon from $K^+K^+\pi^-(\Lambda)$ events are shown. On the top, simulated Monte Carlo events are plotted, on bottom, the g12 data of our analysis. Left: No fiducial cuts. Right: nominal fiducial cuts on the slow.

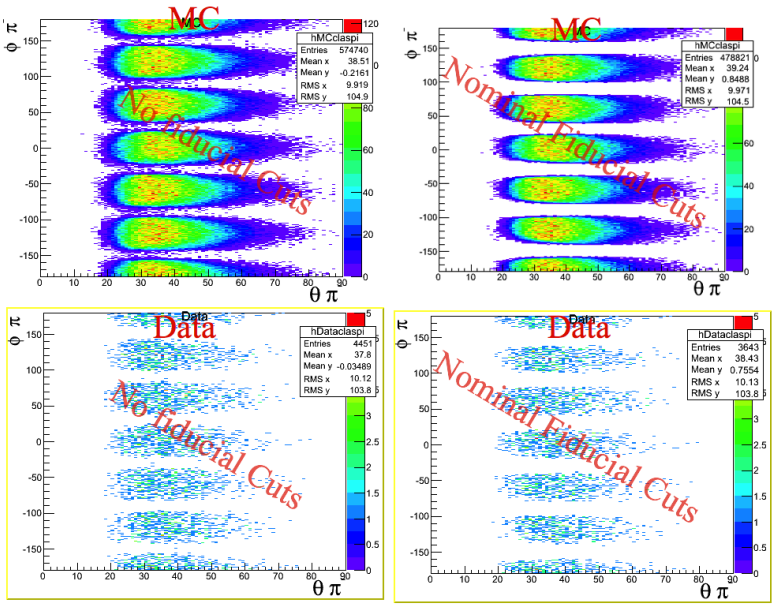


Figure 4.17: $\phi$ vs $\theta$ for the pion from $K^+K^+\pi^-(\Lambda)$ events are shown. On the top, simulated Monte Carlo events are plotted, on bottom, the g12 data of our analysis. Left: No fiducial cuts. Right: nominal fiducial cuts on the pion.

### 4.1.7 Photon-Beam Energy

The threshold center-of-momentum energy $W_{min}$ for production of the final state $K^+K^+\Xi^-$ is simply the sum of each particle's mass-energy. The threshold photon energy ($E_\gamma^{min}$) for producing $K^+K^+\Xi^-$ off a fixed proton target can be computed by considering the conservation of mass-energy.

$$m_i^2 = m_f^2 \Longrightarrow (p_\gamma + p_p)^2 = (p_{K_1^+} + p_{K_2^+} + p_{\Xi^-})^2, \tag{4.8}$$

where $m_i$ and $m_f$ represent the invariant mass of the initial and final state respectively, and $p_x$ represents the energy-momentum four-vector for particle $x$ in the reaction. Carrying out the operation on the left hand side gives,

$$p_\gamma p^\gamma + p_p p^p + p_\gamma p^p + p_p p^\gamma = (p_{K_1^+} + p_{K_2^+} + p_{\Xi^-})^2. \tag{4.9}$$

Considering the proton has zero momentum in the lab-frame and that for the lowest energy final state, $p_{K_1^+}, p_{K_2^+}$ and $p_{\Xi^-}$ will have zero momentum, one obtains,

$$m_p^2 + 2m_p E_\gamma^{min} = (m_{K_1^+} + m_{K_2^+} + m_{\Xi^+})^2. \tag{4.10}$$

Which, using the known values of the particle masses gives a value of

$$E_\gamma^{min} = \frac{(m_{K_1^+} + m_{K_2^+} + m_{\Xi^+})^2 - m_p^2}{2m_p} \approx 2.37 \text{ GeV} \tag{4.11}$$

Where the known masses used in this calculation are,

- $m_{K^+} = 0.49367$ GeV
- $m_p = 0.93827$ GeV
- $m_{\Xi^-} = 1.32171$ GeV

Although the threshold is around 2.37 GeV, events created near this energy are not detected since CLAS is inefficient at reconstructing low speed tracks and also because of low cross sections below 3 GeV [13]. The photon-energy range for cascade production in the data is 2.8-5.5 GeV.

## 4.2 Kinematic Binning of Data

For our analysis, the polarization of the cascade was measured in bins of photon-beam energy, $E_\gamma$, and center-of-momentum cascade polar angle (see Fig. 3.2), $\theta_\Xi^{cm}$. For convenience the cascade angle is expressed in terms of it's cosine, that is, $\cos\theta_\Xi^{cm}$. Various binning schemes were considered. Most of our results were measured with data separated in three bins with an equal number of events in each. Figure 4.18 shows the primary binning scheme.

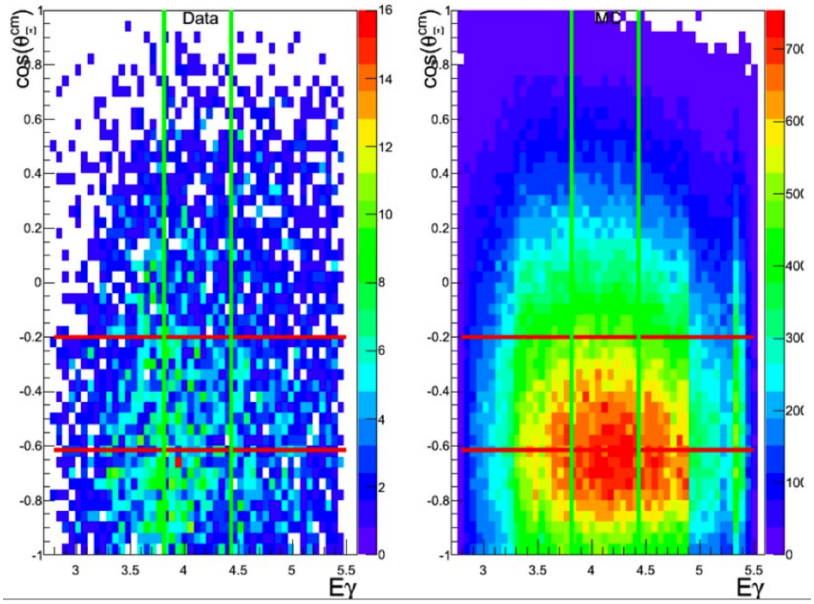


Figure 4.18: The red horizontal lines represent the binning in $\cos\theta_{\Xi}^{cm}$ while the green horizontal lines represent the binning in $E_{\gamma}$. Left: the g12 data. Right: Monte Carlo simulated events.

## 4.3 Corrections and Calibration

### 4.3.1 Photon-Beam Polarization Determination

The electron beam produced with a polarized laser incident on gallium arsenide allows for longitudinal polarization of the electrons [43] and in turn, due to the bremsstrahlung process, circular polarization of the photon beam. The accurate measurement of the polarization transfered from the photon beam to the produced hyperons ($C_x$ and $C_z$) requires knowledge of the beam polarization. Such knowledge is ascertained by knowing the magnitude of incident electron-beam polarization, and the helicity orientation of the electron beam bunch responsible for the event (in the lab-frame). The Maximon-Olsen formula relating incident electron beam polarization,

with the photon polarization is given by [44],

$$P_{\odot}(E_{\gamma}) = \frac{x(4-x)}{4-4x+3x^2} P_{elec} \tag{4.12}$$

where $x = E_{\gamma}/E_{elec}$ is the ratio of photon energy, $E_{\gamma}$, to beam energy, $E_{elec}$. The g12 experiment ran with a constant electron energy of $E_{elec} = 5.715$ GeV. The polarization of the electron beam was measured regularly using the a Møller polarimeter. The polarimeter measures electron polarization by making use of the helicity dependent nature of Møller scattering [29, 35]. The Møller measurements, summarized in Table 4.1, were performed regularly (every few days) during g12. We wrote a simple calculator for the collaboration that computes the run-integrated flux-weighted average of the photon-beam circular polarization in a user-specified energy range, the output of which is given in Table 4.2.

An important experimental aspect of g12 is that the electron-beam helicity was flipped at a rate around 30 Hz. While the helicity information was recorded and stored in the HEVT bank for each event, the convention for bit encoding has been known to change from real-time to delayed-time recording. Further considerations, such as the half-wave plate orientation also had to be accounted for.

The only sure way to pin down the absolute beam helicity orientation for our data was to analyze a well known helicity-dependent reaction. Well-established results in Ref. [45] in the beam-helicity asymmetry, $I^{\odot}(\phi_{\pi}^{hel})$, for the reaction, $\gamma p \to p\pi^+\pi^-$, were reproduced. The mentioned reaction was shown to have a specific helicity-frame defined $\phi_{\pi^+}^{hel}$-dependent structure. If the helicity convention was reversed then we would observe $I^{\odot}(\phi_{\pi^+}^{hel}) \to -I^{\odot}(\phi_{\pi^+}^{hel})$.

The sub-analysis we performed required exclusive $p\pi^+\pi^-$ events in the final state. To ensure exclusivity we required zero missing energy and momentum within detector

| Run Number | Moller Readout ($P_e$) |
|---|---|
| 56355 | (81.221 ± 1.48)% |
| 56476 | (67.166 ± 1.21)% |
| 56644 | (59.294 ± 1.47)% |
| 56733 | (62.071 ± 1.46)% |
| 56744 | (62.78 ± 1.25)% |
| 56850 | (46.490 ± 1.47)% |
| 56930 | (45.450 ± 1.45 )% |
| 57029 | (68.741 ± 1.38)% |
| 57178 | (70.504 ± 1.46 )% |
| 57250 | (75.691 ± 1.46)% |
| 57283 | (68.535 ± 1.44)% |

Table 4.1: The degree of longitudinal electron polarization ($P_e$) for each Møller run.

resolution. The helicity frame (shown in Fig. 4.19) was defined to be the rest frame of the hypothetical parent meson of the two pion system, with $\hat{z}$ aligned along its center-of-mass defined momentum. $\phi_{\pi^+}^{hel}$ is the angle between the proton-production plane, and the plane containing both pions. The beam helicity asymmetry is given by,

$$I_{\odot} = \frac{N^+ - N^-}{N^+ + N^-}, \tag{4.13}$$

where $N^{\pm}$ indicates the number of events with positive (negative) photon helicity. Figs. 4.20-4.21 show the $I_{\odot}(\phi_{\pi^+}^{hel})$ for g12 and in the analysis of [45]. The lab-frame electron helicity readout was taken from the HEVT bank (HEVT→hevt[0].TGRPRS).

| $E_\gamma$ | 3.47 GeV | 4.09 GeV | 4.88 GeV | Integrated |
|---|---|---|---|---|
| $P_\odot$ | $0.447 \pm 0.022$ | $0.539 \pm 0.027$ | $0.592 \pm 0.029$ | $0.526 \pm 0.026$ |

Table 4.2: A table showing the degree of circular photon polarization ($P_\odot$) in the relevant kinematic bins ($E_\gamma$).

The results of our $I_\odot(\phi^{hel}_{\pi^+})$ analysis and the previously published results showed a positive (negative) HEVT readout indicates positive (negative) photon helicity. The reproduction of beam-helicity asymmetry for double charged pion production also served as a way to test the accuracy of the calculated photon polarization magnitude: both results' wave amplitudes were in good agreement.

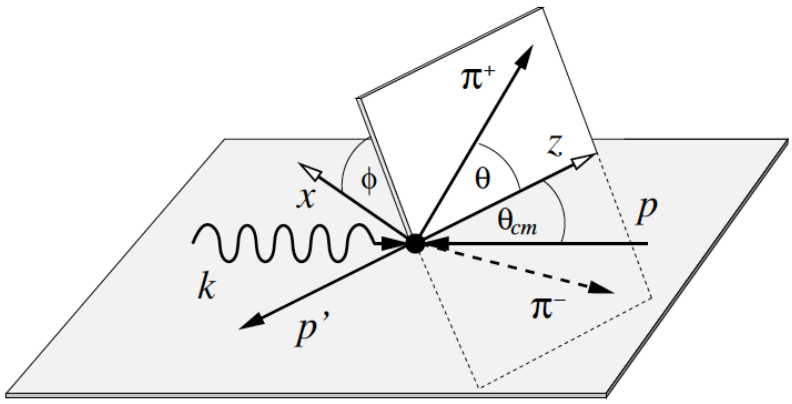


Figure 4.19: An illustration of the angle definitions used in the $\gamma p \to \pi^+\pi^- p$ sub-analysis. $\theta_{cm}$ is defined in the center-of-mass frame. $\theta$ and $\phi$ are defined in the rest frame of the $\pi^+$ $\pi^-$ system as the polar and azimuthal angles. The $z$ direction is along the total momentum of the $\pi^+\pi^-$ system. Image source [45]

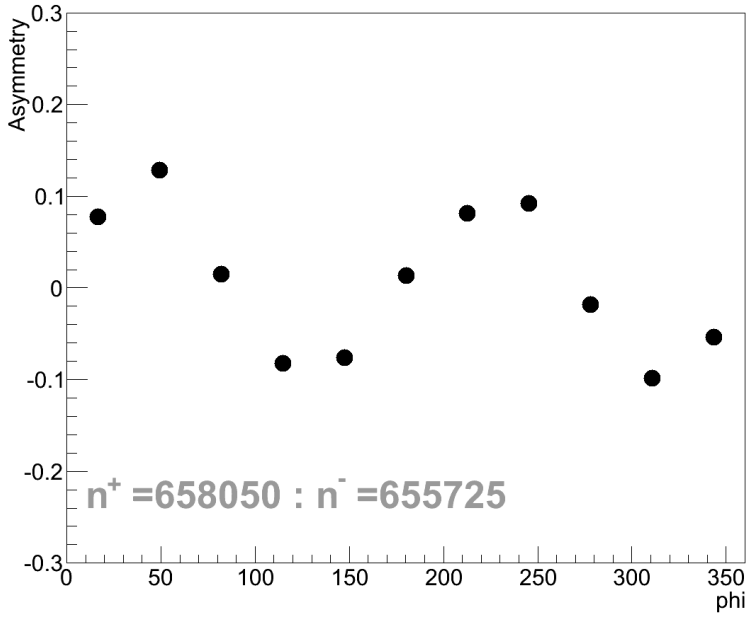


Figure 4.20: $I_{\odot}(\phi^{hel}_{\pi^+})$ for our data within the energy range of $W = 1.9 - 2.3$ GeV.

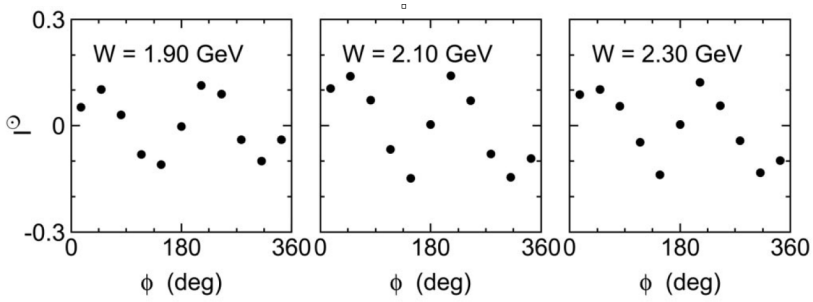


Figure 4.21: $I_{\odot}(\phi^{hel}_{\pi^+})$ as measured in the analysis [45]. The results of are shown in bins of $W$ from 1.9 to 2.3 GeV.

### 4.3.2 Multiple Photon Events

The trigger duration and limited timing resolution of the detectors results in multiple photons being read out by the tagger for each event. Multiple-photon events compose around 10% of the data; three photon selection algorithms were considered,

- Choose photon at random,
- Choose the highest energy photon,
- Reject multiplicity events.

The method contributing most constructively to the signal-to-background ratio was to choose the higher energy photon when multiplicity occurred. Photons with higher energy have a greater probability of producing cascade events although a background is introduced. The mass-hypersphere cuts however eliminate most of the background from photons which were chosen incorrectly.

### 4.3.3 CLAS Energy-Loss Corrections

The standard CLAS energy loss correction software (ELOSS) developed by Eugene Pasyuk was implemented to account for the energy dissipation experienced by particles as they pass through the material between the target and region-one drift chambers. Using the Beth-Bloch equation, the software calculates each track's energy deposition based on the measured particle track-momentum, it's path through CLAS, and a GEANT model mimicking the materials and design of CLAS. The initial energy of a non-decaying particle at the event vertex is simply,

$$E_{initial} = E_{measured} + E_{loss}. \tag{4.14}$$

Above, $E_{initial}$ is the track energy at the event vertex, $E_{measured}$ is the track energy, and $E_{loss}$ is the dissipated energy of the track [46].

### 4.3.4 Photon Beam Energy Corrections for g12

Inaccuracies in the photon energy as measured by the tagger arise due to geometric distortions in the taggers's focal plane. These distortions cause a shift in the recoil electrons' measured locations, resulting in an incorrect energy readout. The effect was studied for each event by a comparison of the measured photon energy and the energy required for the inclusive $\gamma p \rightarrow p\pi^+\pi^-$ reaction. A systematic correction (ECOR) was derived by Mike Kunkel and Johann Gotez for the g12 dataset and was implemented in the present analysis. The effect that ECOR had on our sample is discussed later in this chapter [33].

### 4.3.5 Final-State Momentum Corrections for g12

Distortions in the toroidal magnetic field and small spatial misalignments of the drift chamber during data collection result in a systematic shift in the measured particle track momenta. In order to correct for the shift in momentum, we implemented a set of corrections (PCOR) that were derived by Johann Goetz through analysis of $p\pi^+\pi^-$ events. Further details on the momentum corrections can be found in [33].

### 4.3.6 Combined Effects of Corrections

Fig. 4.22 shows the combined effect of ELOSS, photon energy, and momentum corrections on the cascade signal in our data. An increase signal quality is evident from the 10% narrowing of the mass peak.

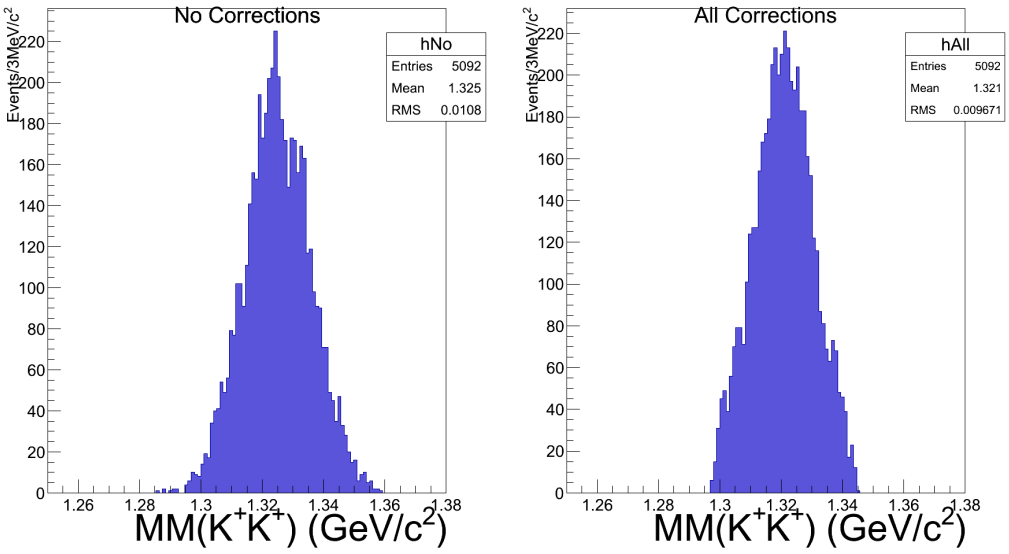


Figure 4.22: On the left, the $\Xi^-$ signal in the missing mass spectrum (after all cuts) of $K^+K^+$ before ELOSS, photon energy, and momentum corrections is shown. On the right, the same signal using the corrected four-vectors. The mass of the $\Xi^-$ is around 1.321 GeV.

# Chapter 5

# Simulation

Generally speaking, the measurement of a physical observable is sensitive to the apparatus with which the measurement is performed. In the present analysis, the polarization observables are accessed through an angular distribution. While the underlying distributions themselves are highly sensitive to the detector's acceptance, such effects, to first order, cancel in all but one of our measurement techniques. Discussions on the cancellation of acceptance can be found in Chapters 3 and 7. Simulated events were used for the calculation of acceptance corrections, estimation of certain sources of systematic uncertainty, and for cross checks of our results. The simulation used in the present analysis is shown to match to the data. Details of the simulation process, tuning, and characterization of acceptance effects are outlined in this chapter.

## 5.1 Simulation Overview

For CLAS, the acceptance is a function that describes the likelihood of detecting and reconstructing an event. The acceptance for a given particle depends mostly on its momentum, charge and scattering angle. Characterization of the detector's response for an event is a formidable challenge. A class of techniques commonly used in the physical sciences know as *Monte Carlo methods* are required. Such methods are utilized for problems with a high degree of complexity as a means to bypass the need to obtain closed-form solutions or deterministic algorithms.

The Monte Carlo methods are computational algorithms that obtain numerical results by employing repeated sampling of a random number generated according to a weighting distribution. In order to characterize the $\gamma p \to K^+K^+\Xi^- \to K^+K^+\pi^-(\Lambda) \to$

$K^+K^+\pi^-(p\pi^-)$ reaction-chain, and associated response of CLAS, pseudo-randomly generated four-vectors corresponding to the appropriate particle masses were obtained. A $t$-channel model was implicit in the probabilistic weighting factors of the four-vector generator. Our generated sample of events were then run through a computational model of CLAS. The ratio of events that survive the simulated reconstruction process to the number generated, is the acceptance. Finley tuning the underlying probability distribution for the random four-vector generation to match the physics data is a challenge in itself. In general, tuning must be performed iteratively.

The CLAS software `GENR8` was used to generate the $t$-channel phase space events. The production model of simulation is shown in Fig. 5.1. After generation, the events were run through a program `gamp2part`, which we modified so that its functionality included the ability to mimic the detachment of the $\pi^-$ vertex from the event vertex. After the generated event's vertex-positions were modified, they were sequentially run through the standard CLAS processing software, `gsim` [47], which simulates the physical effects of the detector, `gpp` which smears the simulated signals, and `a1c` for reconstruction.

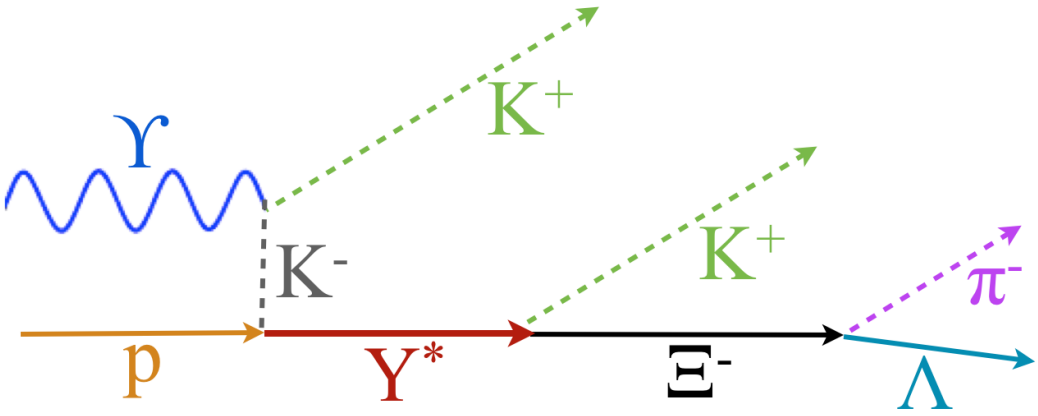


Figure 5.1: A cartoon representing our simulated cascade production model. $K^+_{fast}Y^*$ is produced via virtual-meson exchange in the $t$-channel. The $Y^*$ decays to $K^+_{slow}\Xi^-$. The cascade undergoes a subsequent decay to $\pi^-\Lambda$. The decay of $\Lambda$ to $p\pi^-$ was additionally simulated.

### 5.1.1 Generated and Reconstructed Events

GENR8 was used to produce a simulation of the $\gamma p \to K^+K^+\Xi^- \to K^+K^+\pi^-(\Lambda) \to K^+K^+\pi^-(p\pi^-)$ reaction. The angular distribution of the final state particles were controlled by mimicking the $t$-channel mode of production using $t$-slope as an input parameter. The simulated events produced by GENR8 before being processed are referred to as *generated events*. The generated events are then passed through further processing and similar event selection criteria as the data. Surviving events constitute what are referred to as the *reconstructed events*.

### 5.1.2 Detached Vertices

The detached vertex of the pion is a consideration that affects acceptance and had to be accounted for. Since GENR8 is not equipped for this functionality it was achieved by modifying the preexisting code of gamp2part. The $\pi^-$ in this analysis comes from the decay of $\Xi^-$, hence, each event's $\Xi^-$ velocity along with mean lifetime ($\tau_{\Xi^-} = 0.1639 \pm 0.0015$ [3]) can be used to calculate the average $\pi^-$ vertex detachment from the reaction vertex. The $\Xi^-$ vertex is only negligibly distant from the event vertex following from the fact that excited baryons decay strongly.

For the calculation of vertex detachment, random numbers were generated with an exponential probability distribution representing the $\Xi^-$ lifetime in its rest frame, which is a known parameter:

$$f(t) = f^{rest}(t) = \alpha e^{-\alpha t} \tag{5.1}$$

where the decay constant $\alpha$ is related to the mean lifetime $\tau$ by

$$\tau = 1/\alpha. \tag{5.2}$$

$f(t)$ was calculated starting from a pseudo random number generator with a uniform probability distribution $p(x) \in [0, 1]$ given by,

$$p(x)dx = \begin{cases} dx & : 0 < x < 1 \\ 0 & : otherwise \end{cases} \tag{5.3}$$

The fundamental transformation law of probabilities can be invoked to determine the desired form. This law is stated as,

$$|f(t)dt| = |p(x)dx| \tag{5.4}$$

or,

$$f(t) = p(x)|\frac{dx}{dt}|, \tag{5.5}$$

which enables one to relate the random variable $x$ with the random variable $t$. Since $p(x)$ is a constant we have,

$$f(t) = \frac{dx}{dt}. \tag{5.6}$$

$x$ can be solved for by taking the definite integral,

$$x = \int_0^t f(z)\, dz. \tag{5.7}$$

Above is the relationship between the source random variable and the known target random variable. In order to evaluate the probability distribution of the source

random variable, the above relationship must be inverted. Time, $t$, is of the form,

$$t = G(x) \tag{5.8}$$

and using the form of $f(t)$ we get,

$$x = \int_0^t \alpha e^{-\alpha z}\, dz, \tag{5.9}$$

or,

$$x = \alpha(\frac{1}{-\alpha}e^{-\alpha t} + \frac{1}{\alpha}) = 1 - e^{-\alpha t}. \tag{5.10}$$

Inverting the above equation,

$$t = G(x) = \frac{ln(1-x)}{-\alpha}. \tag{5.11}$$

Finally yielding,

$$t = -\tau ln(1-x). \tag{5.12}$$

The random number $t$ represents the $\Xi^-$ lifetime at rest. The lab-frame and rest-frame lifetimes are related by time dilation,

$$t = t^{rest} = \frac{t^{lab}}{\gamma}, \tag{5.13}$$

where the Lorentz factor ($\gamma$) is given by,

$$\gamma = \frac{1}{\sqrt{1 - v^2/c^2}} = \frac{1}{\sqrt{1-\beta^2}}. \tag{5.14}$$

Above, $c$ is the speed of light. The relative velocity between inertial reference frames ($v$) is simply the measured $\Xi^-$ velocity, which can be found through its momentum

by virtue of the final state kaons.

$$\beta = \frac{v}{c} = \frac{p}{\sqrt{p^2 + m^2c^2}}. \tag{5.15}$$

In natural units the Lorentz factor is

$$\gamma = \frac{1}{\sqrt{1 - \frac{p^2}{p^2+m^2}}}, \tag{5.16}$$

so,

$$t^{lab} = \frac{t^{rest}}{\sqrt{1 - \frac{p^2}{p^2+m^2}}}. \tag{5.17}$$

Hence the $\Xi^-$ flies a distance between its creation and decay given by,

$$d = vt^{lab} = c\beta t^{lab} = \frac{c\gamma p t^{rest}}{E}. \tag{5.18}$$

Note that although natural units are used to relate energy mass and momentum, the speed of light above is in cm/ns to maintain consistency between the units of velocity with units of time and length in the analysis software.

### 5.1.3 GSIM

A `GEANT` based model of the detector known as `GSIM` was implemented to estimate acceptance. `GSIM` takes the kinematics for each particle track and simulates corresponding detector responses for each subsystem of CLAS. The particle kinematics are integrated with a model of the toroidal magnetic field and the CLAS detector to simulate a signal. For the familiar reader, values of parameters used in the `GSIM` `ffread` card are provided in Fig. 5.2. More information on `GSIM` can be found in Ref. [47].

```
============FFREAD.G12=====================
CUTS   5.e-3 5.e-3 5.e-3 5.e-3 5.e-3
DCCUTS 1.e-4 1.e-4 1.e-4 1.e-4 1.e-4
ECCUTS 1.e-4 1.e-4 1.e-4 1.e-4 1.e-4
SCCUTS 1.e-4 1.e-4 1.e-4 1.e-4 1.e-4
MAGTYPE 2
MAGSCALE 0.500 0.000
PTGIFIELD 0
STTYPE 1
STZOFF -90.0
TGPOS 0. 0. 0.
TARGET 'g11a'
TGMATE 'PROT'
POSBEAM 0.0 0.0
GEOM 'ALL' 'ST'
NOGEOM 'MINI' 'PTG '
BEAM00 5.744
DCAY 1
KINE 1
MULS 1
AUTO 1
RUNG 56855
TIME 1000000 1000000 1000000
TRIG 1000000
STOP
```

Figure 5.2: The ffread card used with gsim for our analysis.

### 5.1.4 GPP

GPP uses the output of GSIM and smears the timing signals by randomized displacements, the extent of which is specific to user input and the characteristics of each subsystem. The necessity of this program comes from the fact that GSIM tends to output better resolution than real signals from CLAS. Some of GPP's flags and parameters are found in Fig. 5.2. The broadened signals include the readout from the drift chambers and time of flight scintillators. Broadening of scintillator signals are done according to their dimensions, i.e. a longer scintillator requires a wider smearing function. After the simulated signals have been processed, they go through the reconstruction software a1c, which is described in Chapter 4, and processed with the same analysis code as the real data.

## 5.2 Tuning Simulation to Data

In order to ensure the simulated events are representative of the data, a comparison was made between the accepted events and the data for a number of quantities. The Monte Carlo data were generated iteratively with tuning of parameters including:

- Beam energy spectrum
- Exponential $t$-slope, which is a quantity related to Mandelstam variable $t$ and described in Section 5.2.2
- Production-resonance mass and width
- Input $\Xi^-$ polarization

This is not an exhaustive list; there are many other kinematic quantities to which the acceptance may be sensitive. It will be shown in this section however, that the four quantities listed above provide a sufficient basis for matching Monte Carlo events to the data and determining the acceptance.

### 5.2.1 Simulated Beam Energy Spectrum

Tuning the simulated photon-beam energy spectrum to the data's began with generating events according to a reasonable but arbitrary spectrum. Matching was done by breaking our data and the first iteration's reconstructed events into 27 photon-beam energy bins from 2.8 Gev to 5.5 GeV (100 MeV wide). For each energy bin, a weighting factor $W_i$ was calculated by,

$$W_i = N_i^{data}/N_i^{rec_1}. \tag{5.19}$$

Where $N_i$ is the number of reconstructed events in each energy bin for data or simulation. The next iteration of Monte Carlo events had an energy spectrum obtained by multiplying the first iteration's number of generated events with the respective weighting factor, then multiplied by an overall normalization.

$$N_i^{gen_2} = W_i N_i^{gen_1} \frac{\sum N_i^{rec_1}}{\sum N_i^{data}}, \tag{5.20}$$

where $N_i^{gen_2}$ is the number of Monte Carlo events generated in the second iteration. In the absence of other changes to kinematics of the simulation, the iterative process would only need to be repeated twice. However since other kinematic quantities were being tuned simultaneously, beam tuning was repeated multiple times. An overlay of the final beam energy spectrum for data and simulated events is shown in Fig. 5.3.

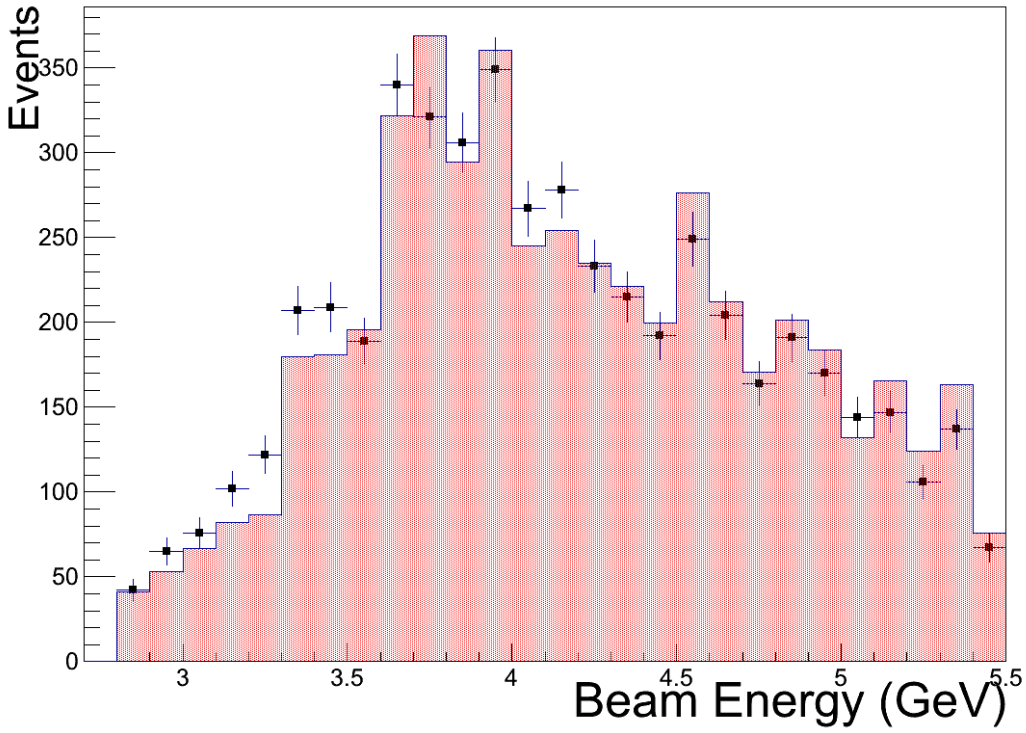


Figure 5.3: The beam energy spectrum for the $\Xi^-$ data sample and Monte Carlo simulation. The Monte Carlo events are in red and are normalized to the data represented as points with statistical error bars.

### 5.2.2 Exponential $t$-slope

The $t$-slope is a parameter in the relationship between differential cross section and the Mandelstam-variable $t$ for a two-body nuclear interaction, $t$ is given by,

$$t = (p_1 - p_3)^2 = (p_2 - p_4)^2, \tag{5.21}$$

where $p_i$ represents the $i$th particle's four-vector. Refer to Fig. 5.4 for further clarification. $t$ measures momentum transfer from the photon to the $\Xi^-$. The $t$-slope

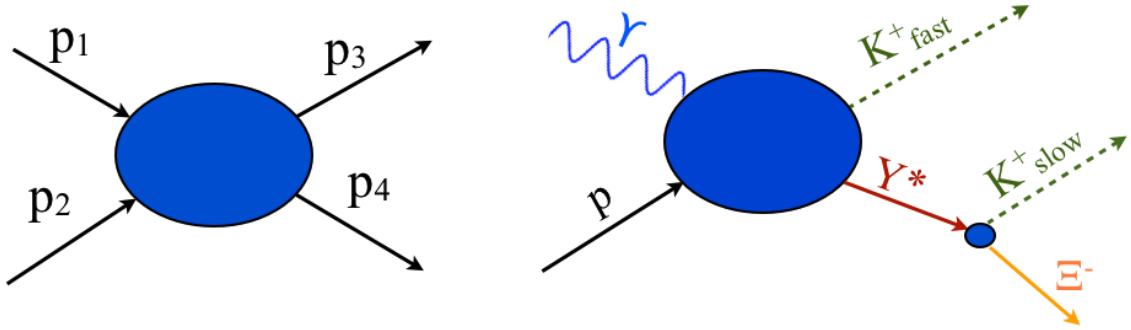


Figure 5.4: The left shows a diagram of a generic interaction with two particles in the initial ($p_1$ and $p_1$)and two particles in the final state ($p_3$ and $p_4$) as referred to in Equation. 5.21. On the right is the analogous model of the $\gamma p \to K^+K^+(\Xi^-)$ reaction. It's should be clear from this diagram and Equation. 5.21 that in this model, $t$ is the momentum transfer from the photon to the fast kaon. The blue ellipses in both figures represent arbitrary intermediate processes.

is denoted as $\alpha$ and is defined according to an assumption regarding the form of the cross section,

$$\frac{d\sigma}{dt} = Ae^{\frac{-t}{\alpha}}. \tag{5.22}$$

Above, $\frac{d\sigma}{dt}$ is the differential cross section with respect to $t$ and $A$ is a constant.

The $t$-slope of our data was determined by measuring the acceptance corrected yield in bins of $t$, then fitting the plot of yield vs $t$ with an exponential function. The fitting procedure was done in 8 separate photon-energy bins. Tuning the $t$-slope spectrum began with a reasonable guess. The first iteration of Monte Carlo events provided rudimentary acceptance corrections that were applied to the data, in turn providing a first estimate on its $t$-slope spectrum. The resultant acceptance corrected $t$-slope spectrum was then used as an input for the second iteration of Monte Carlo event generation. The process was repeated until convergent and stable $t$-slope spectra were

obtained. The flow chart displayed in Fig. 5.5 depicts the iterative process. Fig. 5.6 shows the $t$-slope spectra for simulated and experimental data, and Fig. 5.7 shows a number of quantities used for matching.

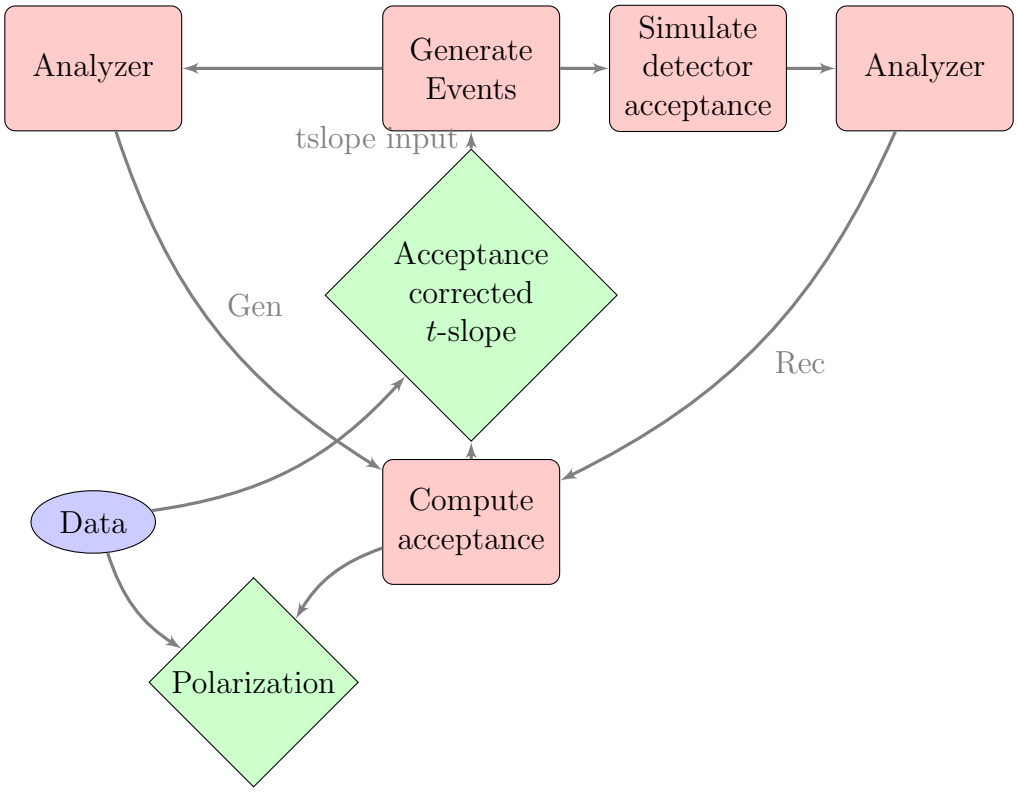


Figure 5.5: First, events are generated. The initial simulation splits into two sets: reconstructed events (Rec) that pass through gsim, gpp and a1c before being analyzed, and generated events (Gen) that pass straight to the analyzer. Acceptance corrections are obtained from the ratio of reconstructed to generated events. Applying acceptance to data, one obtains the corrected $t$-slope spectrum which can in turn be used as input for the next iteration.

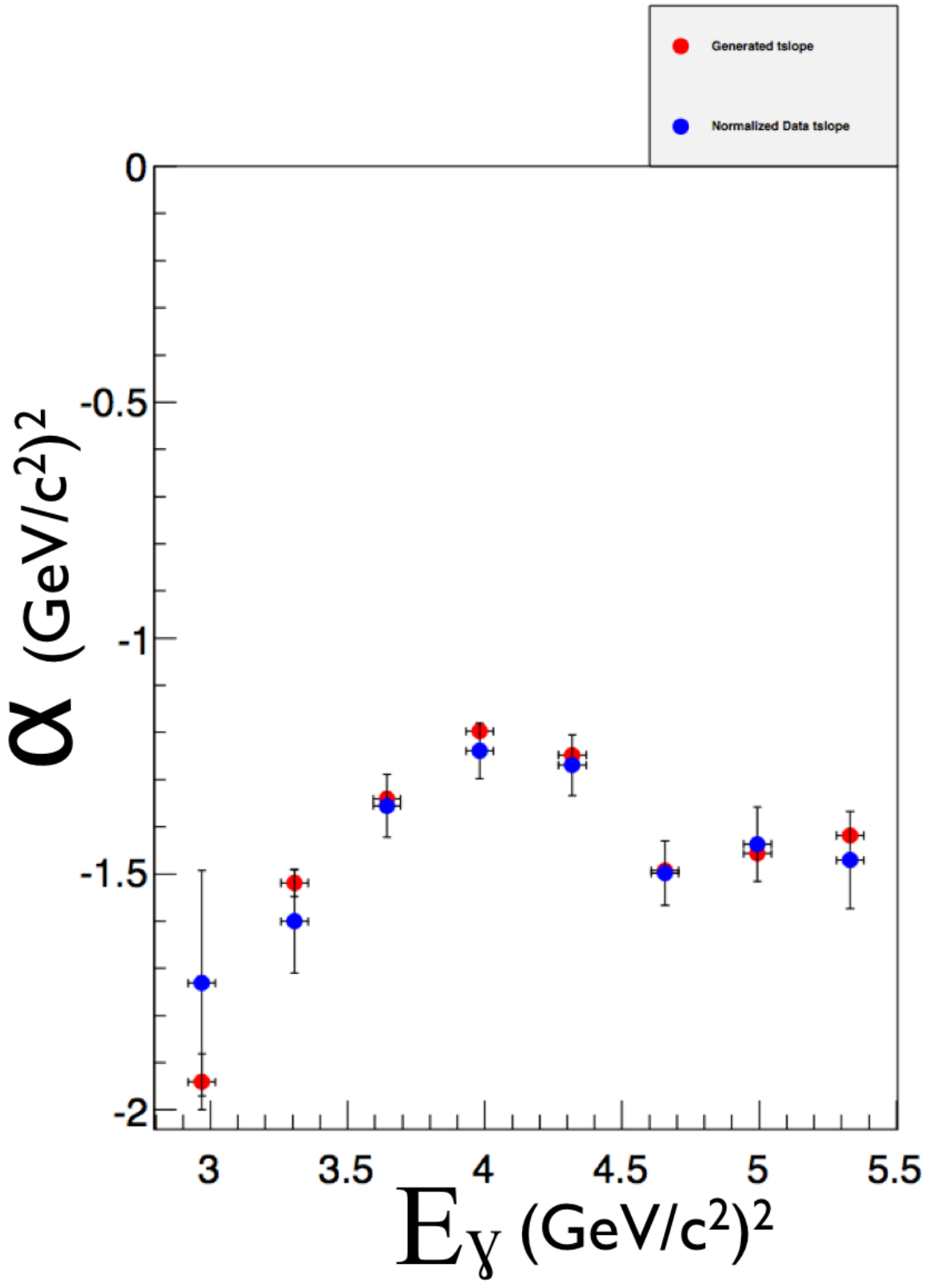


Figure 5.6: $t$-slope for the acceptance corrected experimental data (blue), and the generated Monte Carlo events (red). Agreement within statistical uncertainty is shown.

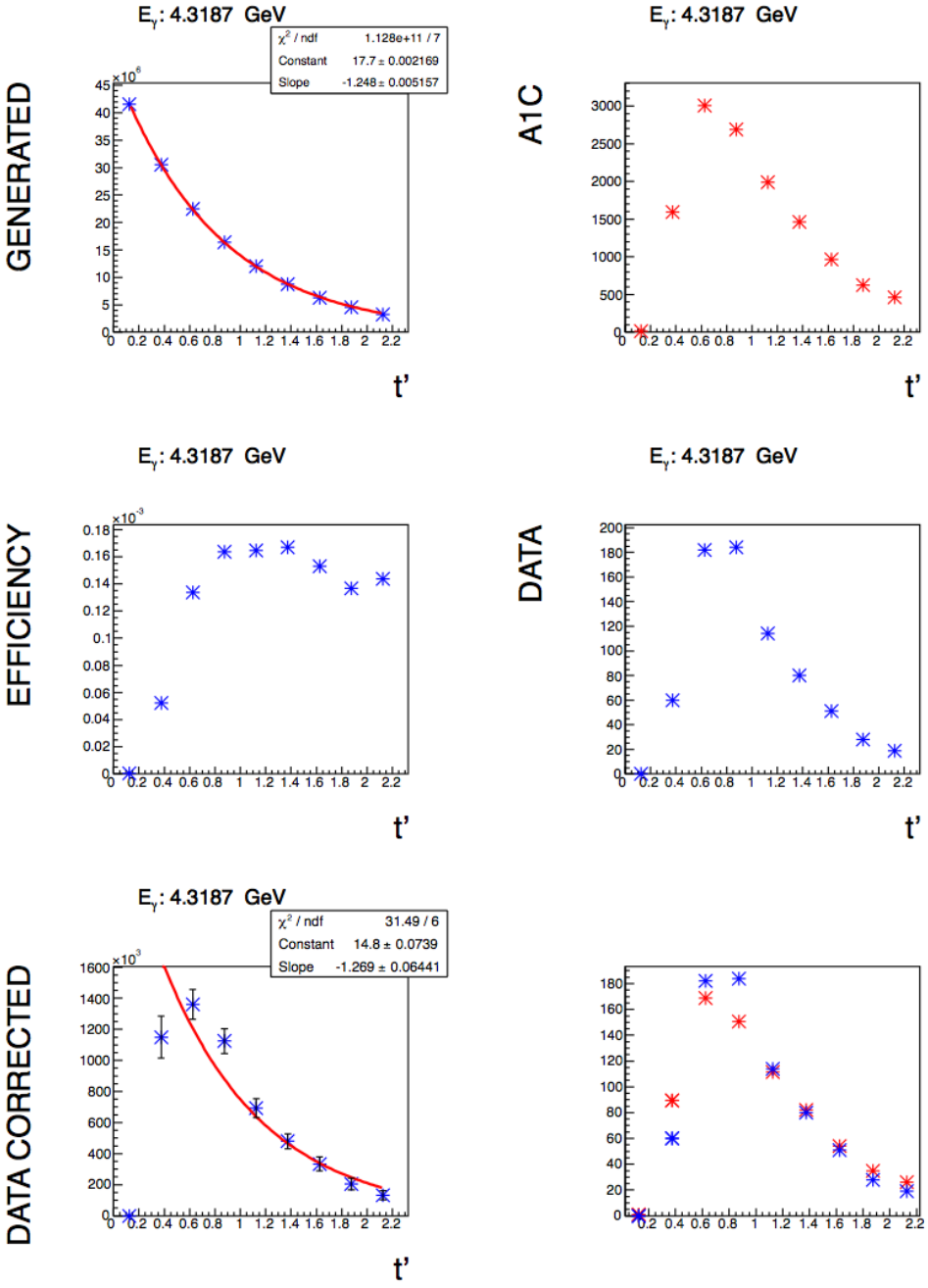


Figure 5.7: An example of the plots that were used to calculate $t$slope. The top two plots show the $t$-spectrum for Monte Carlo generated (left) and reconstructed events (right). The center left shows the calculated acceptance as a function of $t$ while center right shows the uncorrected $t$-spectrum of the data. The bottom right is an overlay fo the uncorrected $t$-spectrum of Monte Carlo and Data events. Finally, the bottom left shows the acceptance corrected $t$-spectrum of the data with an exponential fit.

### 5.2.3 Resonance Mass and Width

Our simulated production model assumes contributions from various intermediate resonant hyperon decays. In the case of $\Xi^-$ photoproduction the primary resonances are believed, due to strangeness conservation in the strong and electromagnetic interactions, to be excited states of the $\Lambda$ and $\Sigma$ (i.e. $Y^*$) having decay modes $Y^* \to K^+\Xi^-$. The coupling amplitudes across the $Y^*$ spectrum for $\Xi^-$ production are unknown,[1] but the *effective* resonance mass spectrum for the simulation was matched to the data in various energy bins. An overlay of $Y^*$ mass spectra for data and simulation is plotted in Fig. 5.8 and 5.9.

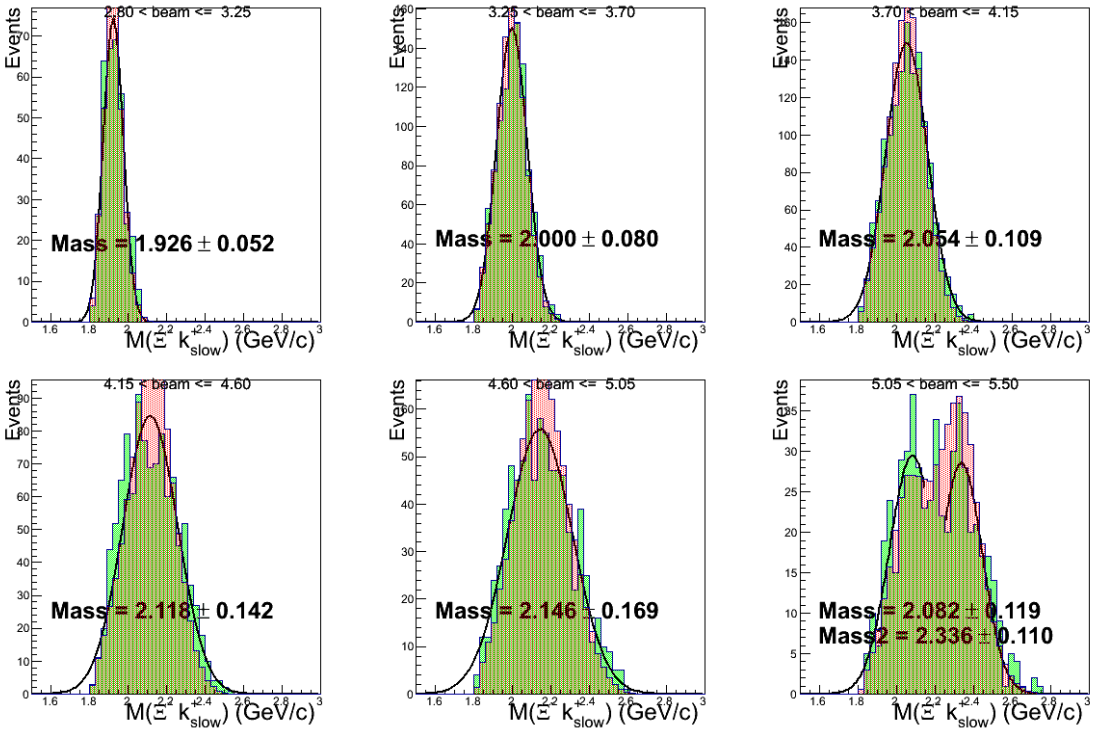


Figure 5.8: An overlay of the data (green) and simulation (red) for the invariant mass $m(\Xi^- K^+_{slow})$ in six distinct beam-energy bins. The data were fit to Gaussian functions which yields the mass and width of the underlying hyperon used as in input parameter for simulation.

[1] Furthering knowledge on cascade production amplitudes is one of the goals of our analysis.

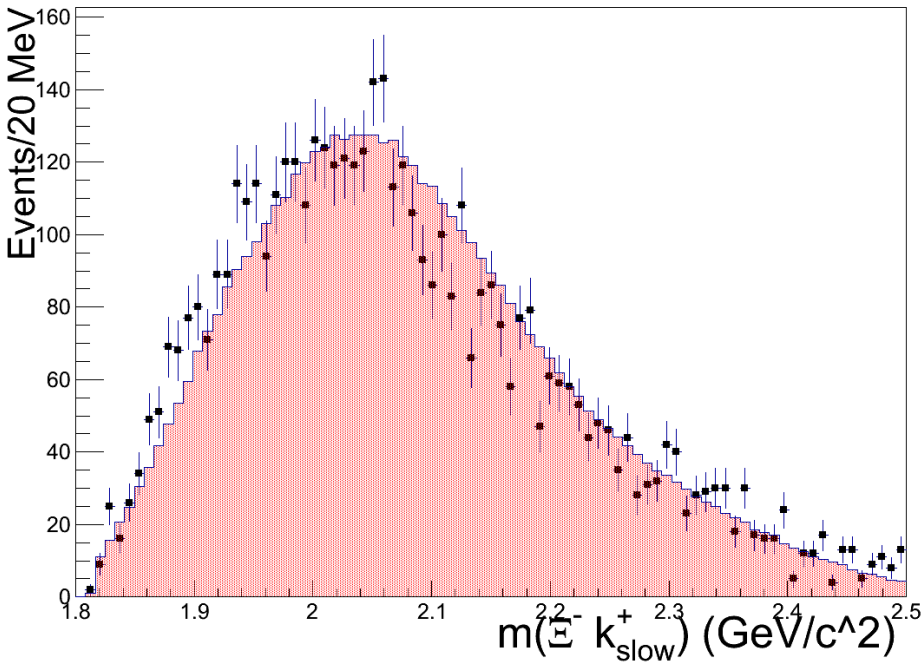


Figure 5.9: An overlay of the data (points) and simulation (red solid) for the invariant mass $m(\Xi^- K^+_{slow})$ integrated over all bins.

### 5.2.4 Further Comparison of Simulated and Experimental Data

There are many kinematic degrees of freedom in the simulation: vertex position and momentum for all three final state particles, along with beam energy, to name a few. Various combinations of the above mentioned variables compose observables that were tuned to the data. A number of additional quantities that were not directly tuned may be compared to ensure the simulation is representative of the data. Good agreement between data and simulation are shown in Figs. 5.10, 5.11 and 5.12.

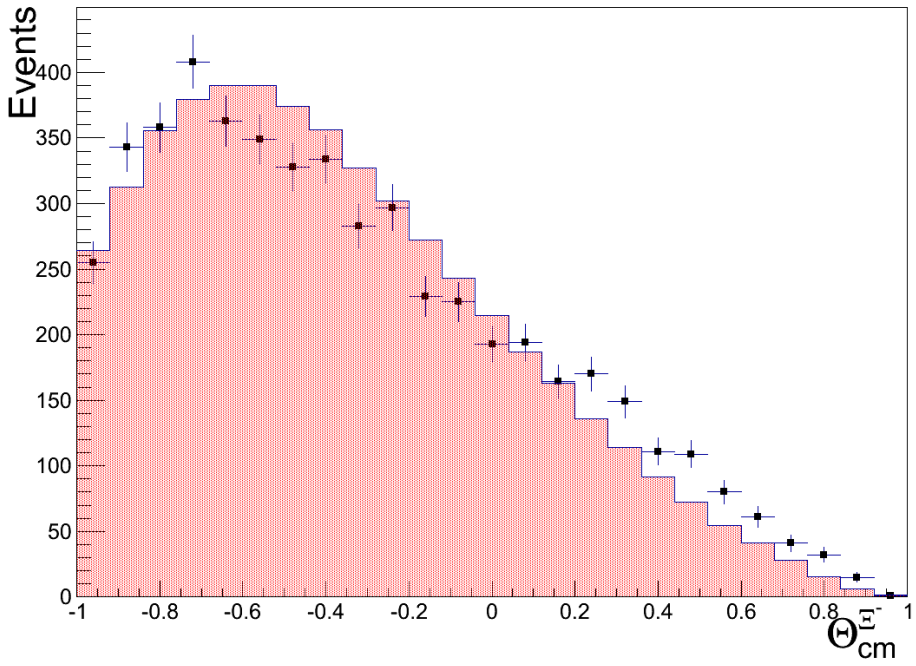


Figure 5.10: Shows the measured cascade angle with respect to the $z$-axis in the center of mass frame. This quantity depends on the intermediate $Y^*$ mass and width, along with the $t$-slope. Red is simulated events and the points are the data.

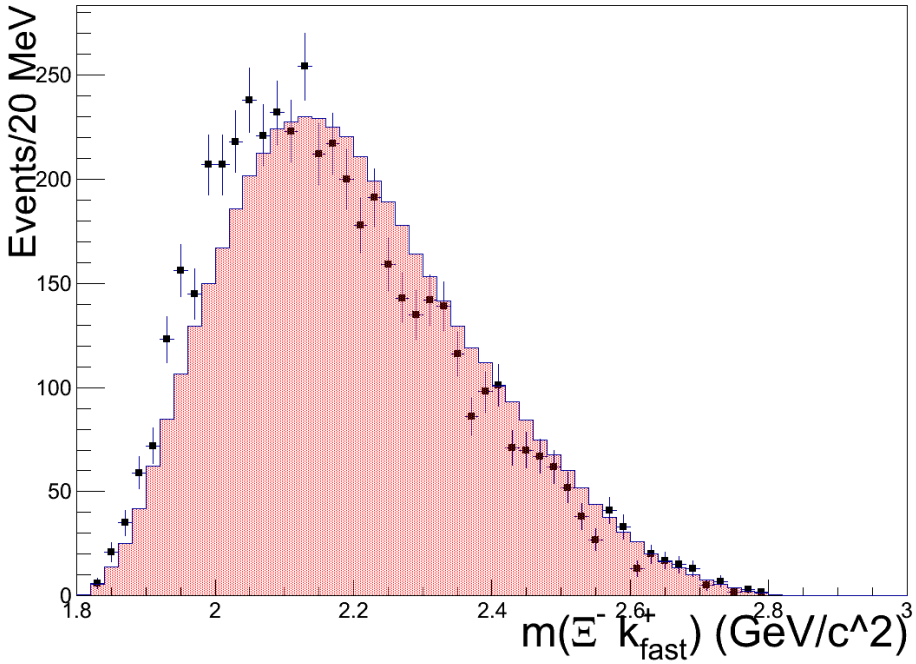


Figure 5.11: The invariant mass of the $K^+_{fast} + \Xi^-$ system. Red is simulated events and the points are the data.

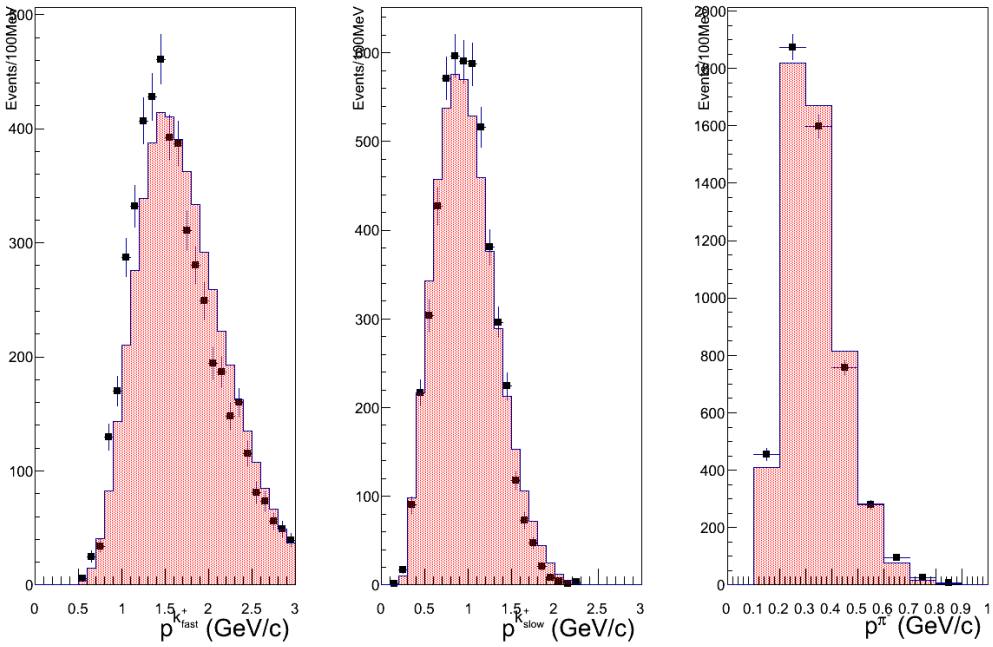


Figure 5.12: The magnitude of momentum for all three mesons. Red is simulated events and the points are the data.

## 5.3 Acceptance Functions

Histograms of acceptance vs. pion angle across $\hat{x}, \hat{y}$ and $\hat{z}$ (axes defined in Chapter 3) were plotted in several hundred bins of beam-energy and center-of-mass cascade angle. The plots were fit to ten-degree polynomials in pion angle. Our final integrated acceptance function was defined by fits in all bins and was applied to each event in the data.

### 5.3.1 Calculation of Acceptance and Uncertainty

The acceptance ($\epsilon$) in a given kinematic bin is determined by the ratio of reconstructed events ($r$) to generated events ($g$).

$$\epsilon = \frac{r}{g}. \tag{5.23}$$

Since $r$ and $g$ are correlated, the uncertainty of the acceptance can not be calculated using the method of quadratures. However the expression for the acceptance can be de-correlated by,

$$\epsilon = \frac{r}{r+n}, \tag{5.24}$$

where $n$ is the number of events which failed to be reconstructed. The uncertainty can thus be determined through quadrature,

$$\delta_\epsilon^2 = (\frac{\partial \epsilon}{\partial r}\delta_r)^2 + (\frac{\partial \epsilon}{\partial n}\delta_n)^2. \tag{5.25}$$

Which leads to the uncertainty in the efficiency,

$$\delta_\epsilon = \frac{1}{g}\sqrt{r(1-\epsilon)}. \tag{5.26}$$

The efficiency was plotted with $\cos\theta^i_{\pi^-}$ where $\imath = x, y, z$ (for a discussion on the coordinate system see Chapter 3). Ten-degree polynomials sufficed as fitting functions to reflect the structure of acceptance. The three acceptance functions,

$$A(\theta^{x,y,z}_{\pi^-}) = \sum_{n=0}^{10} c_n^{x,y,z} x^n, \tag{5.27}$$

represent the acceptance of events in kinematic bins of photon energy ($E_\gamma$) and center of mass $\Xi^-$ angle with the $z$ axis [2] ($\cos\theta_{\Xi^-}$). Fig. 5.13 shows a number of typical acceptance functions in various bins. For simpler notation, $A_j$ will be used to represent a acceptance for an event $j$.

If $N$ is the detected-number of events, then applying the acceptance on each event

[2] As a reminder, the z-axis is parallel with the photon momentum in the center of mass frame.

gives the corrected-number of events $N'$ as,

$$N' = \sum_{j=1}^{N} \frac{1}{A_j}. \tag{5.28}$$

To approximate the uncertainty in $N'$, consider that the acceptance $A_i$ varies little from the average acceptance $A$ within each kinematic bin. One can write,

$$N' \approx \frac{N}{A}. \tag{5.29}$$

The square of the relative uncertainty is then,

$$(\frac{\delta N'}{N'})^2 = (\frac{\delta N}{N})^2 + (\frac{\delta A}{A})^2. \tag{5.30}$$

So,

$$\delta N' = N' \sqrt{(\frac{\delta N}{N})^2 + (\frac{\delta A}{A})^2}. \tag{5.31}$$

Or,

$$\delta N' = N' \sqrt{(\frac{1}{N}) + (\frac{\delta A}{A})^2}. \tag{5.32}$$

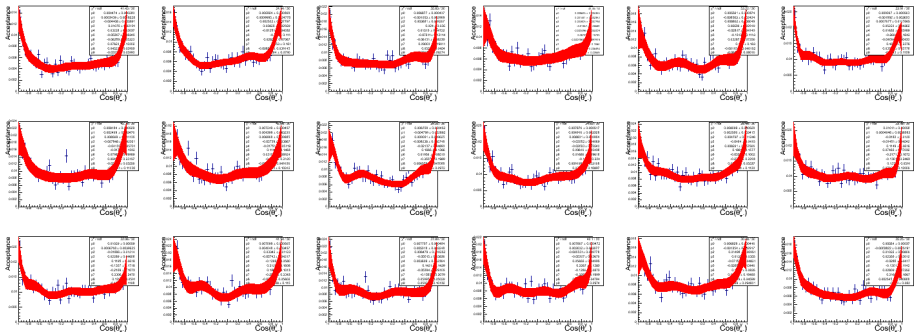

Figure 5.13: A few typical acceptance functions ($A(\theta^y_{\pi^-})$) in various bins of beam energy and cascade angle. The red lines show the fits to the underlying acceptance-histograms with their widths representing the uncertainty as calculated by the covariance matrices of fitting parameters.

# Chapter 6

# Results

This chapter provides the outcome of our cascade polarization measurements in the reaction $\gamma p \to K^+K^+\Xi^-$. Summary tables and discussions for the induced and transfered polarization are provided in Sections 6.1.1 and 6.2.1 respectively. A comparison between results and predictions from the only known theoretical model of cascade photoproduction is also provided in Section 6.3, with a discussion on the comparison in Section 6.3.1.

## 6.1 Induced Polarization $P$

The observable $P$ was measured in nine kinematic bins as shown in Fig. 6.1. We found $P$ to be consistent with zero in all but one bin, although the results also match the predictions of Ref. [11]. The single non-zero bin yielded a value $P = 0.233 \pm 1.84$, which constitutes a $1.26\sigma$ deviation from zero, which is likely to be a statistical fluctuation. Rebinning of the results according to various schemes consistently yielded $P = 0$ within statistical uncertainty. Integrating over all bins, we found $P = 0.027 \pm 0.061$. Higher precision measurements in three energy bins and three cascade angle bins are shown in Figs. 6.2 and 6.4. Additionally, we applied acceptance corrections based on data-tuned Monte Caro events as described in Chapter 5. We found that acceptance corrections had virtually no effect on $P$ when measured by the forward-backward asymmetry method, as is demonstrated in Fig. 6.3 and Table 6.1. Thus, the measurements without acceptance corrections were taken as the nominal results. The systematic uncertainty introduced to $P$ by acceptance is quantified in Chapter 7.

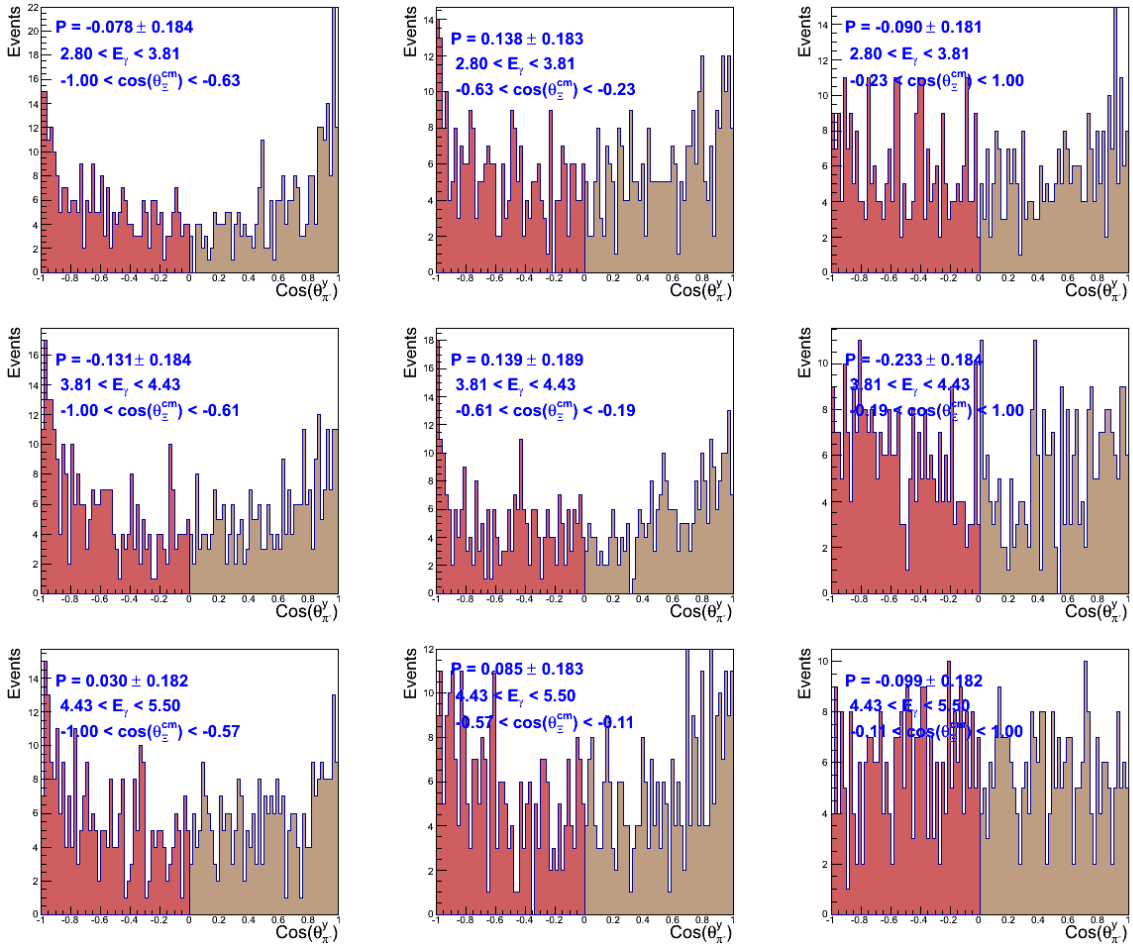


Figure 6.1: The angular distribution of the pion off $\hat{y}$ in nine bins of energy and center of mass cascade angle. The forward-backward asymmetry is used to calculate the induced polarization $P$.

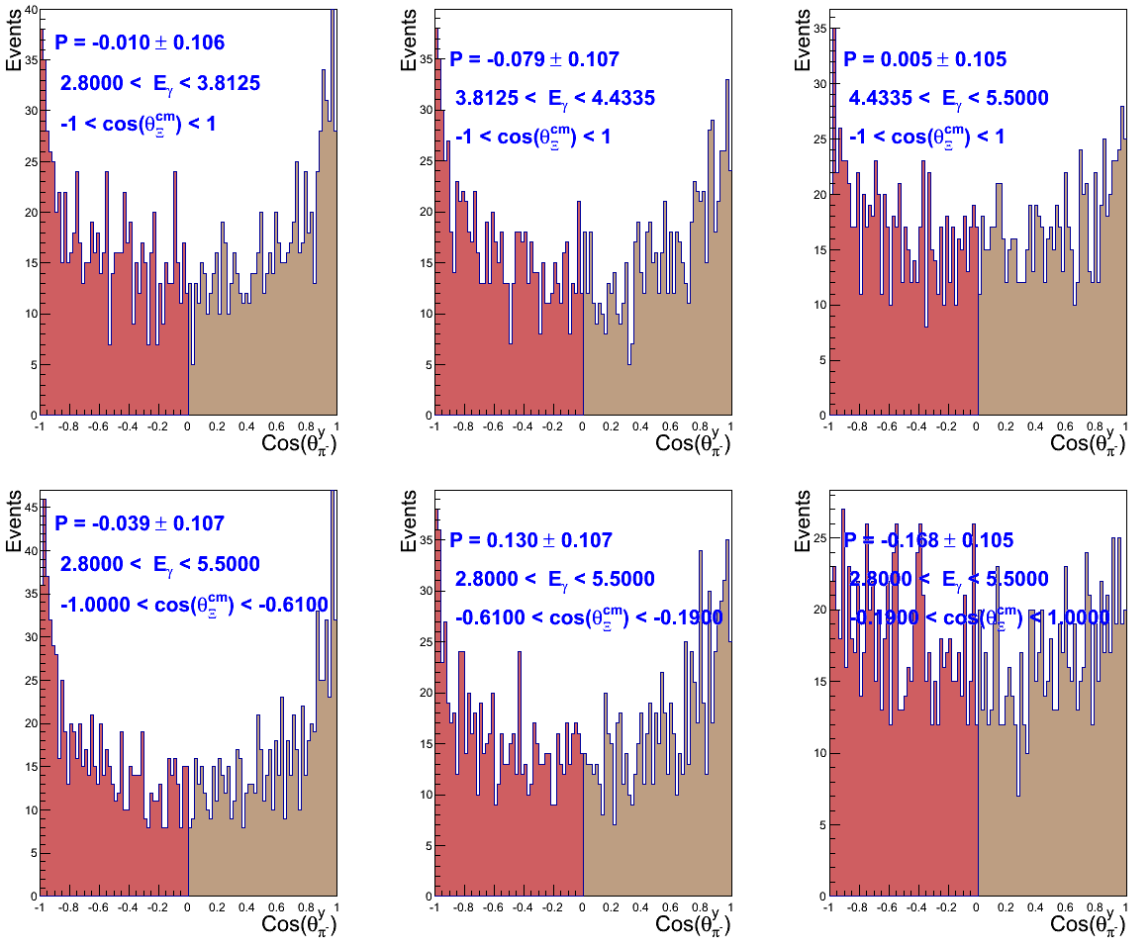


Figure 6.2: The angular distribution of the pion off $\hat{y}$ in three bins of energy (top) and three bins of center of mass cascade angle (bottom). The forward-backward asymmetry is used to calculate the induced polarization $P$.

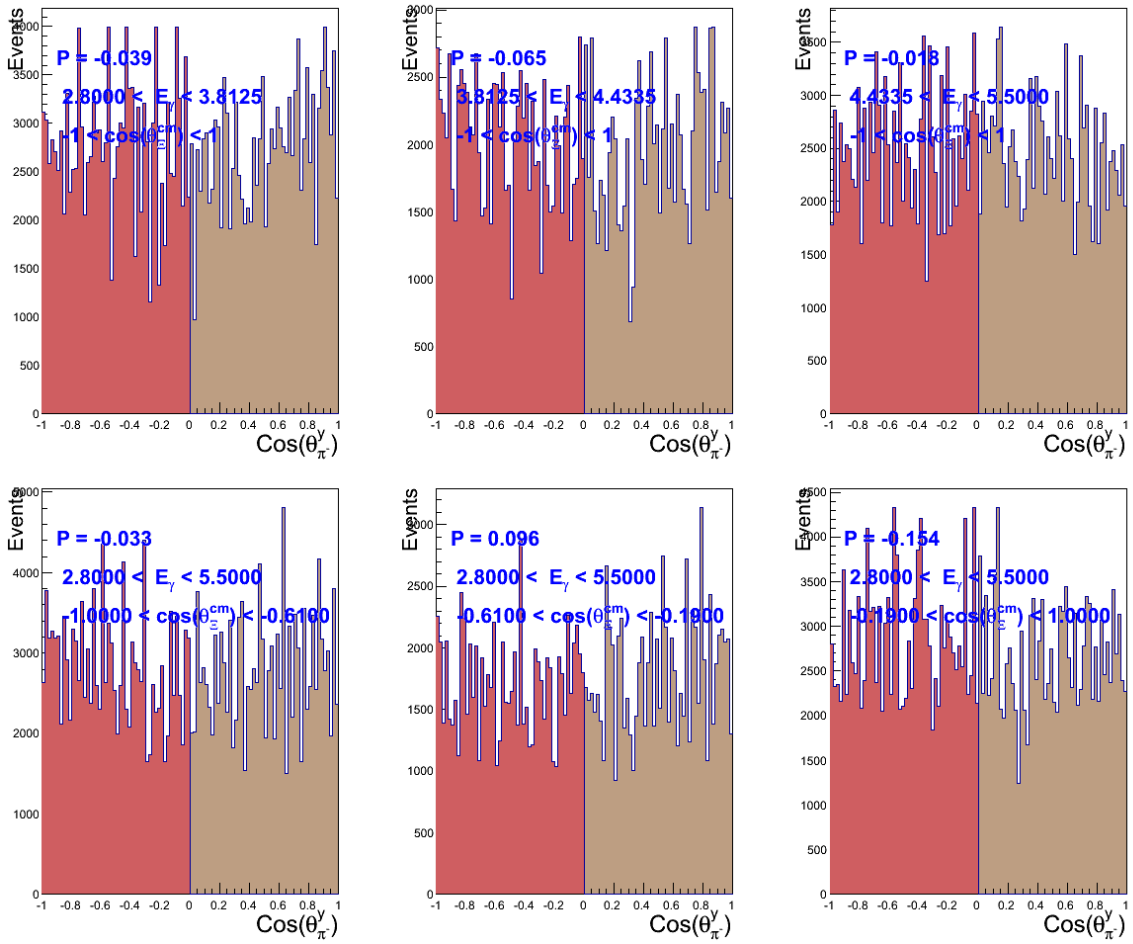


Figure 6.3: As one cross check for the cancellation of acceptance, the acceptance-corrected angular distribution of the pion off $\hat{y}$ is shown.

| $E_\gamma$ | 3.47 GeV | 4.09 GeV | 4.88 GeV |
|---|---|---|---|
| P With AC | -0.039 | -0.065 | -0.018 |
| P No AC | -0.010 ± 0.106 | -0.079 ± 0.107 | 0.005 ± 0.105 |

| $\cos\theta_\Xi^{cm}$ | -0.79 | -0.41 | 0.19 |
|---|---|---|---|
| P With AC | -0.033 | 0.096 | -0.154 |
| P No AC | -0.039 ± 0.107 | 0.130 ± 0.107 | -0.168 ± 0.107 |

Table 6.1: A table summarizing the results for $P$, with and without acceptance corrections. There is good agreement between both methods for all six bins, well within statistical uncertainty.

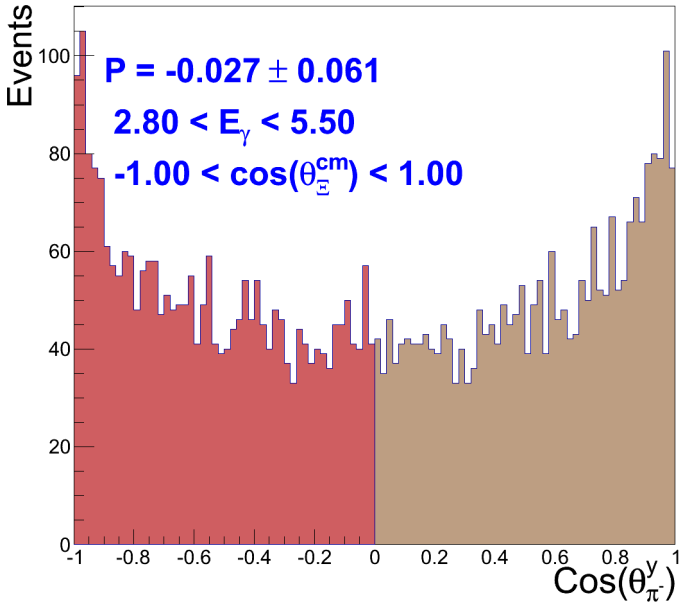


Figure 6.4: Angular distribution of the pion off $\hat{y}$, integrated over all bins. The forward-backward asymmetry is used to calculate the induced polarization $P$. The measured value of $P$ is constant with zero.

### 6.1.1 Comments on Induced Polarization Results

Our results for $P$, summarized in Table 6.2, which hold independent of beam and target polarization, show small or zero induced-polarization for the cascade within our experimental kinematic range. The near-zero integrated value of $P$ differs significantly from what was reported for $\Lambda$ production under similar conditions in Ref. [48], which showed prominent structure for $\gamma p \to K^+\Lambda$ for $P$, with values as high as $\pm 0.5$ for many bins. However, finer binning and statistical precision was achievable for the $\Lambda$ analysis due to higher production cross sections. Probing for narrow structures in $P$ for the cascade must wait until enough data are available to bin more finely. Although not directly reported, the bin-integrated results of [48] "cancel" among bins to some degree, in particular for integrating forward and backward angles, which makes better correspondence with our results. In any case, our $P$ results suggest the polarization mechanism for the cascade and $\Lambda$ differ to some degree, although both mechanisms still remain speculative. There is no reason to assume, that induced-polarization features for doubly and singly strange baryons should resemble one another, especially when comparing single-meson and double-meson production. On the other hand, possible explanations for the differing features of induced polarization could pertain to different diquark configurations of the $\Lambda$ and $\Xi^-$.

Interestingly, our observation of a small induced polarization for the cascade corresponds well with expectations derived from diquark considerations. In the diquark picture, the cascade inherits its spin from the down-quark which in turn, is likely inherited from the unpolarized proton target. Future studies on target polarization transfer could help further elucidate the role of diquark effects and down-quark contributions to the cascade polarization mechanism.

| $P$ | 3.47 GeV | 4.09 GeV | 4.88 GeV $E_\gamma$ |
|---|---|---|---|
| -0.79 | -0.078 ± 0.184 | 0.138 ± 0.183 | -0.090 ± 0.181 |
| -0.41 | -0.131 ± 0.184 | 0.139 ± 0.189 | -0.233 ± 0.184 |
| 0.19 $\cos\theta_\Xi^{cm}$ | 0.030 ± 0.182 | 0.085 ± 0.183 | -0.099 ± 0.182 |

Table 6.2: A table summary of induced polarization values binned in center-of-mass $\Xi^-$ angle and beam energy.

Induced polarization, which relates to interference between real and imaginary parts of its production amplitudes, provides a sensitive test for possible production mechanisms. Our results are compared with the theoretical models of Refs. [11, 14] and are discussed in Section 6.3.

### 6.1.2 Alternate Methods for Induced Polarization

For an alternative way to measure $P$, the acceptance corrected angular distribution of the pion off $\hat{y}$ was fit to a first degree polynomial, as described in Chapter 3. This method showed good agreement with the primary algorithm used to extract $P$ in Figs. 6.1 and 6.2. The acceptance was characterized as a function of beam energy, cascade angle, and pion angle then applied to the data in Fig. 6.5.

### 6.1.3 Further Cross Checks for Induced Polarization

[h] Additional cross checks for acceptance cancellation were performed by simulating events with various effective $\Xi^-$ induced polarization values, $P_{gen}$. The measured value for the reconstructed events, $P_{rec}$, were consistently in agreement with what was

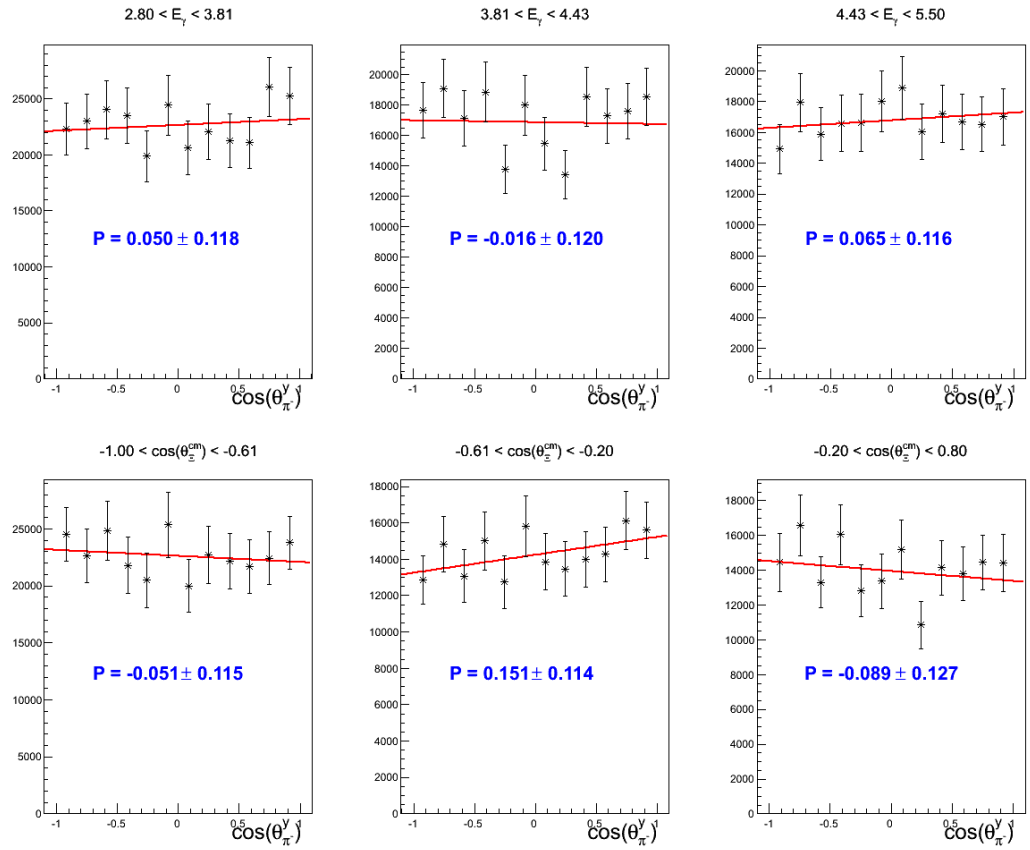


Figure 6.5: Fitted acceptance corrected pion angular distributions and the resulting measurement of $P$. Agreement with the primary measurements shown in Fig. 6.2 is evident for all bins within statistical uncertainty.

generated. The agreement $P_{gen} = P_{rec}$ demonstrates the cancellation of acceptance for the forward-backward asymmetry method. Fig. 6.6 shows the measured value $P_{rec} = 0$ deviating less than $1\sigma$ from $P = 0$ for reconstructed Monte Caro events corresponding to a generated value of $P_{gen} = 0$. We found MC events generated with higher input polarization $P_{gen}$ deviated more than those generated with low or zero polarization. Fig. 6.7 shows consistency with the measured value $P_{rec} = -0.5$ deviating less than $1\sigma$ in all but one bin for a generated value of $P_{gen} = -0.5$.

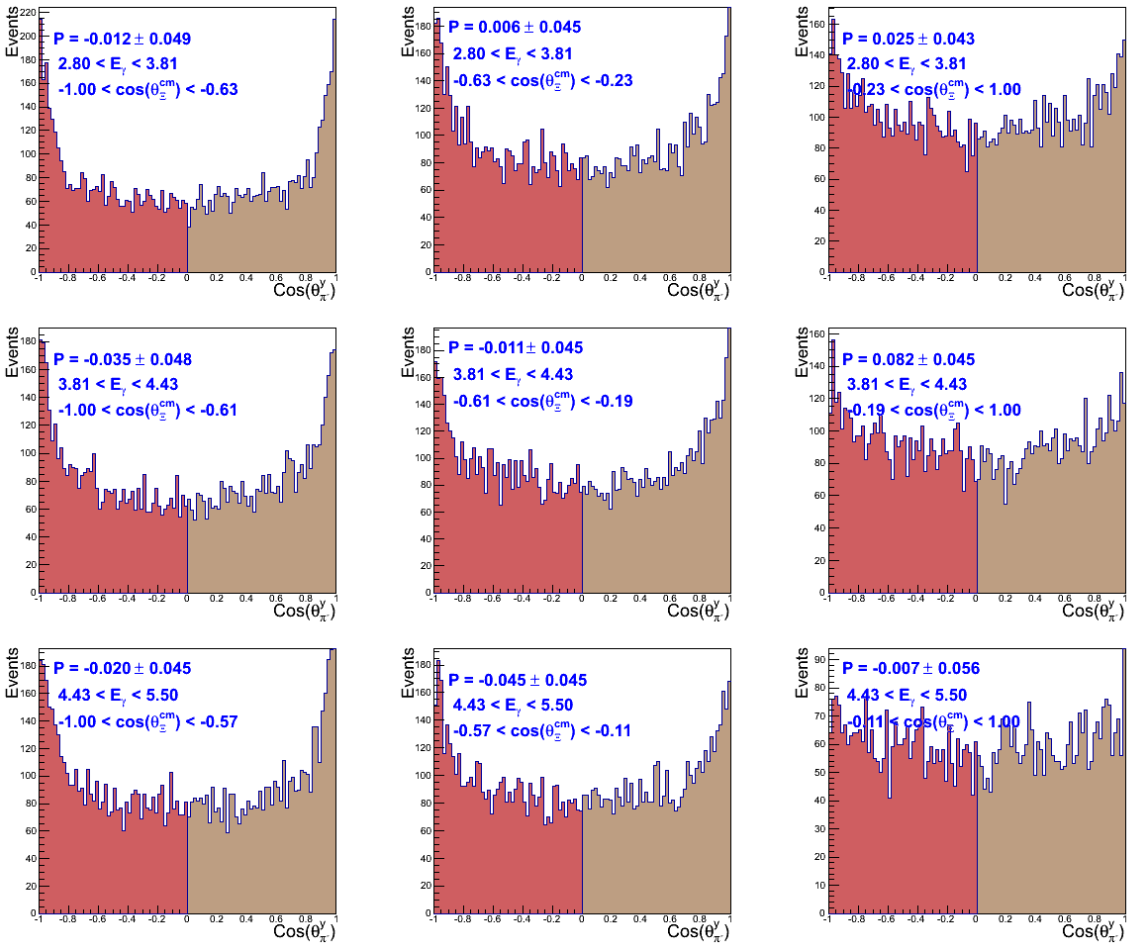


Figure 6.6: Monte Carlo events generated with $P_{gen} = 0$. The pion angular distributions of the reconstructed events in 9 bins kinematic bins are shown along with the measured value of $P_{rec}$. Better than $1\sigma$ agreement for $P_{rec} = P_{gen}$ is shown in all but one bin, which shows a deviation of less than $1.5\sigma$.

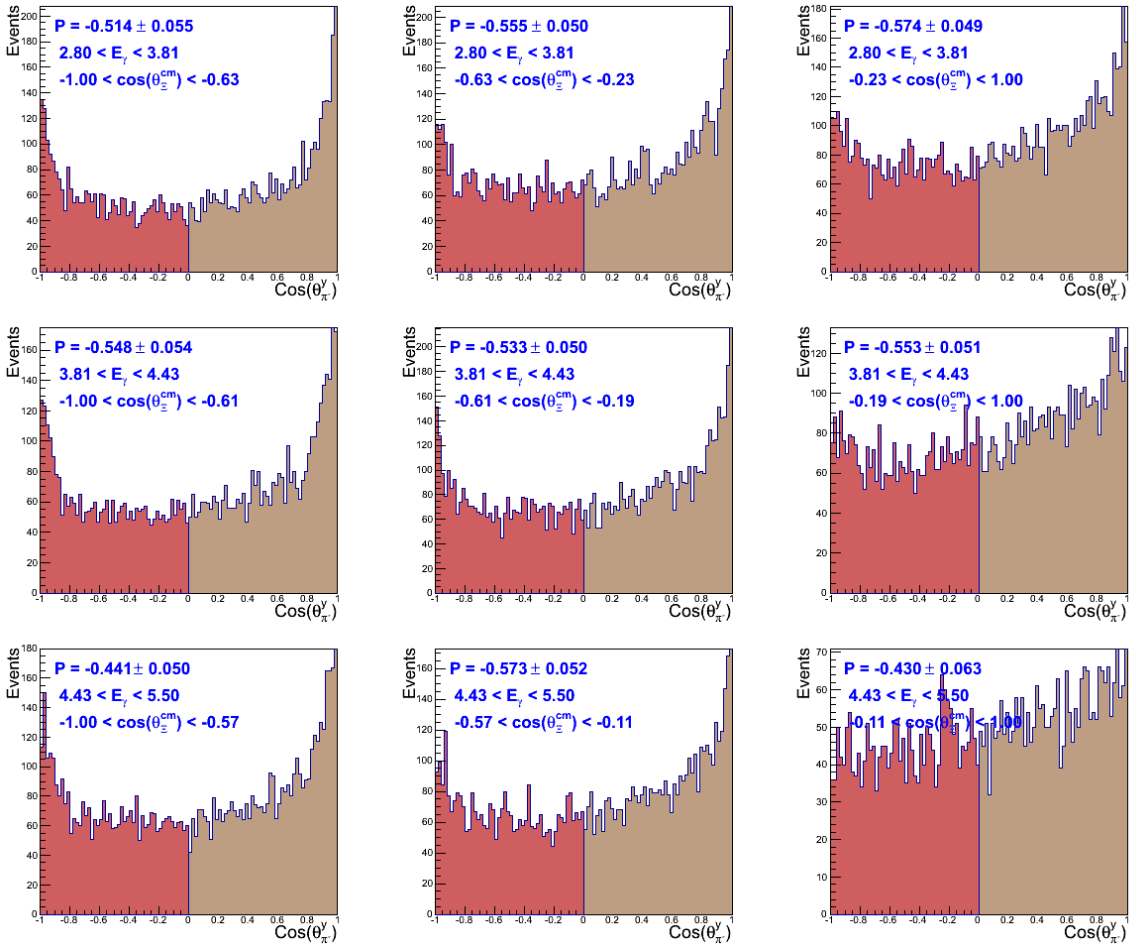


Figure 6.7: Monte Carlo events generated with $P_{gen} = -0.5$. The pion angular distributions of the reconstructed events in nine bins kinematic bins are shown along with the measured value of $P_{rec}$. Close to $1\sigma$ agreement for $P_{rec} = P_{gen}$ is shown in all bins.

## 6.2 Transfered Polarization $C_x$ and $C_z$

Integrated over all kinematic bins, we found $C_x = 0.017 \pm 0.177$, a results consistent with zero. A negative value, $C_z = 0.301 \pm 0.145$ was additionally observed as shown in Fig. 6.8. The finest possible binning scheme with reasonable precision comprised three energy bins integrated over all cascade angles, and three cascade angle bins, integrated over all energy. Our binned results in Fig. 6.9 showed $C_x$ to be consistent with zero in all but one bin. Fig. 6.10 shows $C_z$ to have statistically significant departures from zero, with the highest measured value of $C_z = -0.589 \pm 0.253$ and the lowest $C_z = -0.001 \pm 0.217$.

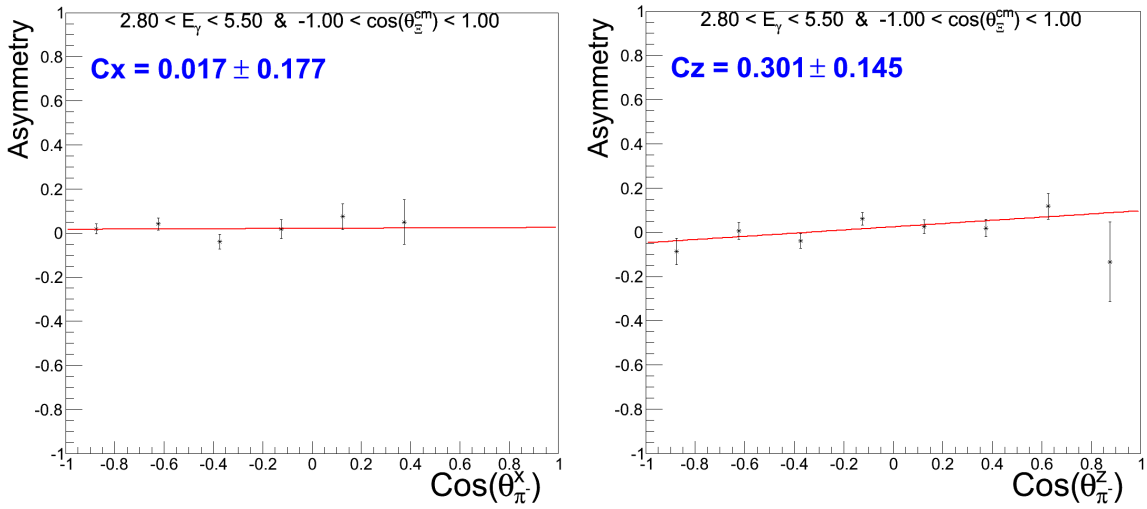


Figure 6.8: Beam-helicity asymmetry as a function of pion angle off $\hat{x}$ (left) and $\hat{z}$ (right), integrated over all bins. The linear fit is used to calculate the transfered polarization $C_x$ and $C_z$.

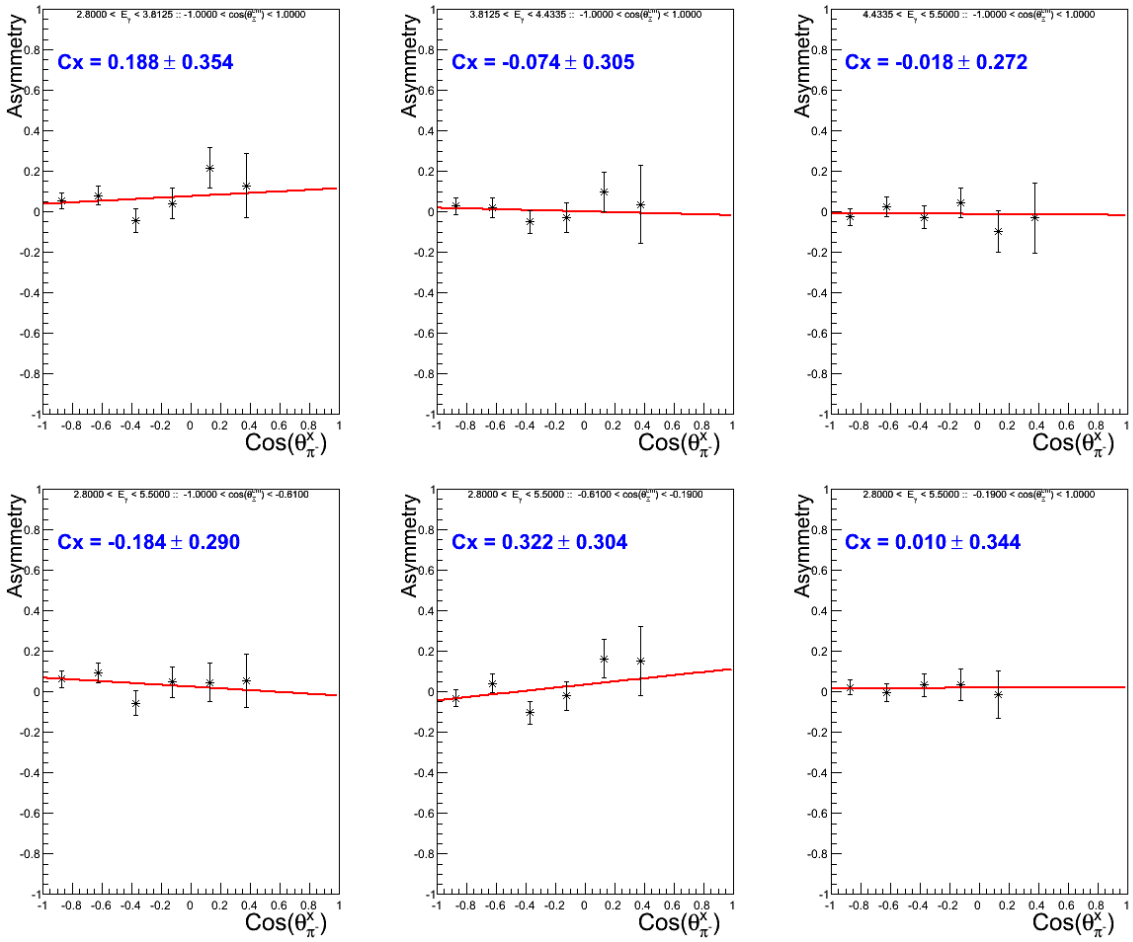


Figure 6.9: Beam-helicity asymmetry as a function of pion angle off $\hat{x}$, in three bins of energy (top) and three bins of center of mass cascade angle (bottom). The linear fit is used to calculate the transfered polarization $C_x$.

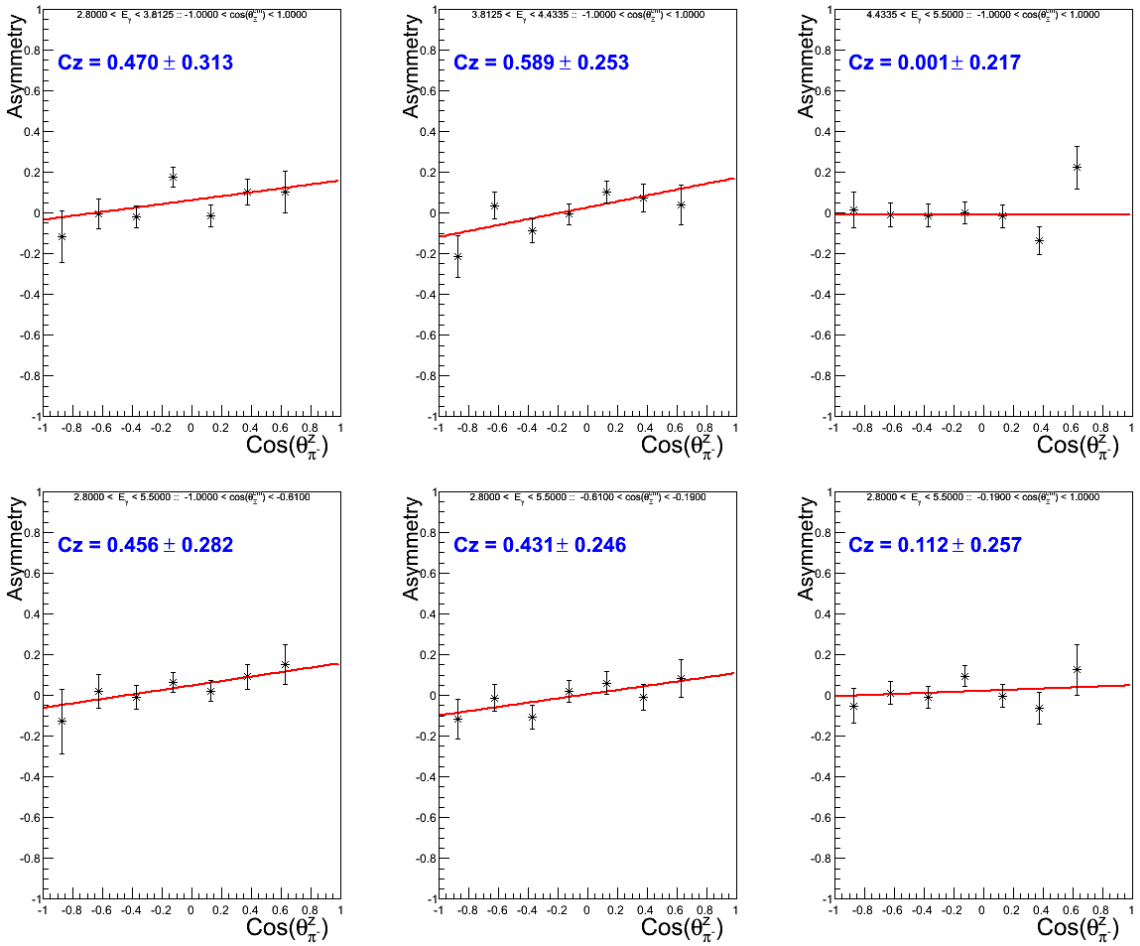


Figure 6.10: Beam-helicity asymmetry as a function of pion angle off $\hat{z}$, in three bins of energy (top) and three bins of center of mass cascade angle (bottom). The linear fit is used to calculate the transfered polarization $C_z$.

### 6.2.1 Comments on Transfered Polarization Results

Our results, summarized in Table 6.3, show a small to intermediate degree of polarization transfer from the photon-beam to the recoil-hyperon. The bin-integrated values of $C_x = 0.017 \pm 0.177$ and $C_z = 0.301 \pm 0.145$ depart greatly from the corresponding observables reported by Ref. [15] for $\Lambda$ photoproduction. In Ref. [15], $C_z$ was large in most kinematic bins often with a value near unity, additionally an empirical constraint $C_z \approx C_x + 1$ was observed, which we do not see for the cascade. Most significantly for $\Lambda$, maximal transfer of polarization in all observed bins occurs; in the case of total circular beam polarization, the $\Lambda$ recoils with 100% polarization *ie* $R_\Lambda \equiv \sqrt{P^2 + C_x^2 + C_z^2} \approx 1$. In contrast, we have shown that the integrated total polarization for the cascade is $\bar{R}_\Xi \approx 0.3$. Aside from the difference in magnitude we observed, we see a similarity between the cascade and the lambda: the total polarization almost entirely comes from $C_z$ (or $\bar{R} \approx C_z$). We qualitatively understand the polarization results of the photoproduced cascade and lambda using the vector meson dominance picture as described in Chapter 1. Our $C_x$ and $C_z$ results suggest that cascade polarization mechanism is similar to that of the lambda.

We did find, within the limited binning scheme, statistically significant kinematic dependence in $C_z$ but not in $C_x$. We measured the highest values of $C_x = 0.322 \pm 0.304$ and $C_z \approx 0.589 \pm 0.253$ in their respective maximal bins. This is not contrary with the diquark picture, as a measurement of large induced polarization $P$ would have been. It is conceivable that the polarized photon could have a *preference* to produce cascades from protons who's down-quarks are aligned (or anti-aligned) with the photon spin. In this indirect way, the photon spin could be found to be correlated with the recoil cascade spin, manifestly as $C_x$ and $C_z$, with the spin transfered from the target. If the photon directly interacts with a valance quark within the proton, the struck quark

| $E_\gamma$ | 3.47 GeV | 4.09 GeV | 4.88 GeV |
|---|---|---|---|
| $P$ | -0.010 ± 0.106 | -0.079 ± 0.107 | 0.005 ± 0.105 |
| $C_x$ | 0.188 ± 0.354 | -0.074 ± 0.305 | -0.018 ± 0.272 |
| $C_z$ | 0.470 ± 0.313 | 0.589 ± 0.253 | 0.001 ± 0.217 |
| $\cos\theta_\Xi^{cm}$ | -0.79 | -0.41 | 0.19 |
| $P$ | -0.039 ± 0.107 | 0.130 ± 0.107 | -0.168 ± 0.107 |
| $C_x$ | -0.184 ± 0.290 | 0.322 ± 0.304 | 0.010 ± 0.344 |
| $C_z$ | 0.456 ± 0.282 | 0.431 ± 0.246 | 0.112 ± 0.257 |

Table 6.3: A table summary of $\Xi^-$ polarization values for the nominal binning scheme.

must have its initial spin anti-aligned with that of the photon in order to have a spin-half final state. In this scenario, the final $s$-quark, must have spin parallel with the initial photon. Subsequent interactions and spin-orbit coupling could precess its polarization but conserve its magnitude. This would manifest as correlations between the photon helicity, and the recoil spin, and be seen in transfered polarization. What we can say regarding the diquark picture at this point is limited however. Experiments involving target polarization may be of great use to decipher the spin structure of the cascade.

Besides probing spin structure and polarization mechanisms, transfered polarization observables tell us about the interference between the complex production amplitudes and can provide tests for possible cascade production mechanisms. Our results are compared with three distinct parameterizations of the theoretical model of Ref. [11] in Section 6.3. Cross checks for our measurement of $C_x$ and $C_z$ are subsequently discussed in Section 6.2.2.

### 6.2.2 Cross Check for Transfered Polarization Results

As shown in Chapter 3, parity conservation of the weak interaction forbids polarization transfer in the $\hat{y}$ direction, i.e. $Cy = 0$. As a cross check for our method, we measured $C_y$ to ensure this physical constraint is observed in the data. Fig. 6.11 shows the measured value of $C_y$ integrated over all energy and cascade angle. As required, we measured a value consistent with zero.

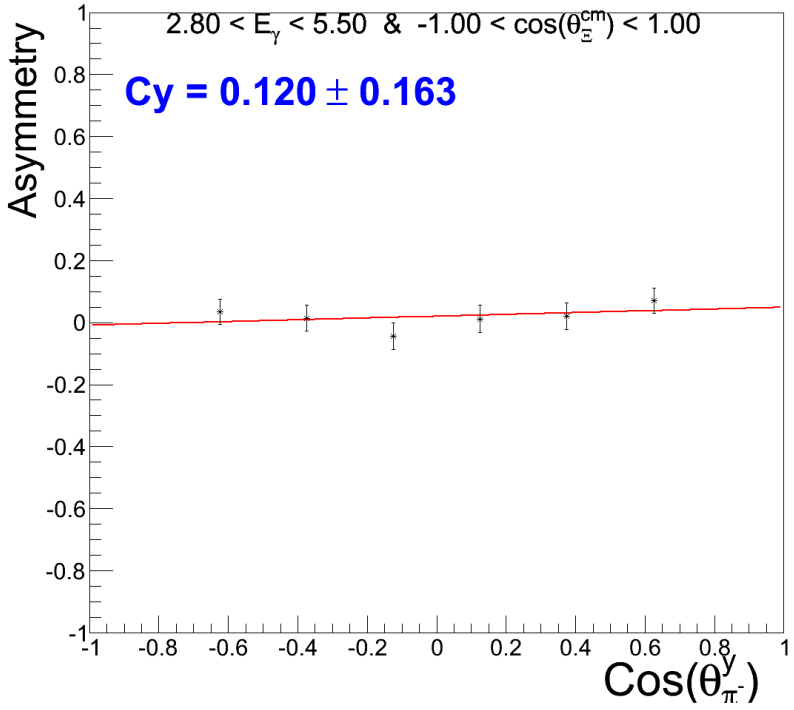


Figure 6.11: Beam-helicity asymmetry as a function of pion angle off $\hat{y}$, integrated over all bins. The linear fit is used to measure the forbidden transfered polarization $C_y$. The measurement is consistent with zero as required.

## 6.3 Comparison with Theory

Our final results were compared with theory as displayed in Figs. 6.12, 6.13, and 6.14. The theoretical predictions of Ref. [11] are based off relativistic meson-exchange of cascade production with intermediate hyperon resonances, as described in Chapter 1. The model has three variants, the first two (A and B) include all hyperon resonances

up to $\Lambda(1890)$; the first uses pure pseudoscalar coupling, while the second uses pure pseudovector coupling. The third variant of the model (C) is described in Ref. [14], which appends the hyperon resonance spectrum of Ref. [11] to include higher spin intermediate states, namely the $\Sigma(2030)$. Overall, the predicted magnitudes of polarization for all three models are in agreement with our results. A more detailed discussion is left for the following section.

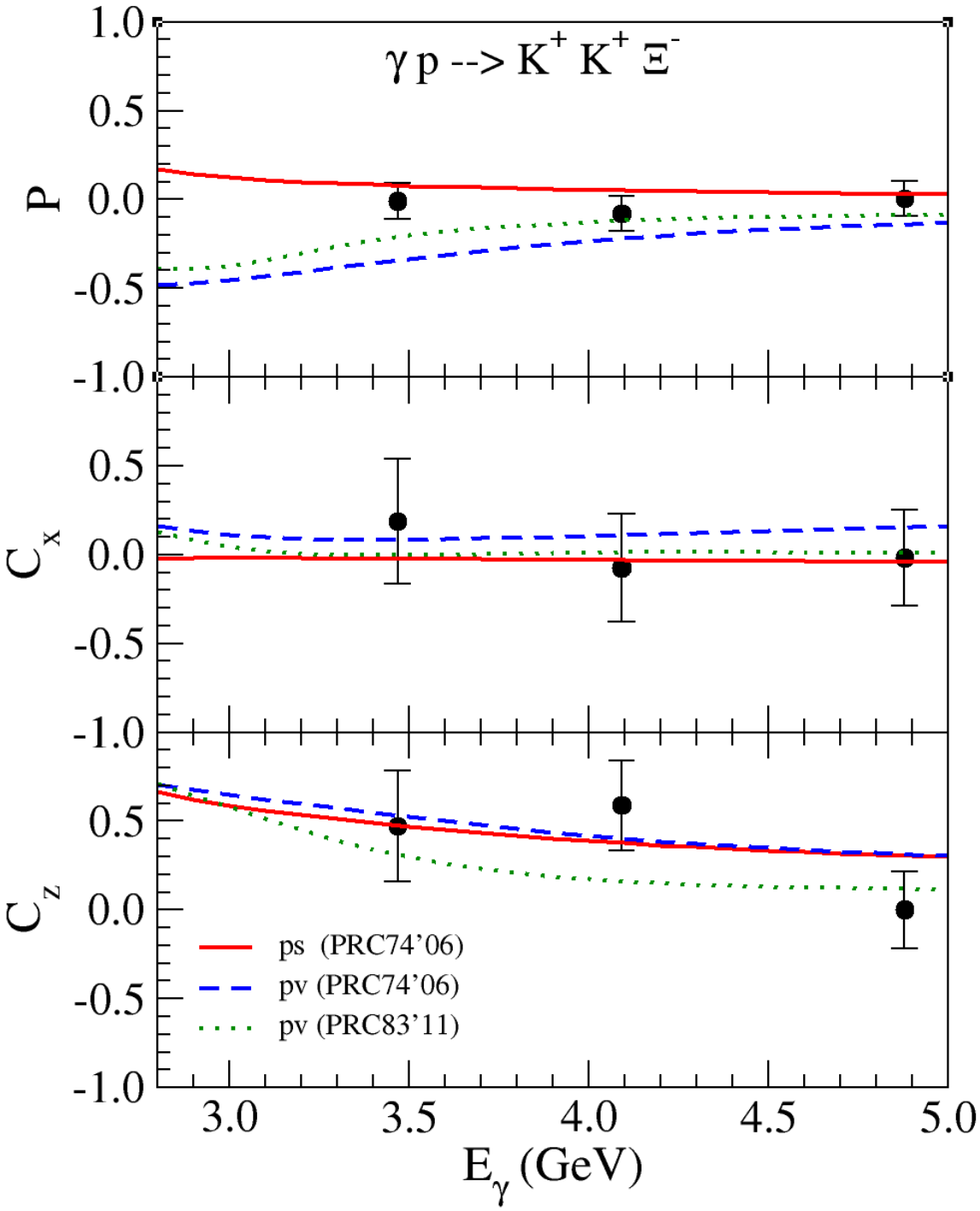


Figure 6.12: A comparison of our results with theory for $P$ (top), $C_x$ (middle) and $C_z$ (bottom) as a function of beam energy. The theoretical predictions of Ref. [11] are based on pseudoscalar (solid red) and pseudovector (striped blue) meson-exchange as described in Chapter 1. Additional high spin hyperon resonances were introduced in Ref. [14] (dotted green). Displayed results are integrated over all energy bins.

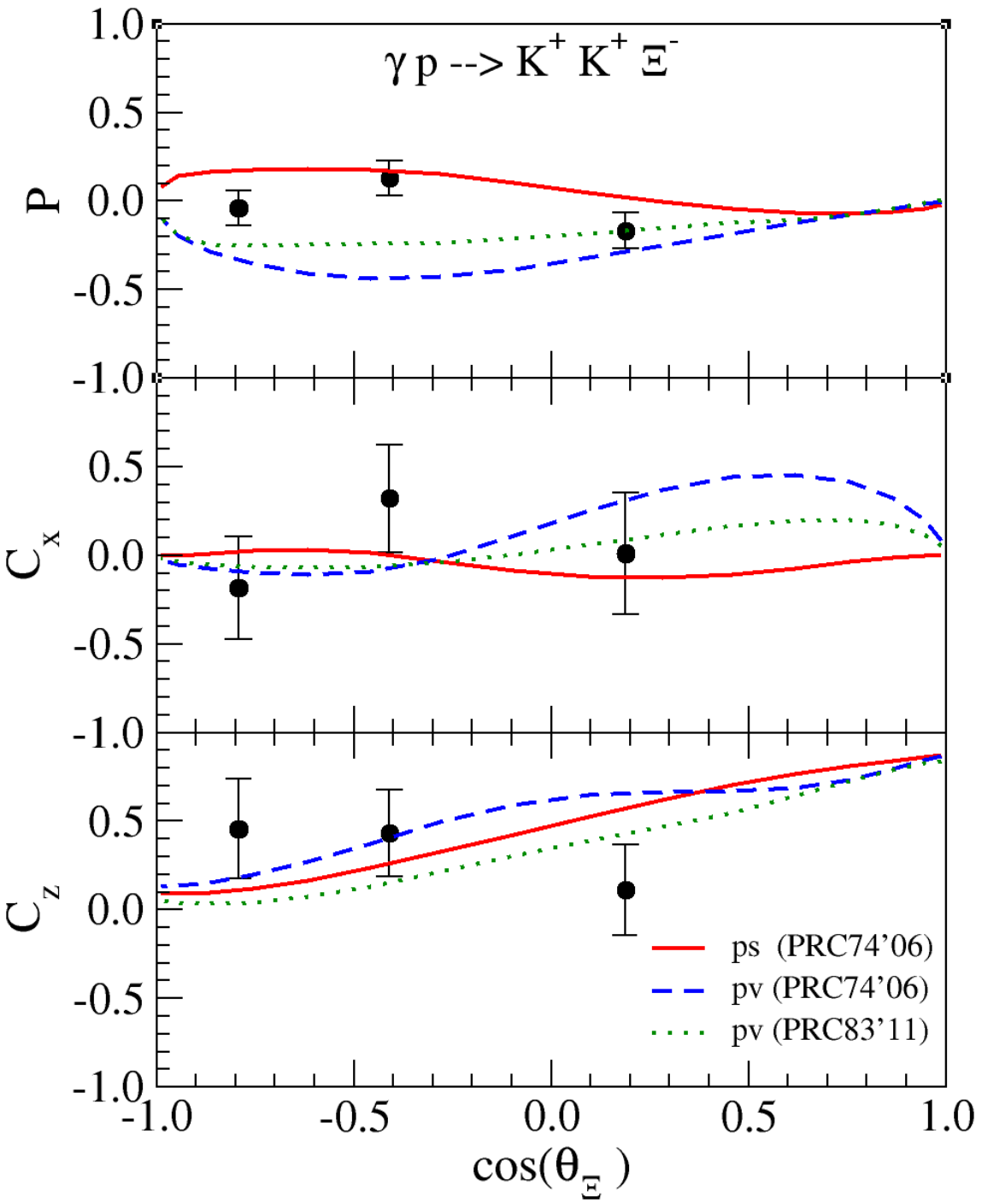


Figure 6.13: A comparison of our results with theory for $P$ (top), $C_x$ (middle) and $C_z$ (bottom) as a function of cascade angle. The theoretical predictions of [11] are based off pseudoscalar (solid red) and pseudovector (striped blue) meson-exchange in the $t$-channel as described in Chapter 1. Additional high spin hyperon resonances were introduced in Ref. [14] (dotted green). Displayed results are integrated over all cascade angles.

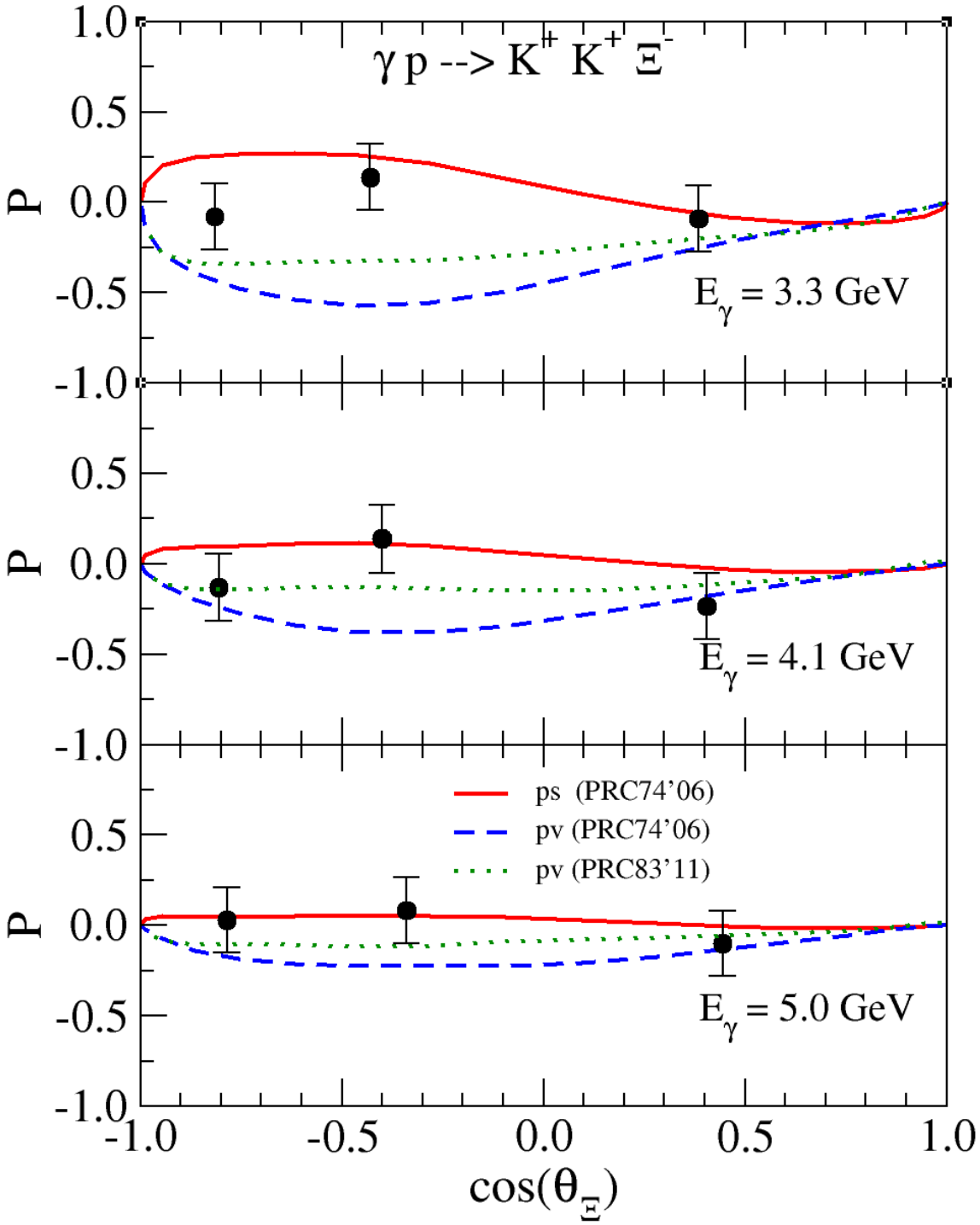


Figure 6.14: A comparison of our results with theory for $P$ in three energy bins. The theoretical predictions of [11] are based off pseudoscalar (red) and pseudovector (blue) meson-exchange in the $t$-channel as described in Chapter 1. Additional high spin hyperon resonances were introduced in Ref. [14] (green).

### 6.3.1 Comments On our Comparison with Theory

Overall, our results for all three polarization observables are in agreement with the predictions from theory. Our measured values of $P$ indicate a preference for pseudoscalar coupling (in variant A) over pseudovector coupling (in variant B), although most of the data lie somewhere between variants A and C. Additionally, Fig. 6.14 indicates the kinematic dependence of $P$ to differ from the predictions, however this may be attributed to statistical fluctuations.

Similar to $P$, the results of $C_x$ are in good agreement with the theory, although no single variant fits the data significantly better than the others. The furtherest departure from the predictions for $C_x$ is in the energy-integrated results which is shown in Fig. 6.13, again, differences are within statistical precision.

Finally, the measurement of $C_z$ is also in agreement with the theory and there is no discernible preference for any given variant. While the magnitudes are in agreement, the energy-integrated $C_z$ results as a function of cascade angle appear to depart from theory. We do not show monotonically increasing $C_z$ as cascade angles become more forward in the center-of-mass frame as predicted, however as previously mentioned, the data sample suffered from a lack of events in the forward regions. The lack of forward cascade events is mostly because of differential cross section effects. Unlike in single meson production, $C_z$ is not necessarily required by conservation of angular momentum to go to unity at extreme forward or backward cascade angles since the double meson system can carry orbital angular momentum.

The discrepancies between our results and the theory could suggest additional intermediate hyperon resonances may be present in production mechanism of our reaction. There are a number of known, high-spin hyperon resonances, the $\Lambda(2100)$ for example, that were not included in the model calculations. The overall qualitative agreement

of our results and the theory does however corroborate the small body of preexisting evidence [11, 13] for cascade production through the excitation of intermediate hyperons via relativistic meson exchange in the $t$-channel.

# Chapter 7

## Systematic Uncertainties

The systematic uncertainty of a measurement $M$ can be estimated by,

$$\delta_{sys}(M) = |M - M_{alt}|, \tag{7.1}$$

where $M_{alt}$ is the outcome after an aspect of the measurement has been varied appropriately. We would however expect, even in the absence of systematic uncertainty, to have statistical fluctuations associated with repeated measurements. Care should be taken to *separate* the statistical fluctuations from the systematic uncertainty, as to avoid overestimating the latter.

However, our data do not have the statistical precision needed to accurately estimate the systematic uncertainty; all observed fluctuations were well within the statistical uncertainty. We instead chose to "over estimate" the systematic uncertainty by not performing a separation.

In general, the total systematic uncertainty of a measurement comes from many sources. Let the uncertainty arising from a *single source* be denoted by $\delta_s(M)$. If the true correlation between each source of uncertainty is not known, as it is often the case, it is safest to over estimate by assuming zero-correlation and adding in quadrature,

$$\delta_{sys}(M) = \sqrt{\sum_s (\delta_s(M))^2}. \tag{7.2}$$

The sources of systematic uncertainty were individually studied and summarized in Table. 7.1.

| | $\delta(P)$ | $\delta(C_x)$ | $\delta(C_z)$ |
|---|---|---|---|
| $\alpha$ | negligible | negligible | 0.009 |
| $P_\odot$ | N/A | negligible | 0.008 |
| Binning | negligible | 0.105 | 0.037 |
| Mass | 0.021 | 0.067 | 0.019 |
| Fiducial | 0.008 | 0.005 | 0.048 |
| Acceptance | 0.018 | 0.005 | 0.020 |
| **Total systematic** | 0.029 | 0.124 | 0.067 |
| **Statistical** | 0.061 | 0.177 | 0.145 |
| **Total uncertainty** | 0.067 | 0.216 | 0.159 |

Table 7.1: Systematic uncertainty for $Cx, Cz$ and $P$ arising from various sources. All sources are detailed in the present chapter. A summary: Binning refers to width of the binning used, Mass refers to the width of the mass cuts, Fiducial refers to fiducial cuts, Acceptance refers to acceptance effects. Total systemic refers to each source, added in quadrature and Statistical refers to the known statistical uncertainty associated with the nominal measurement. Finally, Total uncertainty refers to the total systematic and statistical uncertainties added in quadrature.

We found that the statistical uncertainty far outweighed the systematic uncertainty, which, due to our low statistics was anticipated. Note that if separation of statistical uncertainty was performed, the systematic uncertainties would contribute virtually nothing and would appear to be inconsequential to our measured spin observables.

The remainder of the present chapter shows and discusses how the individual sources of uncertainty were computed.

## 7.1 Uncertainty in Analyzing Power and Beam Polarization

We calculated that the limited precision of the analyzing power contributed an uncertainty of 2.6% for our results, giving $\delta_\alpha(P) = 0.0007 \approx 0$, $\delta_\alpha(C_x) = 0.0005 \approx 0$, and $\delta_\alpha(C_z) = 0.0081$, for the integrated results. The limited photon-beam polarization precision gave 3% error, yielding $\delta_{P_\odot}(C_x) = 0.0005 \approx 0$ and $\delta_{P_\odot}(C_z) = 0.009$. The calculations of the relative uncertainties are outlined below.

### 7.1.1 Analyzing Power

From Equation 3.43, we find the uncertainty in $C_x$ and $C_z$ due to the uncertainty in $\delta\alpha = 0.012$ [3] to be,

$$\delta_\alpha(C_i) = |\delta\alpha \frac{\partial}{\partial\alpha} \frac{A(\cos\theta_\pi^{\hat{i}})}{|P_\odot|\alpha\cos(\theta_\pi^{\hat{i}})}| = |C_i \frac{\delta\alpha}{\alpha}| = |C_i|0.026, \tag{7.3}$$

which is 2.6% relative error. Similarly for $P$, Equation 3.38 gives,

$$\delta_\alpha(P) = |P\frac{\delta\alpha}{\alpha}| = |P|0.026. \tag{7.4}$$

### 7.1.2 Beam Polarization

The uncertainty in the electron beam polarization largely came from the Moller measurements which were recorded with a precision close to 1.5%. To additionally account for uncertainty in the photon-beam energy spectrum, we take the uncertainty in the photon-beam polarization to be 3%. This translates into,

$$\delta_{P_\odot}(C_i) = |C_i|0.03. \tag{7.5}$$

## 7.2 Binning of Pion Angle in Beam-Helicity Asymmetry

The observables were found to vary when the binning scheme of the pion angle was altered. Figures 7.1 and 7.2 show the measured values of $C_x$ and $C_z$ respectively, with decreasing bin width from left to right. The average deviation from the nominal measurements gives $\delta_{bin}(C_x) = 0.105$, $\delta_{bin}(C_z) = 0.037$.

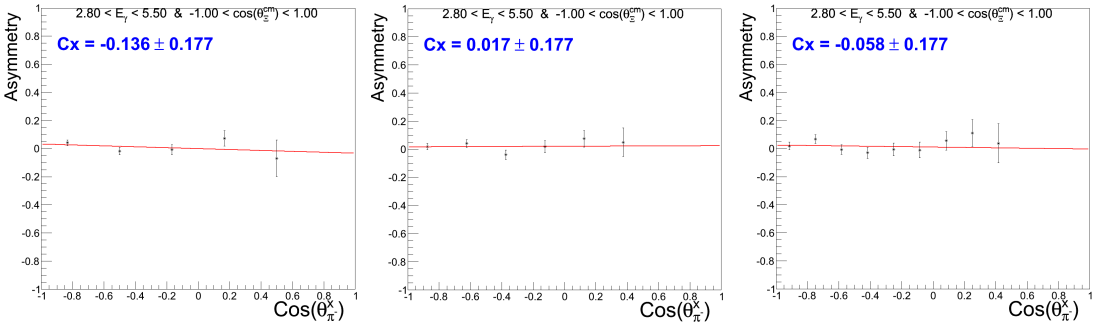


Figure 7.1: Shows the asymmetry as a function of pion angle off the $x$-axis and the corresponding $C_x$ measurement for decreasing pion bin width from left to right. The nominal binning scheme is shown in the middle plot.

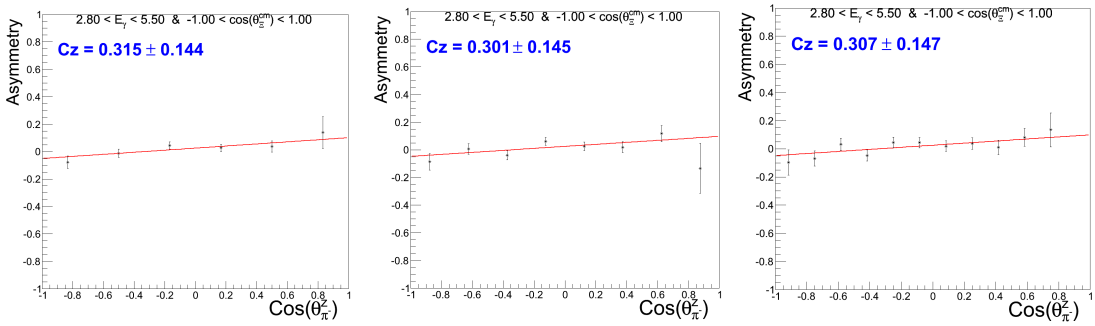


Figure 7.2: Shows the asymmetry as a function of pion angle off the $z$-axis and the corresponding $C_z$ measurement for decreasing pion bin width from left to right. The nominal binning scheme is shown in the middle plot.

## 7.3 Varying the Mass-Hypersphere Radius

One way to estimate the systematics introduced by possible background contamination is to vary the radius for the hypersphere cut. By increasing or decreasing the radius, we let in more or less events from the *sideband*. Fig. 7.3 shows the cascade signal with multiple layers of radius cuts in the hypersphere, while Figs. 7.4, 7.5 and 7.6 show the effects on observables for differing cuts. The average deviation from the nominal measurements gives $\delta_{mass}(P) = 0.021$ , $\delta_{mass}(C_x) = 0.067$ and $\delta_{mass}(C_z) = 0.019$.

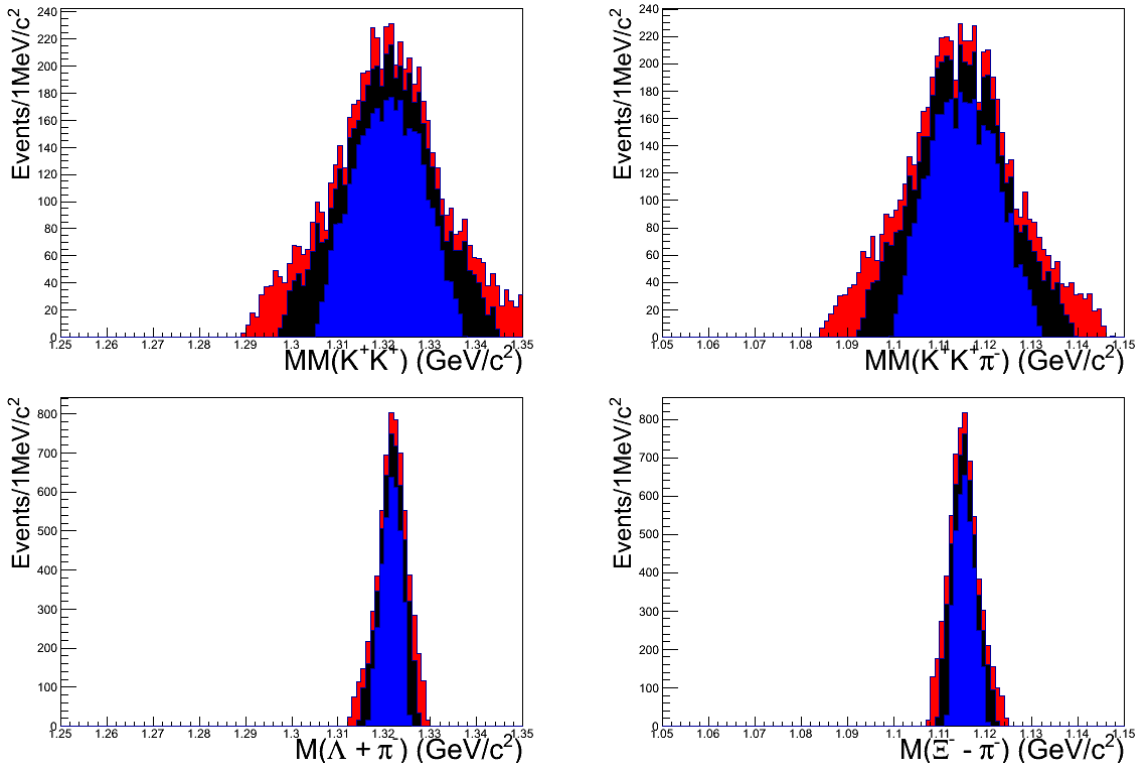


Figure 7.3: The signal shown with 2,3 and 4 $\sigma$ cuts (or radius cuts in the hypersphere). The nominal 3-sigma cut is shown in black.

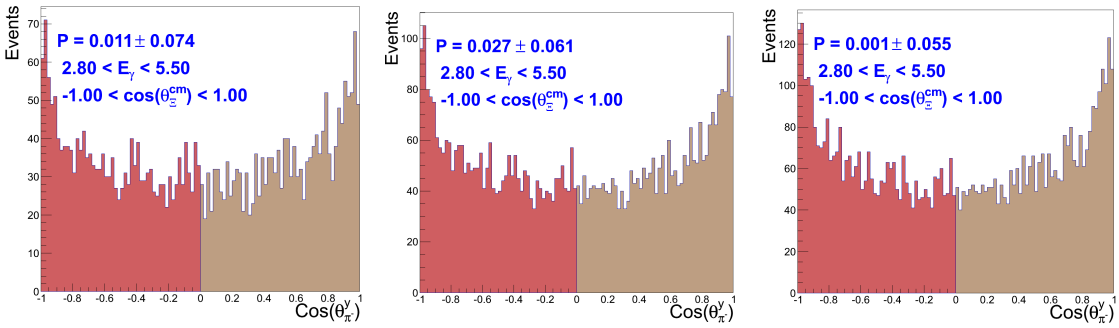


Figure 7.4: The integrated $P$ results for 2,3 and 4 sigma cuts from left to right respectively

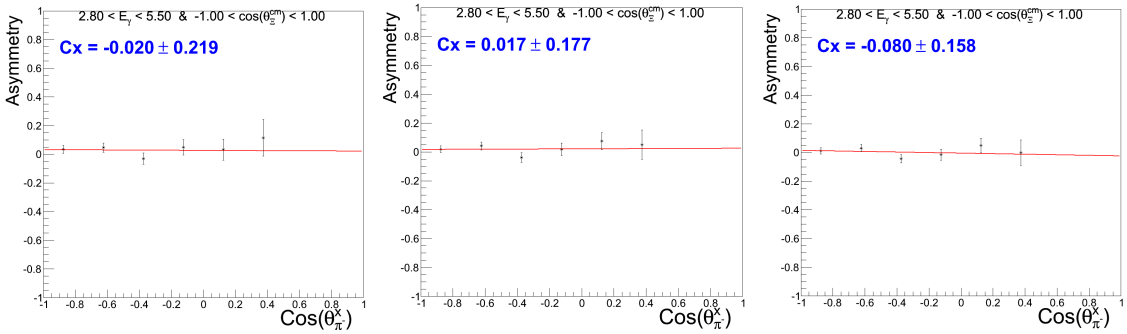


Figure 7.5: The integrated $C_x$ results for 2,3 and 4 sigma cuts from left to right respectively

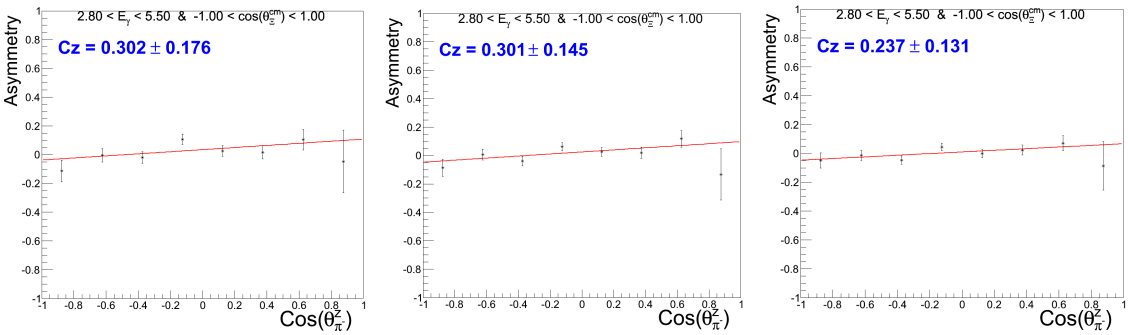


Figure 7.6: The integrated $C_z$ results for 2,3 and 4 sigma cuts from left to right respectively

## 7.4 Effect of Fiducial Cuts

The effects of the fiducial cuts which are described in Chapter 4 were observed to have a small effect on our results. Figures 7.7, 7.8 and 7.9 show a comparison of results without fiducial cuts and with "loose" fiducial cuts. The deviation from two measurements gives $\delta_{fid}(P) = 0.008$ $\delta_{fid}(C_x) = 0.005$ and $\delta_{fid}(C_z) = 0.048$.

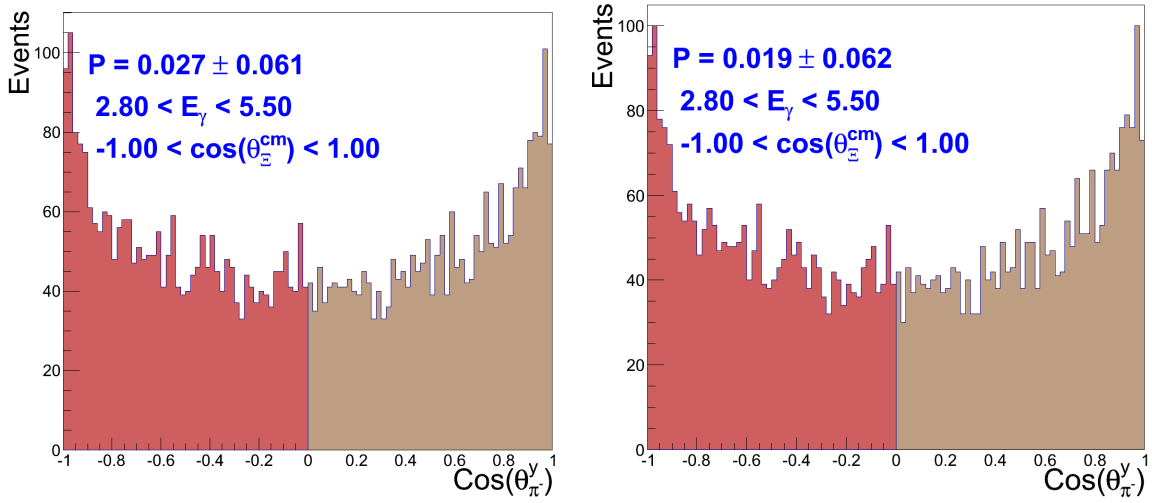


Figure 7.7: $P$. Left: results with no fiducial cuts. Right: results with loose fiducial cuts.

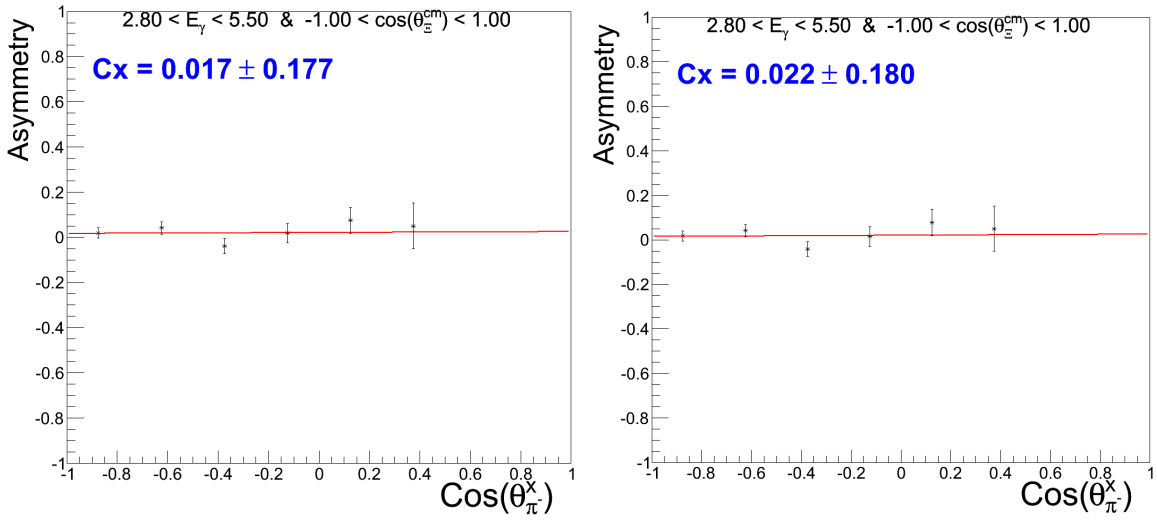


Figure 7.8: $C_x$. Left: results with no fiducial cuts. Right: results with loose fiducial cuts.

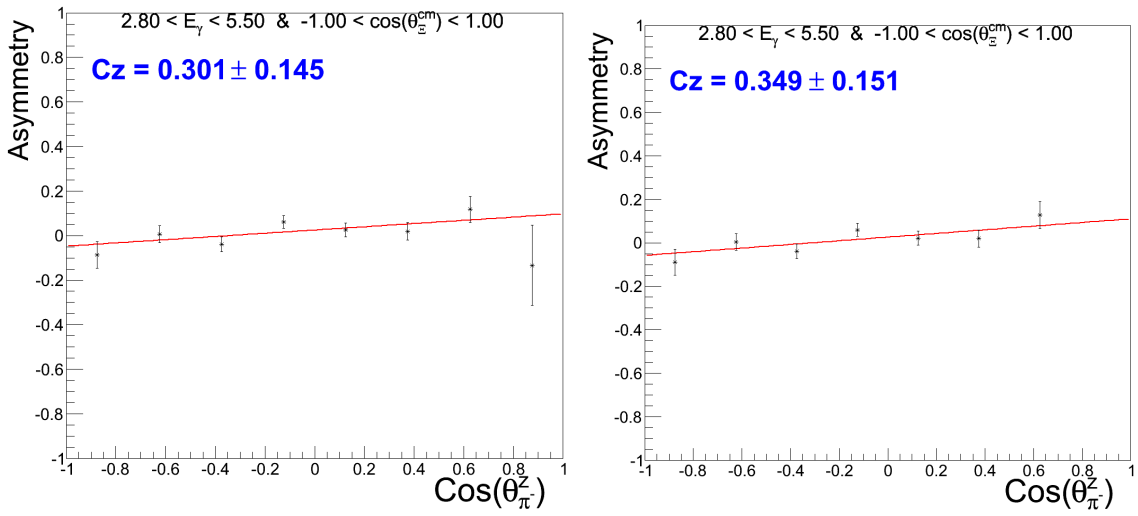


Figure 7.9: $C_z$. Left: results with no fiducial cuts. Right: results with loose fiducial cuts.

## 7.5 Non-Cancellation of Acceptance for $P$

The bin averaged deviation of $P$ as calculated from the uncorrected forward-backward pion asymmetry and the acceptance-corrected forward-backward pion asymmetry gives, $\delta_{ac}(P) = 0.018$. Each deviation was taken as the difference of values between what is shown in Figs. 6.2 and 6.3 for each respective bin, then averaged. Note that averaging $\delta_{ac}(P)$ over multiple bins inflates statistical fluctuation and thus overestimates the associated uncertainty. We chose to overestimate, to demonstrate the slightness of acceptance's effect on our results.

## 7.6 Study of Non-Cancellation of Acceptance for Cx and Cz

[H] The calculation of $C_x$ and $C_z$ was based on the fact that, to first order, the acceptance of the detector cancels in the asymmetry. All second order non-cancellation comes from helicity dependent kinematic distributions of the detected particles.

In the $\gamma p \to K^+K^+\Xi^-$ reaction, both kaons come either from the decay of excited baryons ($Y^*$) or through other parity-conserving strong or electromagnetic interactions. Thus all kinematic distributions for the kaons are independent of the photon-

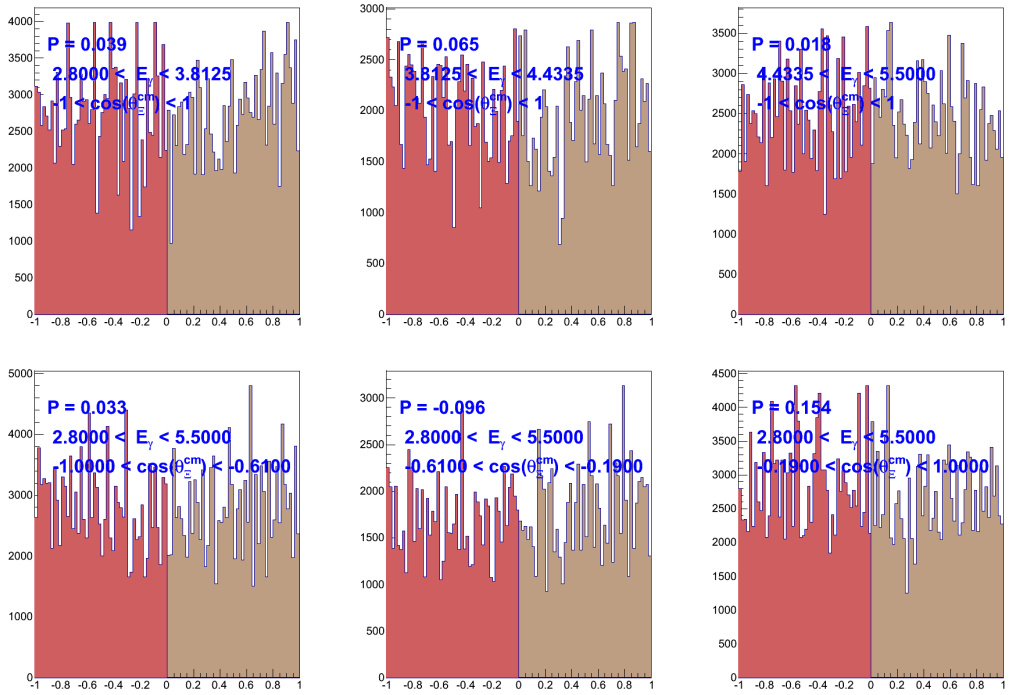


Figure 7.10: The acceptance corrected forward-backward pion asymmetry results for $P$ in three energy bins and three center-of-mass cascade angle bins.

beam helicity. The only helicity dependent parts of the reaction are those following a weak decay of ground-state hyperons. The pion, in the decay $\Xi^- \to \Lambda\pi^-$, contributes to non-cancellation of acceptance. However, only the projections of the pion angular distribution off $\hat{x}$ and $\hat{z}$ are photon-helicity-dependent since the photon-helicity can not be transfered to the $\Xi^-$ in the $y$-direction.

The measurement of the spin observables from Monte Carlo events were found to deviate linearly according to

$$\delta_{acc}(C_i) = \sum_{j=x}^{z} C_j E_{ij}, \tag{7.6}$$

where $E_{ij}$ is an error matrix that was computed using Monte Carlo events and $i$ takes on values of $x$ or $z$. The elements of the 2x2 matrix $E_{ij}$ were estimated by simulating events with an effective cascade polarization in the $\hat{x}$ and $\hat{z}$ directions (corresponding

to $C_x^{gen}$ and $C_z^{gen}$ ) then determining the deviation between generated and measured ($C_x^{rec}$,$C_z^{rec}$) values after reconstruction.

As shown in Fig. 7.11, the values $C_x^{gen} = 0.5, C_z^{gen} = 0$ were generated corresponding to measured values of $C_x^{rec} = 0.483, C_z^{rec} = 0.098$ yielding $E_{xx} = 2(0.017) = 0.34$ and $E_{xz} = 2(-0.002) = -0.004$. Similarly, as shown in Fig. 7.12, the values $C_x^{gen} = 0, C_z^{gen} = 0.5$ were generated corresponding to measured values of $C_x^{rec} = 0.116, C_z^{rec} = 0.461$ yielding $E_{zx} = 2(-0.116) = -0.232$ and $E_{zz} = 2(0.039) = 0.079$. The error matrix is given by,

$$E_{ij} = \begin{pmatrix} 0.34 & -0.004 \\ -0.232 & 0.079 \end{pmatrix} \tag{7.7}$$

Applying the error matrix on our measured spin observables from the data $C_x = 0.017$ and $C_z = 0.301$ gives,

$$\delta_{acc}(C_x) = 0.017E_{xx} + 0.301E_{xz} = 0.0057 - 0.0012 = 0.0045 \approx 0.005, \tag{7.8}$$

$$\delta_{acc}(C_z) = 0.017E_{zx} + 0.301E_{zz} = -0.0039 + 0.0238 = 0.0199 \approx 0.02. \tag{7.9}$$

Although we found the second order acceptance effects to be asymmetrical, they were taken in as typical symmetric systematic uncertainties.

## 7.7 Effect of Method for $P$: A Cross Check

The bin averaged deviation of $P$ as calculated from the fitted acceptance-corrected and uncorrected forward-backward pion asymmetries gives, $\delta_{method}(P) = 0.068$. Each deviation was taken as the difference between values in Figs. 6.2 and 6.5, for each respective bin. Fitting the acceptance corrected angular distribution is inherently less reliable than the forward-backward asymmetry method. A reliable measure of systematic uncertainty introduced by acceptance effects is calculated in Section 7.5.

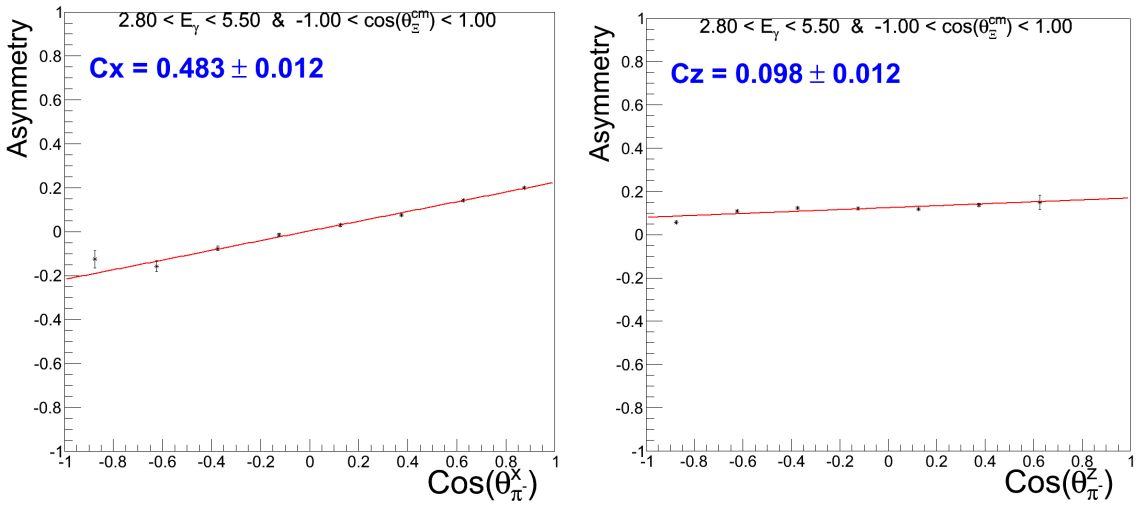


Figure 7.11: The reconstructed values of $C_x^{rec}$ (left) and $C_z^{rec}$ (right) with a generated value $C_x^{gen} = 0.5$ and $C_z^{gen} = 0$.

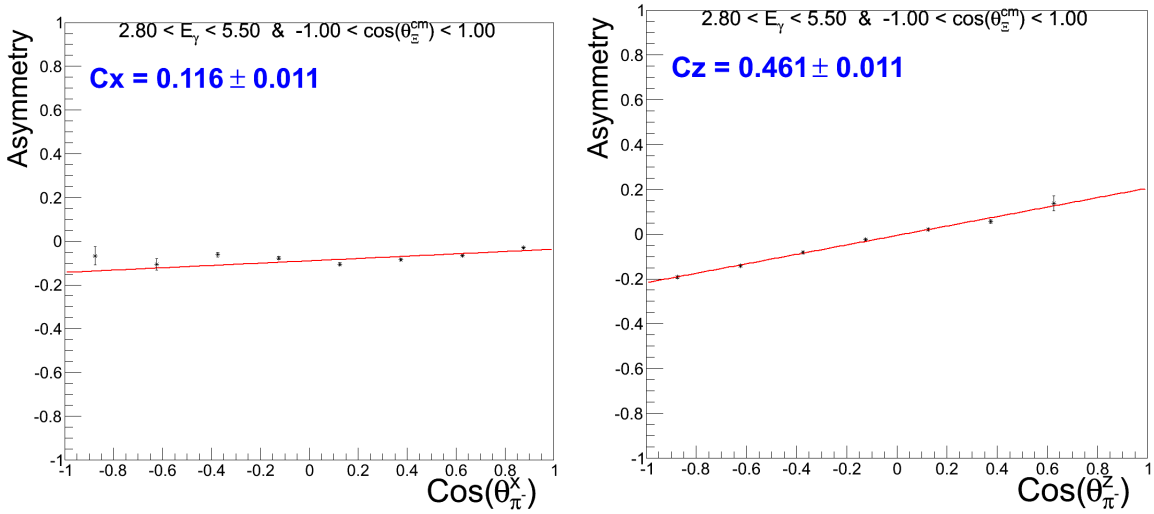


Figure 7.12: The reconstructed values of $C_x^{rec}$ (left) and $C_z^{rec}$ (right) with a generated value $C_x^{gen} = 0$ and $C_z^{gen} = 0.5$.

### 7.7.1 Fitting vs Raw Yield: A Cross Check on $C_x$ and $C_z$

Another way to quantify the effects of background contamination is to compare results which required no fitting method due to the absence of background, with results derived from a background-subtracted fitting algorithm. The background was heavily reintroduced by relaxing two of our four mass constraints, analogously going from a cut in the hypersphere to a cut in the circle. Fig. 7.13 is an example of a typical fit which was integrated to give a background-subtracted yield. The results derived from the fitting algorithm were compared with "background free" results in Figs. 7.14 and 7.15. The average deviation of the two measurements give $\delta_{yeild}(C_x) = 0.046$ and $\delta_{yeild}(C_z) = 0.009$, both within statistical uncertainty. The comparison between fitting and raw yield serves only as a cross check. A more reliable measure of systematic uncertainty introduced by background is calculated in Section 7.3.

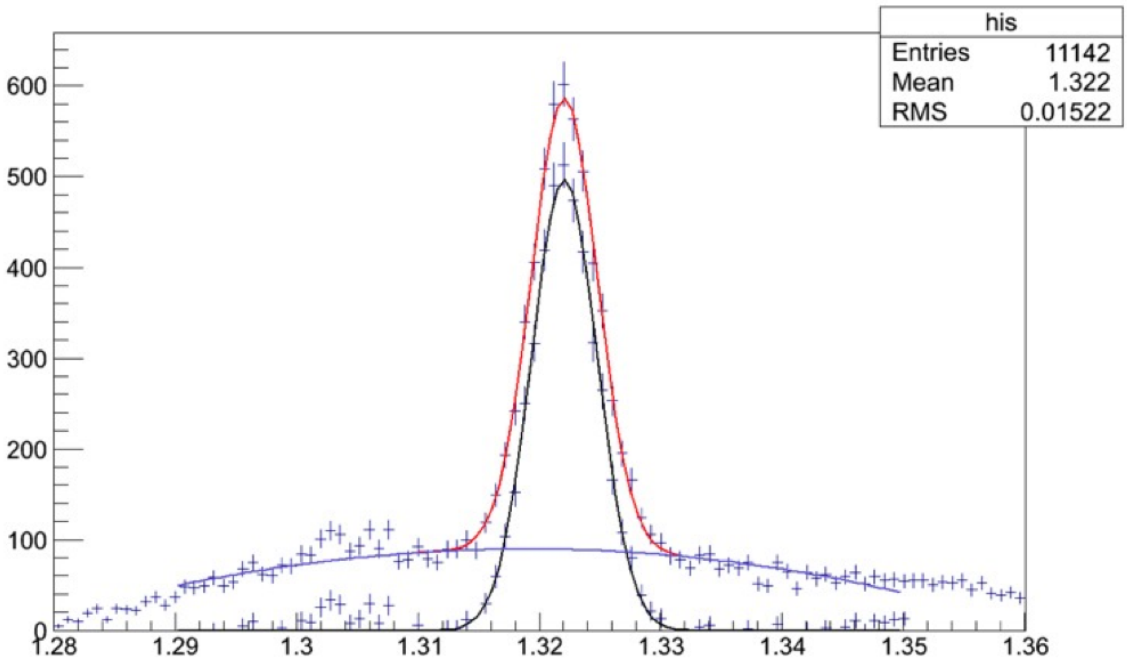


Figure 7.13: A typical fit which was integrated to give a background subtracted yield.

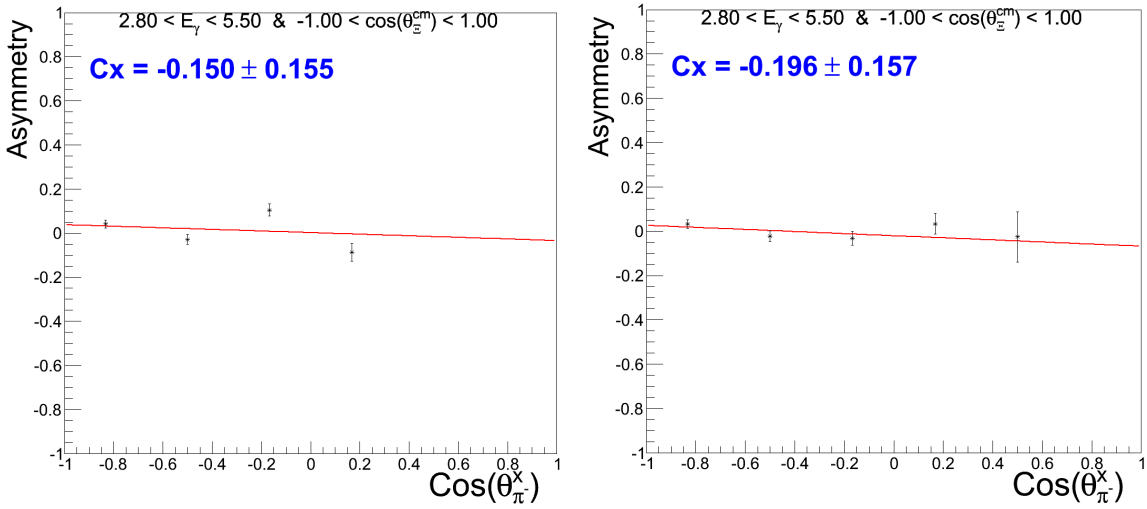


Figure 7.14: Left: fitting with four pion bins. Right: no fitting with five pion bins. The binning scheme for the fitting method was defined coarsely to provide reliable yields.

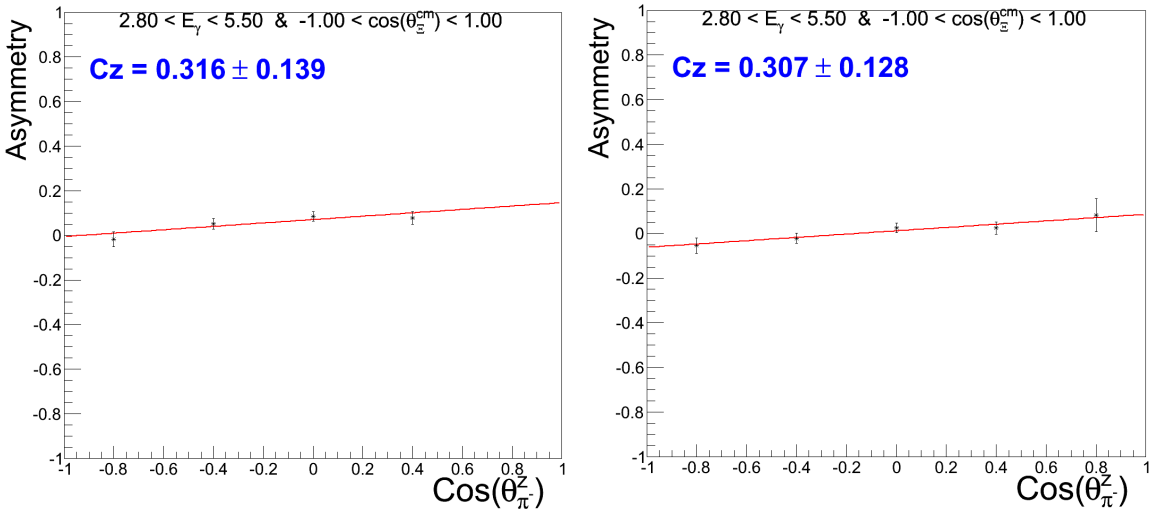


Figure 7.15: Left: fitting with four pion bins. Right: no fitting with five pion bins. The binning scheme for the fitting method was defined coarsely to provide reliable yields.

## 7.8 Studies on Background: Further Cross Checks

### 7.8.1 Effective Polarization of Background From Lambda Decay

Although the data were found to be mostly background free, the primary source would likely come from contamination as a result of the $\Lambda$ decay $\Lambda \to p\pi^-$. In this scenario, the pion from the $\Lambda$ could be misidentified as coming from the cascade decay. This "$\Lambda$ background" is shown Fig. 7.16 and was estimated at most to constitute a few percent of the signal. For the background to contribute significantly to the systematic uncertainty, it's measured effective polarization would have to be well over 100% (possible since the effective values do not correspond to physical observables) due to its minute presence. The effective polarization of the $\Lambda$ background was measured for the sum of all kinematic bins and shown in Fig. 7.17. We found a statistically significant "effective" polarization of $C_z = -0.625$, which would contaminate our data sample by less than 1%, thus, $\delta_\Lambda(C_z) \approx -0.006$. In any case, the varying hypersphere cut includes this number so $\delta_\Lambda(C_z)$ was not taken as a separate source of systematic uncertainty. The analysis on the $\Lambda$-pion background serves merely as a cross check of previous systematics.

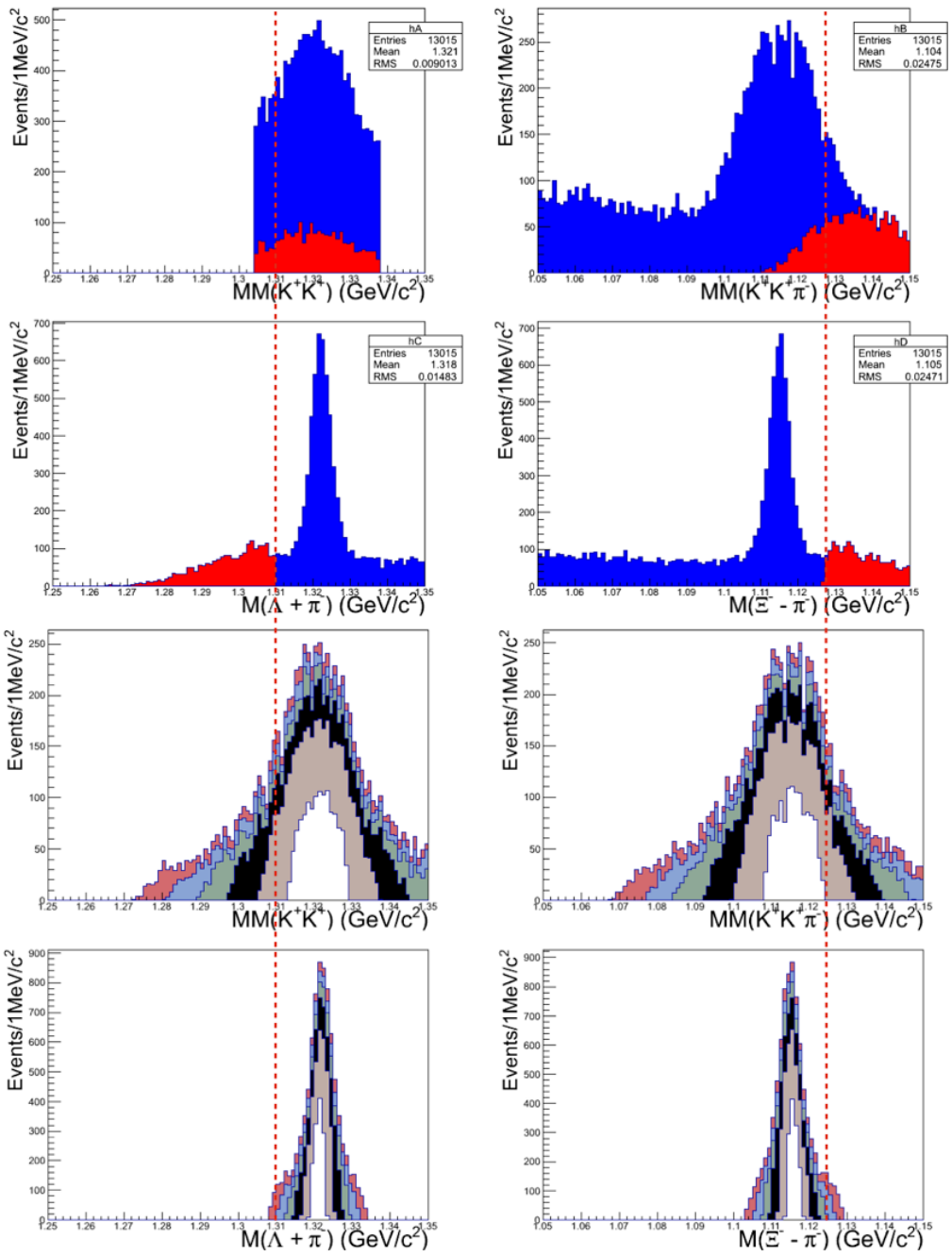


Figure 7.16: In the top four plots: events in red are the result of cut on the invariant mass $m(\Lambda + \pi^-)$ and $m(\Xi^- - \pi^-)$ which identifies the pion coming from the $\Lambda$ decay. Its presence is shown over the broader spectrum of events. In the bottom four plots: Events representing cuts in the hypersphere radius $r = 1, 2, 3, 4, 5, 6$ are layered over one another. The vertical lines provide a means of showing how deep within the hypersphere the "lambda-pion" cuts are. One should note the $\Lambda$-pion cuts lie in the $r = 6$ hypersphere, far out in the sideband of the primary signal.

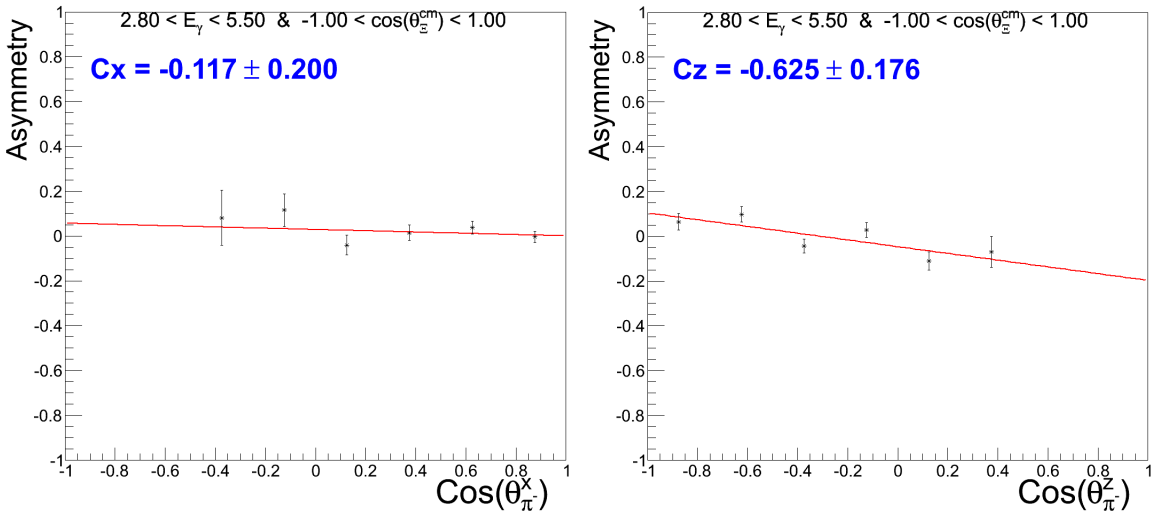


Figure 7.17: Measurements of the *effective* $C_x$ and $C_z$ for events in the lambda-pion background. This measurement is not meaningful in terms of polarization observables, but serves as study of background effects.

### 7.8.2 Effective Polarization of Unknown Background

Just as the Λ-pion contamination was examined, a similar study can be done for the background that comprises a mix of unknown sources. This "unknown" or "mixed" background is mostly from particle misidentification and is shown Fig. 7.18. The mixed background was found to have a zero effective polarization. If there was a large presence of mixed background in our signal, it would dilute the measured polarization. The varying of the hypersphere cuts include the small dilution effect so a separate systematic uncertainty need not be introduced. The systematic uncertainty associated with the discrepancy of results deriving from background-subtraction and non-background subtraction yield method also accounts for this the mixed background.

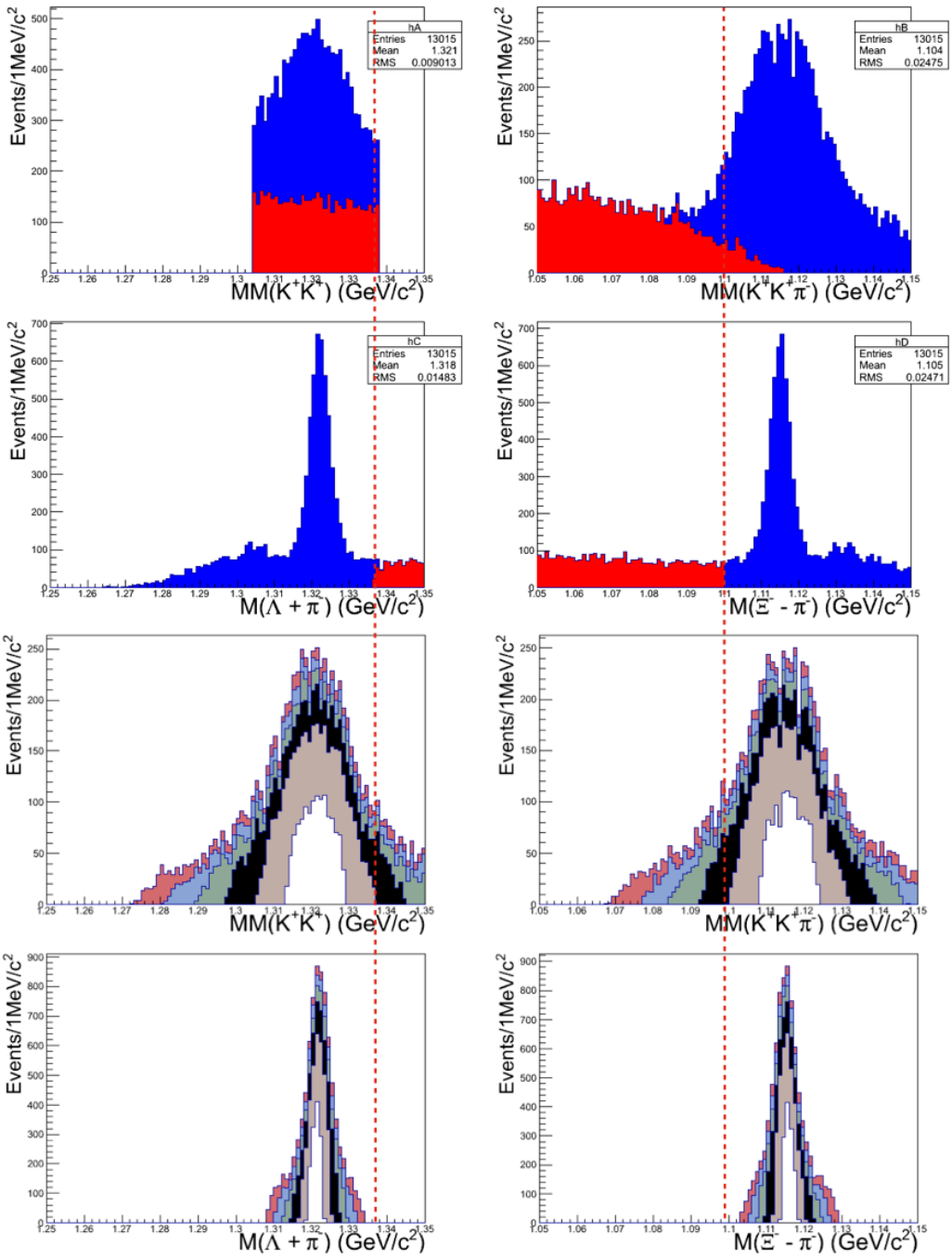


Figure 7.18: In the top four plots: events in red are the result of cut on the invariant mass $m(\Lambda + \pi^-)$ and $m(\Xi^- - \pi^-)$ which identifies the "mixed" background. Its presence is shown over the broader spectrum of events. In the bottom four plots: Events representing cuts in the hypersphere radius $r = 1, 2, 3, 4, 5, 6$ are layered over one another. The vertical lines provide a means of showing how deep within the hypersphere the mixed-background cuts are.

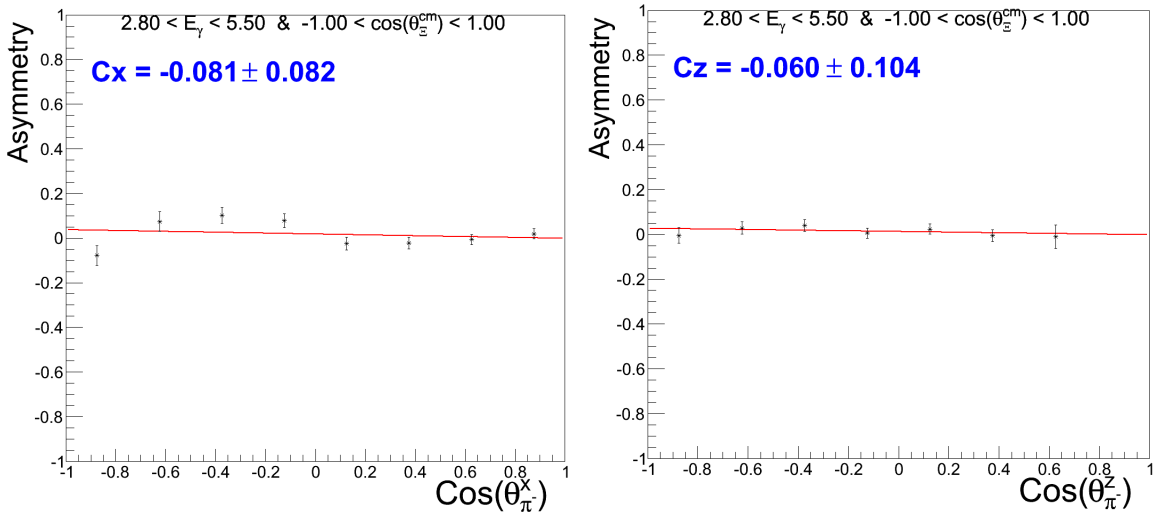


Figure 7.19: Measurements of the *effective* $C_x$ and $C_z$ for events in the "mixed" background. This measurement is not meaningful in terms of polarization observables, but serves as study of background effects.

# Chapter 8

# Conclusions and Outlook

This work presents the first ever determination of polarization observables for the charged cascade hyperon in the reaction $\gamma p \to K^+K^+\Xi^-$. We utilized the parity-violating weak decay of the cascade as a means to measure its polarization through the angular distribution of its decay products. A background-free sample of over 5000 $\Xi^- \to \Lambda\pi^-$ events composed the data, a globally unprecedented yield for photoproduction. We measured the induced polarization $P$, along with the degree of polarization transfer from a circularly polarized photon beam, $C_x$ and $C_z$.

Overall the induced polarization $P$, along with transferred polarization $C_x$ and $C_z$, were found to agree with predictions from the only known model of cascade photoproduction. The theory models hadronic interactions based on relativistic meson exchange, with cascade production arising due to the excitation and decay of resonant, singly strange hyperons. Among the included diagrams, the ones involving $t$-channel kaon exchange dominate the overall contributions to production, which reproduces the preexisting data on the cascade cross sections. A model including singly strange intermediate hyperons for the $\gamma p \to K^+K^+\Xi^-$ reaction is a natural choice, because otherwise, it would involve a $t$-channel exchange of exotic mesons with S=2.

Our results for $P$, which due to the nature of our measurement technique allowed for finer binning than for $C_x$ and $C_z$, showed the closest agreement with the theory. We found that the best match for $P$ came from the model parameterization that only took pseudoscalar mesons as candidates for exchange particles. However within uncertainty, our findings are also consistent with zero, not far from agreement with the other two variants of the model. More data at lower energies, especially closer to

threshold, will help paint a descriptive picture and provide more stringent constraints. There were no events detected below 2.8 GeV while threshold is around 2.37 GeV. The lack of data below 3 GeV is mostly due to small cross sections, as was anticipated from the known form of the differential cross section. The acceptance corrected beam energy profile in our data also indicates the cross section drops off rapidly below 3 GeV. Additionally, the detector efficiency falls off at energies approaching threshold.

Although our results were broadly in agreement with theory, there were also some interesting discrepancies. The most prominent disagreement was in $C_z$ as a function of center-of-mass cascade angle; the general trend of our results appears to diverge from theory. Before a definitive conclusion can be drawn on this front, more data need to be obtained in the forward region. The non-rising $C_z$ for forward cascade angles is a feature of our data that is permissible by angular momentum conservation for two-meson production, in contrast with the case of single meson production. We are eager to compare this feature of our results with future high statistics measurements made by CLAS12.

As expected, we found the total polarization magnitude for the cascade was much lower than what has been reported for the $\Lambda$. The integrated results show $\bar{R}_{\Xi} \approx 30\%$, while for the lambda, $\bar{R}_{\Lambda} \approx 100\%$. An interesting similarity between the lambda and cascade is that most of their total polarization comes from $C_z$, *i.e*, $R \approx C_z$ in most bins. We qualitatively explain both features of our results invoking a vector meson dominance picture in which one of the strange quarks in the final state cascade comes from the photon, and the other, from the decay of an intermediate hyperon resonance. A similar picture has been suggested to explain the previous lambda polarization data for photoproduction.

If the naive diquark model is an accurate picture for the internal dynamics of the cascade, then its total spin would largely be due to the down-quark. In this picture,

photoproduction of the cascade off a proton target should exhibit large polarization transfer from the target, from which the polarizing down-quark is inherited, but one would see little transfer from the beam. The non-zero values we observed for $C_z$ are thus in disagreement with this picture. We point out that it is perhaps unnatural to suppose that the two $s$ quarks strongly correlate as a diquark since this state is not overall antisymmetric in spin, flavor, and color. Regardless, future experiments with target polarization could prove invaluable for probing the spin structure of the cascade.

In addition to constraining current and future theoretical production models, our results taken in conjunction with subsequent polarized target experiments will facilitate progress towards a *complete measurement* for the $\gamma p \to K^+K^+\Xi^-$ reaction. Complete measurements for cascade photoproduction would allow for unambiguous calculation of amplitudes i.e. a model independent identification of any missing hyperon resonances. While the realization of a complete measurement is still infeasible with current nuclear physics instrumentation, there is much to be learned along the way, and polarization observables provide detailed information on the interference of the production amplitudes. Many $\Lambda$ and $\Sigma$ resonances have been observed and studied, but there are still large gaps to close in the world database regarding the spectrum of possible hyperon states and their properties.

For the near future, it should be possible to make a first time measurement of the beam asymmetry $\Sigma$ using our data, provided the experimental photon helicity asymmetry can be accurately accounted for. Additionally, there are other cascade polarization observables, specific to two meson production that we plan on extracting. Within the next few years, CLAS12 may be able to produce and reconstruct around a million $\Xi^- \to \Lambda\pi^-$ events.

To conclude, this work has produced the only three standing measurements for the cascade polarization observables in photoproduction. We have a qualitative understanding of our results from the vector meson dominance picture of the photon. Additionally, our data have corroborated the only theoretical model for cascade photoproduction and provided constraints for its parameters, and for the parameters of future models. We have taken a first step towards a characterization of the cascade's underlying complex amplitudes of production. Such amplitudes, which can in principal be extracted from cross section and polarization and observables such as the three we have provided, will help elucidate the spectrum of excited hyperon resonances. Finally, our work has established the feasibility of cascade studies near threshold energies. There is still much to be learned from further studies of this data set and in cascade data sets to come, in particular with CLAS12. We hope our results will stimulate the otherwise slow progress in experimental and theoretical cascade physics, and in turn help bring about a phenomenological understanding of the photoproduction of strangeness.

# Bibliography


[1] D.H. Perkins. *Introduction to High Energy Physics*. Cambridge University Press, 2000.

[2] NOVA PBS. http://www.pbs.org/wgbh/nova.

[3] K. Nakamura *et al.* (Particle Data Group). Review of Particle Physics. *Journal of Physics G*, 33, 2006.

[4] S.S.M. Wong. *Introductory Nuclear Physics*. A Wiley-Interscience publication. Wiley, 1998.

[5] F. Halzen and A.D. Martin. *QUARK & LEPTONS: AN INTRODUCTORY COURSE IN MODERN PARTICLE PHYSICS*. Wiley India Pvt. Limited, 2008.

[6] M. Gell-Mann and Y. Ne'eman. *The eightfold way: a review, with a collection of reprints*. Frontiers in physics. W.A. Benjamin, 1964.

[7] Barth *et al.* Evidence for the positive-strangeness pentaquark $\Theta^+$ in photoproduction with the SAPHIR detector at ELSA. *Physics Letters B*, 572(3-4):127–132.

[8] S. Stepanyan *et al.* Observation of an Exotic $S = +1$ Baryon in Exclusive Photoproduction from the Deuteron. *Phys. Rev. Lett.*, 91:252001, Dec 2003.

[9] T. Nakano and N. *et al* Muramatsu. Evidence for the $\Theta^+$ in the $\gamma d \to K^+K^-pn$ Reaction by Detecting $K^+K^-$ Pairs. *Phys. Rev. C*, 79:025210, Feb 2009.

[10] Eric Swanson. New particle hints at four-quark matter. *Physics*, 6:69, Jun 2013.

[11] K. Nakayama, Yongseok Oh, and H. Haberzettl. Photoproduction of $\Xi$ off nucleons. *Phys. Rev. C*, 74:035205, Sep 2006.

[12] W. Liu and C. M. Ko. Photoproduction of pentaquark cascades from nucleons. *Phys. Rev. C*, 69:045204, Apr 2004.

[13] L. *et al* Guo. Cascade production in the reactions gamma p to K+ K+ (X) and gamma p to K+ K+ pi- (X). *Phys.Rev.*, C76:025208, 2007.

[14] J. Ka Shing Man, Yongseok Oh, and K. Nakayama. Role of high-spin hyperon resonances in the reaction $\gamma p \to K^+K^+\Xi^-$. *Phys. Rev. C*, 83:055201, May 2011.

[15] R.K. Bradford et al. First measurement of beam-recoil observables $C_x$ and $C_z$ in hyperon photoproduction. *Phys.Rev.*, C75:035205, 2007.

[16] R. Schumacher. Polarization of hyperons in elementary photoproduction. In Josef Pochodzalla and Thomas Walcher, editors, *Proceedings of The IX International Conference on Hypernuclear and Strange Particle Physics*, pages 339–344. Springer Berlin Heidelberg, 2007.

[17] A.V. Anisovich, V. Kleber, E. Klempt, V.A. Nikonov, A.V. Sarantsev, and U. Thoma. Baryon resonances and polarization transfer in hyperon photoproduction. *The European Physical Journal A*, 34(3):243–254, 2007.

[18] M.E. McCracken et al. Differential cross section and recoil polarization measurements for the $\gamma p \to K^+\Lambda$ reaction using CLAS at Jefferson Lab. *Phys.Rev.*, C81:025201, 2010.

[19] D. Flamm and F. Schöberl. *Introduction to the quark model of elementary particles*. Number v. 1 in Introduction to the Quark Model of Elementary Particles. Gordon and Breach, 1982.

[20] Carlos G. Granados and Misak M. Sargsian. Quark structure of the nucleon and angular asymmetry of proton-neutron hard elastic scattering. *Phys. Rev. Lett.*, 103:212001, Nov 2009.

[21] G. Bunce. *Phys. Rev. Lett.*, 36:1113–1116, May 1976.

[22] I.S. Barker, A. Donnachie, and J.K. Storrow. Complete experiments in pseudoscalar photoproduction. *Nuclear Physics B*, 95(2):347 – 356, 1975.

[23] G. Knochlein, D. Drechsel, and L. Tiator. Photo- and electroproduction of eta mesons. *Zeitschrift fur Physik A Hadrons and Nuclei*, 352(3):327–343, 1995.

[24] Wen-Tai Chiang and Frank Tabakin. Completeness rules for spin observables in pseudoscalar meson photoproduction. *Phys. Rev. C*, 55:2054–2066, Apr 1997.

[25] H. Arenhoevel and A. Fix. Complete set of observables for photoproduction of two pseudoscalars on a nucleon. 2014.

[26] J. Ashman *et al.* A measurement of the spin asymmetry and determination of the structure function $g_1$ in deep inelastic muon-proton scattering. *Physics Letters B*, 206:364–370, May 1988.

[27] Aidala *et al.* The spin structure of the nucleon. *Rev. Mod. Phys.*, 85:655–691, Apr 2013.

[28] Jefferson lab picture exchange. http://www.jlab.org.

[29] B. Mecking *et al.* The CEBAF large acceptance spectrometer (CLAS). *Nucl. Instrum. Methods A 503, 513*, 2003.

[30] J. T. Goetz. *Ξ Hyperon Photoproduction from Threshold to 5.4 GeV with the CEBAF Large Acceptance Spectrometer*. PhD thesis, University of California Los Angeles, 2010.

[31] C. Bookwalter. *A Search for Exotic Mesons in $\gamma p \to \pi^+\pi^+\pi^- n$ with CLAS at Jefferson Lab*. PhD thesis, Florida State University, 2012.

[32] J. Li. The new tagger calibration program. *CLAS*, 2003.

[33] g12 Colaboration. g12 analysis procedures, statistics and systematics. *CLAS Note*, 2013.

[34] M.D Mestayer *et al.* The clas drift chamber system. *Nuclear Instruments and Methods in Physics Research Section A: Accelerators, Spectrometers, Detectors and Associated Equipment*, 449(1,2):81–111, 2000.

[35] D. S. Carman. 2002-018 (unpublished). *CLAS Note*, 2002.

[36] D. Schott. *A Search for an Exotic Meson in $\gamma p \to \Delta^{++}\pi^-\eta$ Reaction*. PhD thesis, Florida International University, 2012.

[37] E.S. Smith *et al.* The time-of-flight system for {CLAS}. *Nuclear Instruments and Methods in Physics Research Section A: Accelerators, Spectrometers, Detectors and Associated Equipment*, 432:265 – 298, 1999.

[38] G. Adams *et al.* The CLAS Cherenkov detector. *Nuclear Instruments and Methods in Physics Research Section A-accelerators Spectrometers Detectors and Associated Equipment*, 465:414–427, 2001.

[39] M. Amarian *et al.* The clas forward electromagnetic calorimeter. *CLAS*.

[40] K. Nakayama. Observables in two spineless-meson photoproduction. *Unpublished*.

[41] David R. Giebink. Relativity and spin in one-, two-, and three-body systems. *Phys. Rev. C*, 32:502–515, Aug 1985.

[42] K. *et al* Wijesooriya. Polarization measurements in neutral pion photoproduction. *Phys. Rev. C*, 66:034614, Sep 2002.

[43] B. Reihl, M. Erbudak, and D. M. Campbell. Production of spin-polarized electrons by photoemission from gaas(110). *Phys. Rev. B*, 19:6358–6366, Jun 1979.

[44] Haakon Olsen and L. C. Maximon. Photon and electron polarization in high-energy bremsstrahlung and pair production with screening. *Phys. Rev.*, 114:887–904, May 1959.

[45] Strauch and Berman *et al.* Beam-helicity asymmetries in double-charged-pion photoproduction on the proton. *Phys. Rev. Lett.*, 95:162003, Oct 2005.

[46] E. Pasyuk. Energy loss corrections for charged particles in clas. *CLAS-Note*, 2007.

[47] M. Holtrop. Gsim: Clas geant simulation.

[48] J.W.C. McNabb et al. Hyperon photoproduction in the nucleon resonance region. *Phys.Rev.*, C69:042201, 2004.

# VITA

## JASON STEPHAN WILLIAM BONO

| | |
|---|---|
| 2005-2006 | B.Sc., Mathematical Physics<br>Macquarie University<br>Sydney, Australia |
| 2007-2009 | M.S., Physics<br>University of Miami<br>Miami, Florida |
| 2009-2014 | Ph.D., Physics<br>Florida International University<br>Miami, Florida |

## SELECTED PUBLICATIONS AND PRESENTATIONS

1. Jason Bono, *Newport News, Virgina* (2014). First Time Measurements of Polarization Observables for the Charged Cascade in Photoproduction.

2. Jason Bono, *Newport News, Virgina* (2013). Spin Observables for the $\Xi^-$ in Photoproduction, *Fall Meeting of the American Physical Society, Division of Nuclear Physics.*

3. Jason Bono (2014). Polarization of the Cascade Hyperon in Photoproduction, *Proceedings of Science.*

4. Jason Bono, *Montevideo, Uruguay* (2013). Polarization of the Cascade Hyperon in Photoproduction, *10th Annual Latin American Symposium on Nuclear Physics and Applications.*

5. Jason Bono, *Plymouth, New Hampshire* (2012). A First Time Polarization Measurement of the $\Xi$ Baryon in Photoproduction, *Gordon Research Conference on Photonuclear Reactions.*

6. Jason Bono, *St. Petersburg, Florida* (2012). Search for a New $\Xi$ Resonance, *Conference on Intersections of Particle and Nuclear Physics.*